

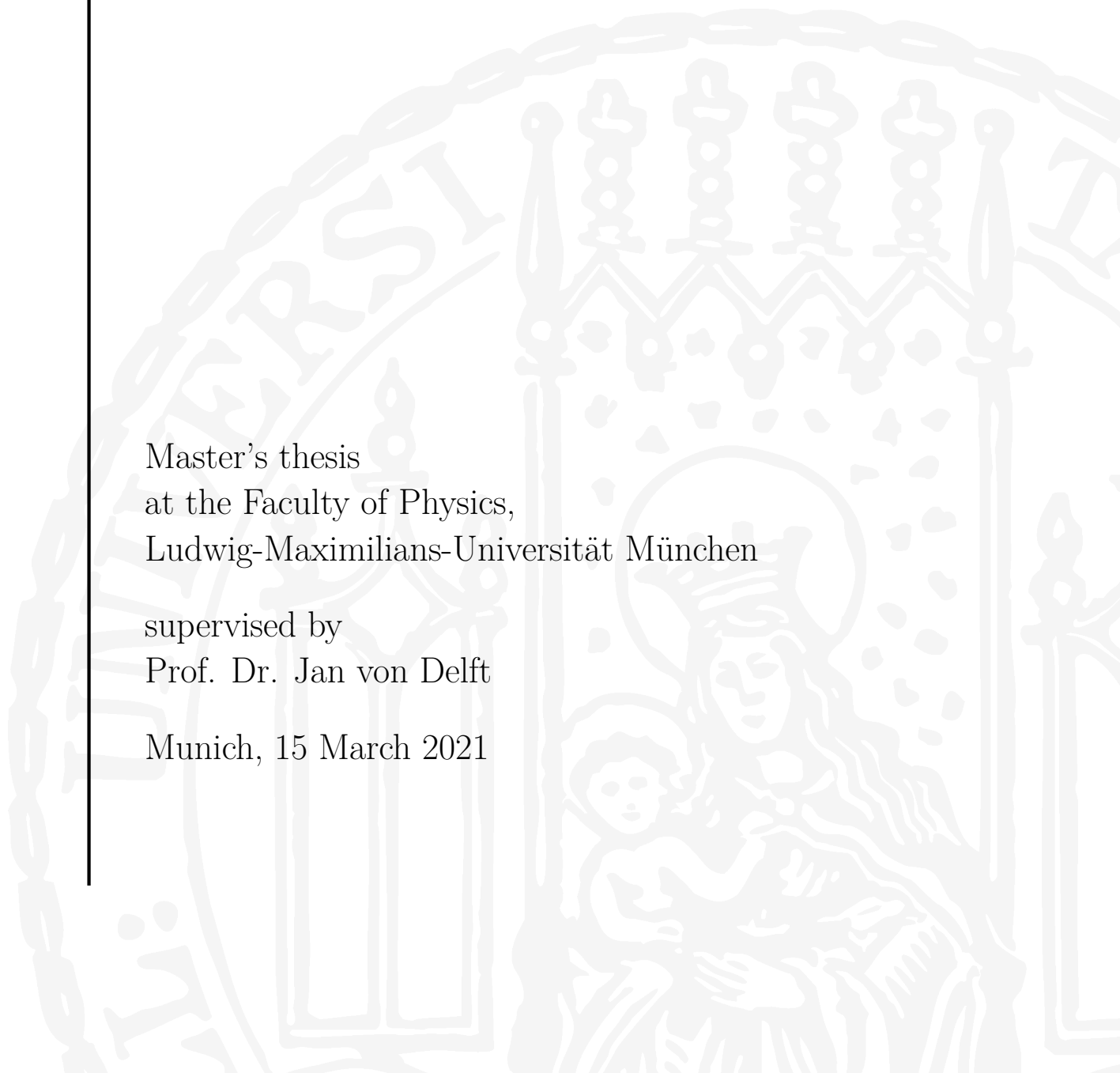
Multiloop Pseudofermion Functional Renormalization Group Study of the Pyrochlore XXZ Model

Marc K. Ritter

Master's thesis
at the Faculty of Physics,
Ludwig-Maximilians-Universität München

supervised by
Prof. Dr. Jan von Delft

Munich, 15 March 2021



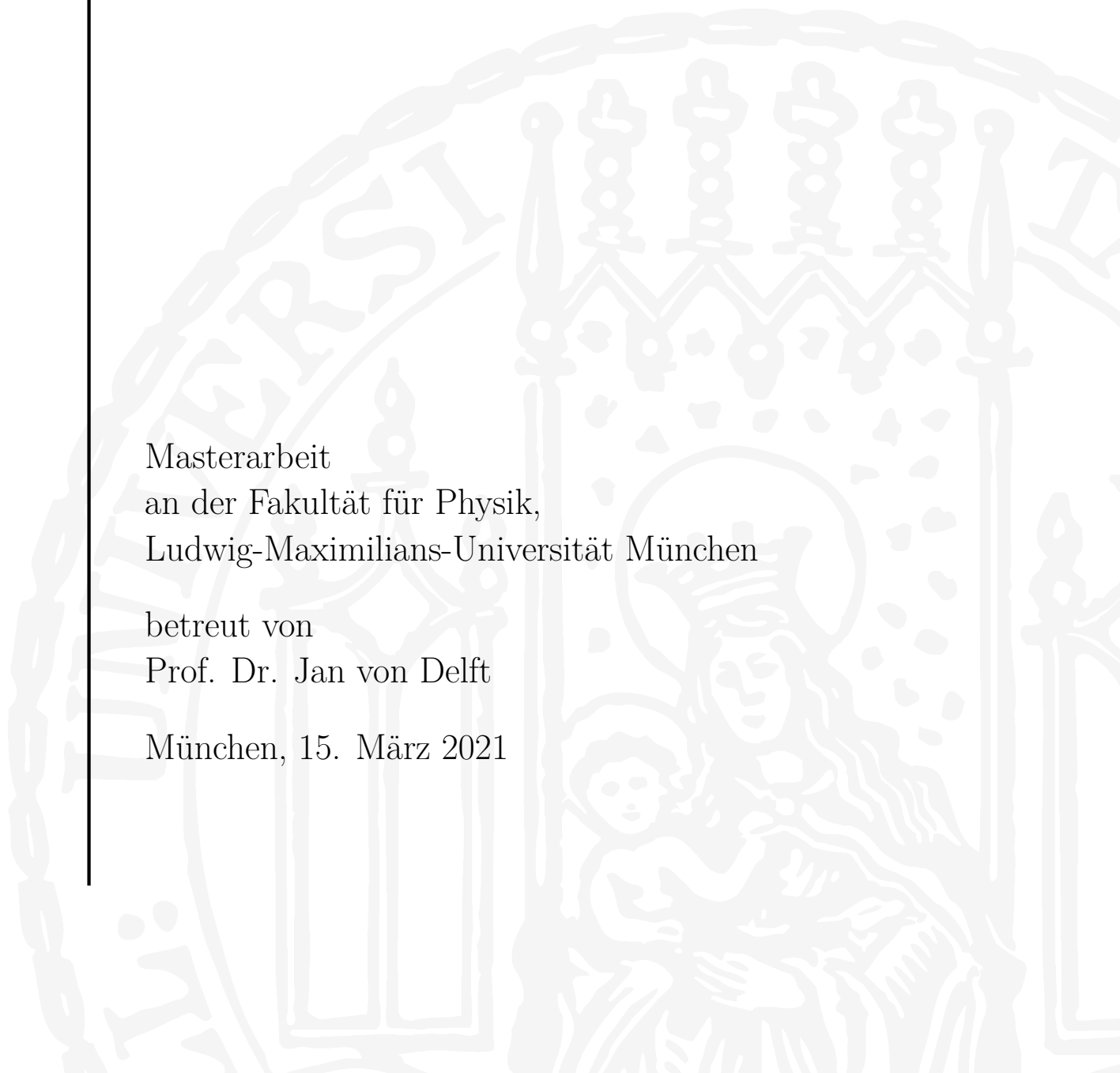
Untersuchung des
Pyrochlor-XXZ-Modells mittels
Mehrschleifen-FRG für
Pseudofermionen

Marc K. Ritter

Masterarbeit
an der Fakultät für Physik,
Ludwig-Maximilians-Universität München

betreut von
Prof. Dr. Jan von Delft

München, 15. März 2021



Abstract

Rare-earth pyrochlore oxides are considered prime candidates for quantum spin liquid behavior due to their geometrically frustrated magnetism. Though a rich variety of possible ground states of the effective spin-1/2 model for pyrochlores has been proposed, the combination of a three-dimensional lattice and frustrated interactions poses great difficulty for methods beyond mean-field theory. We use the recently developed multiloop pseudofermion fRG approach to quantum spin systems to compute ground states in all parts of the phase diagram of this model. This thesis presents the approach in detail, including information about solutions to practical challenges that arise during implementation. We derive explicit expressions for multiloop pseudofermion fRG flow equations for the XXZ model and some observables of interest, most importantly the spin-spin correlator. We show results of the application of this approach to the pyrochlore XXZ model and discuss its reliability. Comparing physical results such as spin susceptibilities and neutron scattering cross sections obtained from our implementation to prior theoretical work and experimental results, we find excellent correspondence in spite of some technical problems.

Acknowledgments

I would like to express my deepest gratitude to Jan von Delft, whose guidance and support as my supervisor throughout the thesis project was truly invaluable. I particularly appreciate the great amount of effort and time he put into helping me whenever I needed it, while trusting me to work independently when I was making progress. Always offering level-headed and reliable advice, his supervision kept me from losing the big picture in excessive detail. I learned a lot from him, not only about physics, but also about the practical aspects of scientific work and communication.

This project would not have been possible without the contributions of each member of the multiloop pffRG project. I am extremely grateful to Julian Thönni, who originally started the implementation of multiloop pffRG used here and whose continuous and tireless work on improvements was admirable. I am indebted to Fabian Kugler, who frequently offered inspired ideas and figured out how to proceed when we were stuck. Matthias Punk guided our investigations with his extensive knowledge about the physics of quantum many-body systems and spin liquids, and I would also like to extend my sincere thanks to him. He is the person who most inspired me to enter the field of condensed matter physics through his excellent lectures, which sparked a lasting fascination for quantum many-body phenomena in me. It is a pleasure to work with Jan, Julian, Fabian and Matthias, and I am very glad to be part of this project.

Jan, Fabian and Julian also offered helpful comments on an earlier version of this thesis, as did Benedikt Schneider. I am also grateful to Benedikt for helping me gain insight into the physics of rare-earth pyrochlores. I very much appreciate the helpful exchange of ideas with Dominik Kiese and Tobias Mller during our discussions about all aspects related to implementing multiloop pffRG.

I would like to acknowledge helpful discussions with Elias Walter, Santiago Aguirre, Anxiang Ge, Nepomuk Ritz and Marcel Gievers about fRG and other topics. I would also like to thank all members of the chair for creating a pleasant and comfortable environment to work in.

Special thanks to Owen Benton, who kindly gave permission to reproduce some of his figures in this thesis.

Contents

Contents	v
1 Introduction	1
2 Models of frustrated quantum magnetism in pyrochlores	5
2.1 Effective spin- $1/2$ model for pyrochlores	5
2.2 Lattice symmetries and the local spin basis	7
2.3 Zero-temperature phases of the pyrochlore XXZ model	8
2.4 Observables	11
2.4.1 Spin-spin correlations	11
2.4.2 Neutron-scattering experiments	12
3 Method	15
3.1 Abrikosov’s pseudofermion representation	15
3.2 Parquet Formalism	18
3.2.1 Definition of the correlators	18
3.2.2 Self-energy and four-point vertex	18
3.2.3 Bethe–Salpeter and Schwinger–Dyson equation	20
3.2.4 The parquet approximation	20
3.3 Multiloop functional renormalization group	21
3.3.1 Energy cutoff	22
3.3.2 Vertex flow	24
3.3.3 Self-energy flow	25
3.3.4 Integrating the renormalization group flow	28
3.3.5 Parquet solutions at finite Λ	30
4 Implementation	31
4.1 Parametrization of vertices and propagators	31
4.1.1 SU(2) gauge redundancy of the parton construction	32
4.1.2 Physical symmetries	33

4.1.3	Parametrized form of the propagator and self-energy . . .	34
4.1.4	Parametrization of spin and site dependence of the vertex	35
4.1.5	Lattice symmetries	36
4.1.6	Asymptotic structure and natural frequency parametrization of the vertex	38
4.2	Parametrized building blocks for the XXZ model	41
4.2.1	Self-energy loop	42
4.2.2	a -bubble	43
4.2.3	t -bubble	45
4.2.4	p -bubble	46
4.2.5	Symmetries preserved by the flow	48
4.3	Spin susceptibility	49
4.3.1	Evaluation of the spin susceptibility in pffRG	49
4.3.2	Efficient evaluation of the zero-time susceptibility	51
5	Results	55
5.1	Loop convergence	56
5.2	Pseudofermion constraint	61
5.3	Physical observables	62
5.4	Ordered phases	62
5.5	Quantum spin ice	67
5.6	Easy-plane quantum spin liquid	73
6	Summary and outlook	77
A	The pyrochlore lattice	79
A.1	Definition	79
A.2	Symmetries of vertices on a pyrochlore lattice	79
A.3	Symmetry reduction of the effective displacement	81
B	Frequency meshes for pffRG	83
B.1	Structure of the frequency meshes	83
B.2	Dynamic adjustment algorithm	84
B.3	Criteria for the adjustment heuristic	85
C	Fast convolution for RPA-type diagrams	87
C.1	Convolution structure of the RPA bubble	88
C.2	Circular convolution theorem	89
C.3	Discrete Fourier transform of vertices	91
C.4	Symmetries of the Fourier-transformed vertex	92
C.5	Complexity of the fast convolution	93
	Bibliography	97
	Selbständigkeitserklärung	107

Introduction

The effect of microscopic geometry and quantum behavior on macroscopic properties of matter is perhaps most direct in quantum spin liquids. Quantum spin liquids are unusual states of magnetic systems characterized by absence of long-range order and an extreme degree of entanglement, which have no classical analogue [1]. In fact, it is precisely the strength of the quantum fluctuations in the system that prevents order, and thus the macroscopic behavior is influenced in a very direct way by the quantum nature of the microscopic constituents.

There is a variety of models that have stable quantum spin liquid phases, such as a quantum dimer model on a triangular lattice [2] as well as Kitaev's toric code [3] and honeycomb [4] models. Another class of models that may show spin liquid behavior and are arguably closer to real materials are anti-ferromagnetic Ising, Heisenberg and XYZ models on lattices with geometric frustration. These models may also be used to describe some materials with suspected spin-liquid behavior such as herbertsmithite ($\text{ZnCu}_3(\text{OH})_6\text{Cl}_2$), a mineral with kagome lattice structure and antiferromagnetic coupling between nearest neighbors [1, 5–7]. Thus, both the validity of the models as well as the methods used to solve them can be tested [1].

Experimentally, signatures of spin liquid behavior have been observed for many rare-earth pyrochlore oxides [8–25]. This class of materials is also very well-suited for the theoretical study of spin liquid phases for several reasons:

- The magnetic moments are effectively spin- $1/2$ and strongly localized. Therefore, such systems should be well described by a spin- $1/2$ nearest-neighbor model [1].
- The exchange coupling constants can be obtained from experimental observations of excitation spectra [20].
- The lattice structure consists of corner-sharing tetrahedra which induces a high degree of geometric frustration [12, 26].

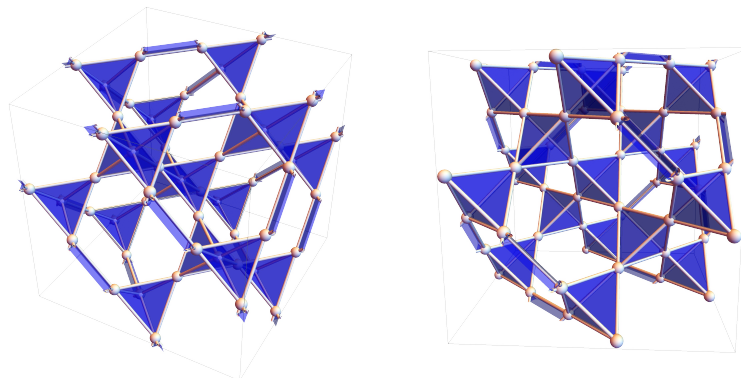


Figure 1.1: The pyrochlore lattice from two different points of view. Nearest-neighbor bonds connect atoms along the edges of the tetrahedra.

These pyrochlore materials are modeled using Ising and XXZ models¹ on the pyrochlore lattice (see Fig. 1.1). A variety of phases have been postulated for these models, most famously quantum spin ice, a gapless U(1) quantum spin liquid [13, 18, 20, 26–46].

However, all theoretical approaches applied to the pyrochlore XXZ model in prior work have important limitations. Analytic results based on mean-field theory are only reliable in limited parts of the phase diagram [1, 13, 38, 44]. Most numerical methods are either biased (such as mean-field approaches), not applicable to the frustrated part of the phase diagram (such as some quantum Monte Carlo approaches) or exceedingly expensive due to the three-dimensional nature of the pyrochlore lattice (such as the density-matrix renormalization group) [43, 47]. One method that does not suffer from these limitations is the pseudofermion functional renormalization group (pffRG) [48, 49]. It is able to treat frustrated spin systems on sufficiently large three-dimensional lattices, treating ordered and disordered states on equal footing without inherent bias [50]. However, there are some unsolved questions concerning this approach. On one hand, its internal consistency has been questioned. The functional renormalization group is only known to be valid in low to intermediate coupling regimes, and a pseudofermion system is inherently in the strong-coupling limit due to lack of a quadratic term in the Hamiltonian. On the other hand, the reliability of physical statements generated with this method has been doubted as well, since the operator constraint of the pseudofermion representation is violated. Both points are discussed in the first sections of chapter 5, and more detail can be found in a preprint that is partially based on work done for this thesis [51].

¹In our model, the coupling of the x - and y -components is equal. Thus, the XYZ model becomes an XXZ model [20].

Recently, the traditional functional renormalization group (fRG) has been expanded to the so-called multiloop functional renormalization group (mfRG) [52–55] which fully incorporates inter-channel feedback and corrects many shortcomings of the original method. It has proven to be accurate to a quantitative level for the two-dimensional Hubbard model for weak to intermediate interaction strength [56]. Combining the multiloop and pseudofermion functional renormalization group, we implemented the multiloop functional renormalization group for the pseudofermion representation of a spin system. We have applied this implementation to the kagome Heisenberg model, and results are presented elsewhere [51]. In parallel and in close cooperation with us, a collaboration in Cologne, Würzburg and Madras applied the same approach to Heisenberg models on various three-dimensional lattices [57]. This thesis is focused on the implementation of this method for the nearest-neighbor XXZ model on the pyrochlore lattice.

In the next chapter, we start by discussing properties of pyrochlores which are known from prior work and by deriving the effective pseudo-spin- $1/2$ XXZ model which is the main topic of this thesis. The multiloop pffRG approach used to study this model is presented in chapter 3. As this method is not straightforward to implement, we give a detailed description of an efficient parametrization for the building blocks of pseudofermion fRG in chapter 4, where we also discuss some numerical problems and solutions for the same. In chapter 5, we present results for the physical behavior of the system as well as some statements concerning the reliability of the method. In the final chapter 6, we summarize the results and relate them to prior work. We also give an outlook on interesting directions future work might take.

Models of frustrated quantum magnetism in pyrochlores

Rare-earth pyrochlores are materials of the type $A_2B_2O_7$, where A is generally a trivalent rare earth ion and B is a tetravalent transition metal ion [12]. The cations of each type form a lattice of corner-sharing tetrahedra (see Fig. 2.1), and these two lattices interpenetrate such that the tetrahedra of one lattice sit in voids of the other lattice. This structure of many triangles introduces an extreme degree of geometric frustration. Combined with the effects of highly anisotropic magnetic interactions, this causes many forms of exotic behavior. Phenomena observed in experiments include, among others, spin ice, quantum spin liquids, superconductivity and unconventional forms of the Hall effect [12, 13, 18, 46]. In this chapter, we will briefly summarize the derivation of the pseudo-spin- $1/2$ Hamiltonian that models the magnetic behavior of rare-earth pyrochlores and give an overview of the known features of the zero-temperature phase diagram.

2.1 Effective spin- $1/2$ model for pyrochlores

The magnetic behavior of these pyrochlores can be described using an effective model of the low-energy behavior. This model is constructed as follows: As the B ions are non-magnetic, only the lattice of A ions is of interest¹. The low-energy manifold of the A ion is constrained by Coulomb and spin-orbit interaction to a single total angular momentum value [18, 58]. Within this manifold, the degeneracy of states is lifted through electric interactions with the surrounding crystal ions², i.e. the ‘crystal field’ [18, 58]. The remaining low-energy states are a doublet, where the degeneracy of the two states is enforced

¹In some materials, the B ions indirectly influence the A ions either through hybridization or lattice distortions. This type of behavior is outside the scope of this thesis.

²There are further interactions contributing to this splitting, though the crystal field is the most important contribution [18].

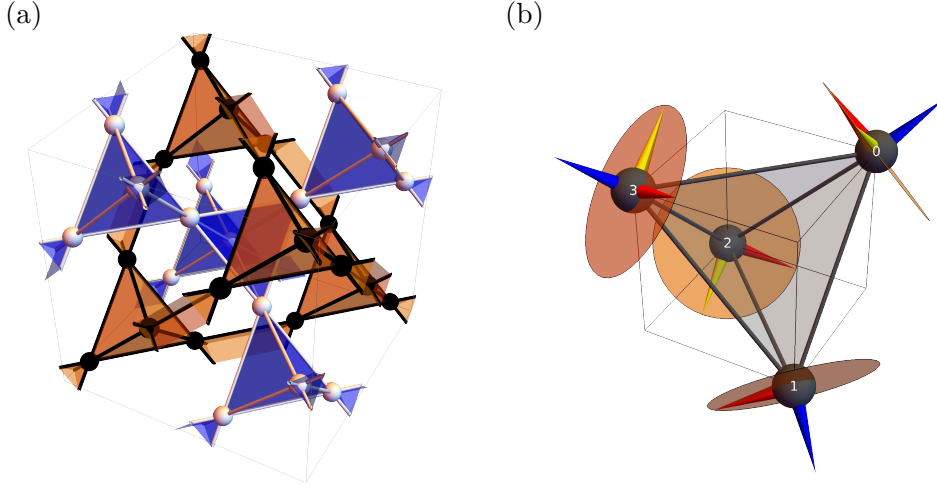


Figure 2.1: (a) Crystal structure of the cations in a pyrochlore material. The A and B ions form one pyrochlore lattice each, and the two pyrochlore lattices are displaced with respect to each other such that the tetrahedra of one lattice sit in voids of the other. For clarity, the oxygen ions are not shown. (b) Local spin basis vectors on the pyrochlore lattice, where the blue vectors point in local z -direction and the discs represent the local xy -plane. The cube is centered on the origin, aligned to the real-space coordinate axes and atom 0 is at position $\frac{a}{2\sqrt{2}}(1, 1, 1)^T$ where a is the distance between nearest neighbors.

either by Kramers' theorem (in case the ion has an odd number of electrons), or by crystal symmetries (in case of an even number of electrons) [13, 18]. We restrict our model to those Kramers doublets that transform as a spin-1/2, though the same effective Hamiltonian can be derived for dipolar-octupolar Kramers doublets as well as non-Kramers doublets [58].

This doublet, which we denote by $|+\rangle$ and $|-\rangle$, can be described by an effective spin-1/2 through

$$\tilde{S}^z \equiv \frac{1}{2}(|+\rangle\langle+| - |-\rangle\langle-|), \quad \tilde{S}^+ \equiv |+\rangle\langle-|, \quad \tilde{S}^- \equiv |-\rangle\langle+|. \quad (2.1)$$

Placing one effective spin on each site of the A lattice, the system is described by the effective Hamiltonian [58, 59]

$$H = \frac{1}{2} \sum_{ij} \sum_{\mu\lambda} J_{ij}^{\mu\lambda} \tilde{S}_i^\mu \tilde{S}_j^\lambda \quad (2.2)$$

where i, j are site indices, and μ, λ enumerate spin directions [59]. The interaction is symmetric $J_{ij}^{\mu\lambda} = J_{ji}^{\lambda\mu}$ and we limit the interaction to nearest neighbors. The relation between \tilde{S}^\pm and \tilde{S}^x, \tilde{S}^y is given by

$$\tilde{S}_i^\pm = \tilde{S}_i^x \pm i\tilde{S}_i^y. \quad (2.3)$$

2.2 Lattice symmetries and the local spin basis

We construct the lattice following the convention set by Ross et. al [20], which has commonly been used in prior work [43, 46]. The unit cell is a tetrahedron centered on the origin with sites at its corners

$$\begin{aligned} \mathbf{r}_0 &= \frac{a}{2\sqrt{2}} (+1, +1, +1)^T, & \mathbf{r}_1 &= \frac{a}{2\sqrt{2}} (+1, -1, -1)^T, \\ \mathbf{r}_2 &= \frac{a}{2\sqrt{2}} (-1, +1, -1)^T, & \mathbf{r}_3 &= \frac{a}{2\sqrt{2}} (-1, -1, +1)^T, \end{aligned} \quad (2.4)$$

where a is the distance between nearest neighbors³. This unit cell is then repeated using the face-centered cubic pattern where the cubes have side length $a_{\text{fcc}} = \frac{4a}{\sqrt{2}}$, and each cube contains 16 sites.

Lattice symmetries constrain the interaction to 4 independent components [20, 46]. For instance, interactions on the bond between \mathbf{r}_0 and \mathbf{r}_1 are given by

$$J_{01} = \begin{pmatrix} J_2 & J_4 & J_4 \\ -J_4 & J_1 & J_3 \\ -J_4 & J_3 & J_1 \end{pmatrix}, \quad (2.5)$$

where the 4 independent components correspond approximately to [46]

- J_1 : ‘XY’ interaction with respect to the local bond,
- J_2 : ‘Ising’ interaction with respect to the local bond⁴,
- J_3 : symmetric off-diagonal interaction and
- J_4 : Dzyaloshinskii-Moriya interaction.

The interaction matrices for other bonds within the same unit cell are related to J_{01} by symmetry transforms Q^c of the lattice (see Appendix A). It is therefore more convenient to express the Hamiltonian in a local basis which encodes these symmetries such that the environment at each site is the same within the local basis. This can be accomplished by choosing the spin basis vectors as shown in Fig. 2.1. We label spin operators in the local basis at each site i by S_i ; the global spin operators are labeled \tilde{S}_i . The transformation can be expressed using site-dependent rotation matrices R_i such that

$$\tilde{\mathbf{S}}_i = R_i \mathbf{S}_i \quad \Leftrightarrow \quad \mathbf{S}_i = R_i^T \tilde{\mathbf{S}}_i \quad (2.6)$$

³In prior work, the ‘lattice constant’ a has been defined in different ways by different authors. It may be defined as

- The distance between nearest neighbors, i.e. between two atoms in the same tetrahedron. This is the definition for a used in this thesis.
- The side length of the cube that contains one tetrahedron (see Fig. 2.1). In our convention, this is $a/\sqrt{2}$.
- The side length of the cubic unit cell of the face-centered cubic lattice that is the Bravais lattice of a pyrochlore crystal. We refer to this length as $a_{\text{fcc}} = 4a/\sqrt{2}$.

⁴The way in which spin components are coupled by these interactions may be unexpected. For example, the ‘Ising’ interaction J_2 , which is usually defined as an interaction between \tilde{S}_i^z spin components, couples \tilde{S}_i^x components in J_{01} instead. The reason for this is that the matrix is rotated in different directions on each bond; in J_{03} and J_{12} , the ‘Ising’ interaction J_2 does couple \tilde{S}_i^z components.

2. Models of frustrated quantum magnetism in pyrochlores

at each site i within the unit cell, and all sites that are related to that site by fcc translation vectors. The matrices R_i are [43, 46]

$$\begin{aligned} R_0 &= \frac{1}{\sqrt{6}} \begin{pmatrix} -2 & 0 & \sqrt{2} \\ 1 & -\sqrt{3} & \sqrt{2} \\ 1 & \sqrt{3} & \sqrt{2} \end{pmatrix}, & R_1 &= \frac{1}{\sqrt{6}} \begin{pmatrix} -2 & 0 & \sqrt{2} \\ -1 & -\sqrt{3} & -\sqrt{2} \\ -1 & \sqrt{3} & -\sqrt{2} \end{pmatrix}, \\ R_2 &= \frac{1}{\sqrt{6}} \begin{pmatrix} 2 & 0 & -\sqrt{2} \\ 1 & -\sqrt{3} & \sqrt{2} \\ -1 & -\sqrt{3} & -\sqrt{2} \end{pmatrix}, & R_3 &= \frac{1}{\sqrt{6}} \begin{pmatrix} 2 & 0 & -\sqrt{2} \\ -1 & \sqrt{3} & -\sqrt{2} \\ 1 & \sqrt{3} & \sqrt{2} \end{pmatrix}. \end{aligned} \quad (2.7)$$

At each site, the S_i^z component points to the center of one of the neighboring tetrahedra (see Fig. 2.1) [46]. In the local basis, the Hamiltonian can now be expressed as

$$\begin{aligned} H = \sum_{\langle i,j \rangle} \left\{ J^z S_i^z S_j^z - J^\pm [S_i^+ S_j^- + S_i^- S_j^+] - J^{\pm\pm} [\zeta_{ij}^* S_i^+ S_j^+ + \zeta_{ij} S_i^- S_j^-] \right. \\ \left. + J^{z\pm} [S_i^z (\zeta_{ij} S_j^+ + \zeta_{ij}^* S_j^-) + S_j^z (\zeta_{ji} S_i^+ + \zeta_{ji}^* S_i^-)] \right\}, \end{aligned} \quad (2.8)$$

where the matrix ζ_{ij} performs rotations between local coordinate frames on different sites within the unit cell [20, 46].

2.3 Zero-temperature phases of the pyrochlore XXZ model

This thesis will focus on the XXZ model, which corresponds to the limit $J^{\pm\pm} = J^{z\pm} = 0$. From prior theoretical studies, such as Refs. [27, 28, 38, 43, 60], the model is known to host a U(1) quantum spin liquid for antiferromagnetic Ising interaction $J^z > 0$ and small transverse interaction $J^\pm \ll J^z$. This case can therefore be considered the simplest model for quantum spin ice [28, 43].

For our method, it is more convenient to express the Hamiltonian in terms of S^x and S^y instead of S^+ and S^- . The XXZ Hamiltonian is

$$\begin{aligned} H &= \sum_{\langle i,j \rangle} \left\{ J^z S_i^z S_j^z - J^\pm [S_i^+ S_j^- + S_i^- S_j^+] \right\} = \\ &= \sum_{\langle i,j \rangle} \left\{ J^z S_i^z S_j^z + J^x [S_i^x S_j^x + S_i^y S_j^y] \right\}, \end{aligned} \quad (2.9)$$

which implies $J^x = J^y = -2J^\pm$. The overall energy scale of the model is arbitrary and has no effect on its behavior. Therefore, we define an energy unit

$$J \equiv \sqrt{(J^x)^2 + (J^z)^2} \quad (2.10)$$

and parametrize the phase diagram using an angle θ , where

$$J^z = J \cos \theta \quad \text{and} \quad J^x = J^y = J \sin \theta. \quad (2.11)$$

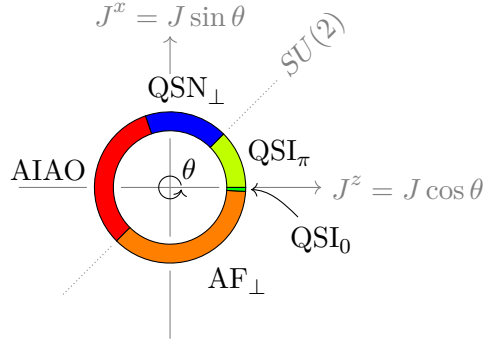


Figure 2.2: Zero-temperature phase diagram of the pyrochlore XXZ model found in cluster-variational calculations. Adapted with permission from Benton et al. [28, Fig. 1(a)].

At $\theta = \frac{\pi}{4}$ and $\frac{3\pi}{4}$, the model becomes a $SU(2)$ -symmetric Heisenberg model.

It is difficult to obtain a complete phase diagram of the XXZ model, simplified as it may seem compared to the variety of possible interactions in a complete description of a pyrochlore. Quantum Monte Carlo methods are only applicable in the sector $\theta \in [-\frac{\pi}{2}, 0]$ due to the sign problem [28]. Exact diagonalisation methods are extremely limited in system size. Thus, theoretical work is forced to rely on inherently approximate methods, such as methods based on mean-field and perturbation theory. These offer some advantages in that their description of quantum states is, compared to heavier numerical methods, more accessible to interpretation in terms of theoretical concepts and analytic methods such as lattice gauge theories. On the other hand, predictions of these methods may be unreliable. When calculating a zero-temperature phase diagram, inaccuracies in the value of the ground-state energy are particularly problematic, as multiple competing states may have very similar energies, particularly in frustrated systems.

Nevertheless, approximate phase diagrams may be obtained by combining and comparing different methods. This approach was pursued by Benton et al. [28] using cluster mean-field theory combined with variational optimization and perturbative expansions, supported by exact diagonalisation, analytic arguments as well as linked-cluster and high-temperature series expansions. A sketch of the phase diagram they obtained is shown in Fig. 2.2. It contains two ordered phases, two quantum spin ice phases and one nematic phase:

All-in-all-out phase (AIAO). A state where all spins are parallel or antiparallel to local S^z -direction. On one half of all tetrahedra in the lattice, all spins at the corners of each tetrahedron point towards the centers of the neighboring tetrahedra, which form the other half of the lattice (see Fig. 2.3(a)) [18].

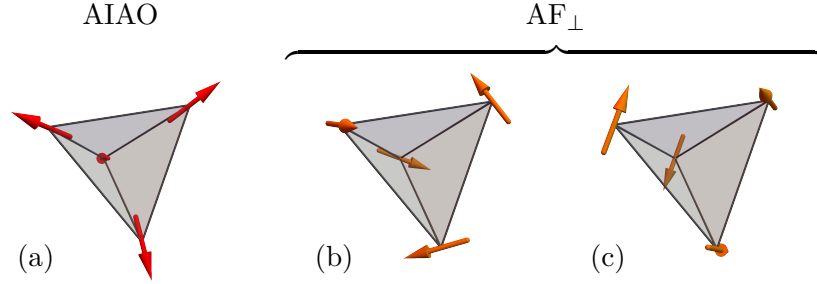


Figure 2.3: States corresponding to ordered phases of the pyrochlore XXZ model. (a) All-in-all-out order, where all spins point parallel (or antiparallel) to local S^z direction. (b, c) Two possible ordered states in the easy-plane antiferromagnetic phase. The rotation symmetry in the easy plane is spontaneously broken in one of the directions inside the local S^x - S^y -plane, and the shown orders are two examples [18].

Easy-plane antiferromagnet (AF_\perp). A state where the spins order *ferromagnetically* inside the local S^x - S^y -plane. In the global basis, this order corresponds to spins aligned in patterns that have antiparallel components between neighboring spins and is therefore labeled an *antiferromagnetic* phase (see Fig. 2.3(b, c)) [18, 43].

Quantum spin ice (QSI). A gapless $U(1)$ spin liquid state. The phase diagram contains two distinct quantum spin ice phases (QSI_0 and QSI_π), which are described by the same effective field theory: a $U(1)$ gauge theory equivalent to a compact version of quantum electrodynamics⁵ [38, 60, 61]. This theory is defined on the so-called dual lattice, which is constructed by replacing each tetrahedron of the pyrochlore lattice by a vertex and each spin by a bond between the two adjacent vertices. The resulting lattice is a diamond lattice [13, 38]. The two quantum spin ice phases differ in the background flux enclosed by the hexagonal plaquettes of this diamond lattice [60]: For $\theta < 0$, this background flux is 0, while for $\theta > 0$, the background flux takes the value π . Following the notation of Benton et al. [28], we label these phases QSI_0 and QSI_π , respectively.

Quantum spin nematic phase (QSN_\perp). A phase which breaks the $U(1)$ spin rotation symmetry in the local S^x - S^y -plane, while preserving translation-symmetry. This order cannot be detected using expectation values of single spin operators. Appropriate order parameters can be constructed as combina-

⁵A detailed derivation can be found in the original work by Hermele et al. [38] and in the review by Gingras and McClarty [13].

tions of spin operators, such as⁶ [62, Eq. (2)]

$$O_{ij}^{\mu\lambda} = \frac{1}{2} (S_i^\mu S_j^\lambda + S_i^\lambda S_j^\mu) - \frac{1}{3} \delta^{\mu\lambda} \langle \mathbf{S}_i \cdot \mathbf{S}_j \rangle. \quad (2.12)$$

2.4 Observables

Given the quantum nature of some of the above phases, it is necessary to find observables that characterize the system's behavior and are suitable for comparison to prior work. Here, we have several related goals in mind: Comparison to prior theoretical work using other methods such as Quantum Monte Carlo, where applicable, enables us to judge the degree of reliability of multiloop pf-FRG. Comparison to analytical results such as mean-field theories allows us to conclude whether the model's behavior can be understood in these analytical terms. Finally, comparison to experiment allows us to understand whether the model itself is a good representation of the physics of frustrated magnetism in pyrochlores and perhaps reveal the microscopic mechanisms at play.

The microscopic behavior of the above states is most easily interpreted using spin-spin correlations $\langle S_i^\mu S_j^\lambda \rangle$. On the other hand, comparison to experiments requires predictions for macroscopic observables. The quantity closest to microscopic spin correlations that has been measured is the neutron scattering pattern for polarized neutrons. Detailed descriptions of both observables will be given in the following sections.

2.4.1 Spin-spin correlations

The spin susceptibility is the primary quantity we use to characterize states obtained by the functional renormalization group flow. It is defined as [48, 66]

$$\chi_{ij}^{\mu\lambda}(\Omega) = \int_0^\beta d\tau e^{i\Omega\tau} \langle \mathcal{T}_\tau S_i^\mu(\tau) S_j^\lambda(0) \rangle, \quad (2.13)$$

where $\mu, \lambda \in \{x, y, z\}$ and τ denotes imaginary time.

The susceptibility can be defined using spin operators in the local or the global spin basis. These quantities have different advantages: The susceptibility in the global basis, which we label $\tilde{\chi}$, can be measured in experiments and describes the reaction of the system to external magnetic perturbations. The susceptibility in the local basis, which we label χ , is more useful to gain insight into the behavior of the spin states themselves, as it inherently respects symmetries of the lattice. For this reason, it also has only 2 independent

⁶Many related definitions of the nematic order parameter, which are equally suitable for our purposes, have been used in prior work [28, 43, 62–65]. Here, we use the convention of Shannon et al. [62, Eq. (2)].

2. Models of frustrated quantum magnetism in pyrochlores

components: $\chi^z \equiv \chi^{zz}$ and $\chi^\perp \equiv \chi^{xx} = \chi^{yy}$, and all off-diagonal components of χ vanish. The two quantities are related by

$$\begin{aligned}\tilde{\chi}_{ij}^{\mu\lambda}(\Omega) &= \int_0^\beta d\tau e^{i\Omega\tau} \langle \mathcal{T}_\tau \tilde{S}_i^\mu(\tau) \tilde{S}_j^\lambda(0) \rangle = \\ &= \int_0^\beta d\tau e^{i\Omega\tau} \sum_{\kappa\eta} (R_i^{-1})^{\mu\kappa} (R_j^{-1})^{\lambda\eta} \langle \mathcal{T}_\tau S_i^\kappa(\tau) S_j^\eta(0) \rangle = \\ &= \sum_{\kappa} R_i^{\kappa\mu} R_j^{\kappa\lambda} \chi_{ij}^{\kappa\kappa}(\Omega),\end{aligned}\quad (2.14)$$

where the matrices R_i are the basis transform matrices defined in Eq. (2.7). Though $\chi^{\mu\lambda}$ is diagonal in (μ, λ) , the basis transform causes $\tilde{\chi}^{\mu\lambda}$ to acquire off-diagonal components.

2.4.2 Neutron-scattering experiments

Neutron-scattering experiments offer a very direct characterization of magnetic states in a material, as the neutron-scattering intensity is closely related to the spin-spin correlations in the global basis given by $\tilde{\chi}$. Such experiments have been performed on many pyrochlore oxide materials⁷, and similarities in this data would provide evidence for realization of a similar state in nature.

The total scattering intensity is proportional to the neutron scattering structure factor [43]

$$\mathcal{S}_{\text{total}}(\mathbf{q}, \Omega) = \sum_{\mu\lambda} \mathcal{S}_{\text{total}}^{\mu\lambda}(\mathbf{q}, \Omega) = \sum_{\mu\lambda} \left(\delta^{\mu\lambda} - \frac{q^\mu q^\lambda}{\|\mathbf{q}\|^2} \right) \tilde{\chi}^{\mu\lambda}(\mathbf{q}, \Omega),\quad (2.15)$$

where $\mu, \lambda \in \{x, y, z\}$, q^μ is the μ -component of \mathbf{q} , and

$$\tilde{\chi}^{\mu\lambda}(\mathbf{q}, \Omega) = \sum_{ij} e^{i\mathbf{q}(\mathbf{r}_j - \mathbf{r}_i)} \int dt e^{i\Omega t} \langle \tilde{S}_i^\mu(t) \tilde{S}_j^\lambda(0) \rangle\quad (2.16)$$

is the Fourier transformed spin-spin correlator. A common choice, pioneered by Fennel et al. [10], is to fix the neutron polarization vector to $\mathbf{P} = (1, -1, 0)^T / \sqrt{2}$ and decompose the signal into a spin-flip channel

$$\mathcal{S}_{\text{SF}}(\mathbf{q}, \Omega) = \sum_{\mu\lambda} \frac{(\mathbf{P} \times \mathbf{q})^\mu (\mathbf{P} \times \mathbf{q})^\lambda}{\|\mathbf{q}\|^2} \tilde{\chi}^{\mu\lambda}(\mathbf{q}, \Omega)\quad (2.17)$$

and non-spin-flip channel

$$\mathcal{S}_{\text{NSF}}(\mathbf{q}, \Omega) = \sum_{\mu\lambda} P^\mu P^\lambda \tilde{\chi}^{\mu\lambda}(\mathbf{q}, \Omega).\quad (2.18)$$

⁷See Refs. [1, 9–11, 13–17, 19–21, 24, 32, 36, 37, 43, 46, 67–70].

These two quantities are usually measured for scattering vectors $\mathbf{q} = (q^1, q^1, q^3)^T$ and integrated over all energies Ω , though some experiments are able to decompose the signal into finite energy intervals.

Signatures of some of the proposed spin liquid states, including the pinch points of spin ice, appear in only one of the two channels [10, 43]. These are difficult to observe in a setup that does not track neutron polarization and measures only the superposition $\mathcal{S}_{\text{total}} = \mathcal{S}_{\text{SF}} + \mathcal{S}_{\text{NSF}}$. In theoretical work, it is therefore equally important to produce separate predictions for each of the two channels. In this thesis, the two structure factors \mathcal{S}_{SF} and \mathcal{S}_{NSF} will be the quantities used to compare predictions to experiment.

Method

To simulate the behavior of quantum spin systems, we will use an approach that combines the pseudofermion functional renormalization group (pffRG) method pioneered by Reuther et al. [48, 49] and the multiloop extension to the functional renormalization group developed by Kugler et al. [53–55]. This approach consists of the following steps:

1. Reformulation of the spin Hamiltonian through Abrikosov’s pseudofermion representation.
2. Introduction of an artificial infrared cutoff Λ to the bare fermion propagator.
3. Self-consistent solution of the Parquet equations at large Λ .
4. Integration of a multiloop fRG flow to small Λ , using the solution obtained in the previous step as initial condition.

In this chapter, the components of our method, namely the pseudofermion representation, the Parquet formalism and the multiloop functional renormalization group will be described in order.

3.1 Abrikosov’s pseudofermion representation

As the fRG methods used in this thesis were designed to investigate fermion rather than spin systems, it is necessary to first transform the spin-1/2 Hamiltonian

$$H = \frac{1}{2} \sum_{ij} \sum_{\mu\nu} J_{ij}^{\mu\nu} S_i^\mu S_j^\nu, \quad (3.1)$$

where i, j enumerate lattice sites and $\mu, \nu \in \{x, y, z\}$ enumerate spin direction, into a Hamiltonian of fermion operators. To this end, we replace

$$S_i^\mu \rightarrow \frac{1}{2} \mathbf{f}_i^\dagger \boldsymbol{\sigma}^\mu \mathbf{f}_i, \quad (3.2)$$

3. Method

where $\mathbf{f}_i = \begin{pmatrix} f_{i\uparrow} \\ f_{i\downarrow} \end{pmatrix}$ and $f_{i\alpha}$ are operators with fermionic anti-commutation relations [71]. The transformed Hamiltonian is

$$\begin{aligned} H &= \frac{1}{2} \sum_{ij} \sum_{\mu\nu} J_{ij}^{\mu\nu} \sum_{\alpha\beta\gamma\delta} \frac{1}{4} \sigma_{\alpha\beta}^\mu \sigma_{\gamma\delta}^\nu f_{i\alpha}^\dagger f_{i\beta} f_{j\gamma}^\dagger f_{j\delta} \\ &= \frac{1}{8} \sum_{ij} \sum_{\mu\nu} J_{ij}^{\mu\nu} \sum_{\alpha\beta\gamma\delta} \sigma_{\alpha\beta}^\mu \sigma_{\gamma\delta}^\nu f_{i\alpha}^\dagger f_{j\gamma}^\dagger f_{j\delta} f_{i\beta} + \frac{1}{8} \sum_i \sum_\mu J_{ii}^{\mu\mu} \sum_\alpha f_{i\alpha}^\dagger f_{i\alpha} \end{aligned} \quad (3.3)$$

in normal-ordered form. The last term $\sim f^\dagger f$ is equivalent to a shift of the chemical potential in the grand canonical ensemble.

On each site, the spin states $|\uparrow\rangle, |\downarrow\rangle$ are represented by fermions $f_\uparrow^\dagger |0\rangle, f_\downarrow^\dagger |0\rangle$ on that site. However, in fermion language, sites can be doubly occupied, $|2\rangle$, or not occupied at all, $|0\rangle$; these states do not correspond to any spin state and are therefore unphysical. To restrict the Hilbert space to physical states, an additional constraint,

$$\sum_\alpha f_{i\alpha}^\dagger f_{i\alpha} = 1 \quad \forall i, \quad (3.4)$$

is necessary [71]. In practice, this constraint is hard to enforce exactly¹ and the weaker constraint

$$\sum_\alpha \langle f_{i\alpha}^\dagger f_{i\alpha} \rangle = 1 \quad (3.5)$$

is used instead. This constraint can be fulfilled by tuning the chemical potential to the particle-hole symmetric value $\mu = 0$ [49]. The fermions f are known as *Abrikosov pseudofermions*, *auxiliary fermions* or *partons* [48, 71, 73].

When using the average constraint, the ground states we obtain might still violate the exact constraint through particle number fluctuations. Therefore, it is necessary to check explicitly whether the constraint is fulfilled. This can be done by calculating the variation in particle number, which should be zero for states fulfilling the exact constraint:

$$\sum_\alpha \langle f_{i\alpha}^\dagger f_{i\alpha} \rangle^2 - \sum_{\alpha\beta} \langle f_{i\alpha}^\dagger f_{i\alpha} f_{i\beta}^\dagger f_{i\beta} \rangle = 0. \quad (3.6)$$

In practice, it is more convenient to use quadratic expectation values of spin operators $\langle S_i^\mu S_i^\mu \rangle$ to test whether the ground state we find is part of the physical sector of the pseudofermion Hilbert space. This test is equivalent to the above Eq. (3.6), since

$$\langle S_i^\mu S_i^\mu \rangle = \frac{1}{4} \left\langle \left(\sigma_{\alpha\beta}^\mu f_{i\alpha}^\dagger f_{i\beta} \right)^2 \right\rangle = \frac{1}{4} \underbrace{\sum_\alpha \langle f_{i\alpha}^\dagger f_{i\alpha} \rangle}_1 - \frac{1}{2} \langle f_{i\uparrow}^\dagger f_{i\downarrow}^\dagger f_{i\downarrow} f_{i\uparrow} \rangle, \quad (3.7)$$

¹For systems at finite temperature, this constraint can be enforced using an imaginary chemical potential $\mu = -i\pi/2\beta$ which eliminates unphysical states in the partition function by shifting the Matsubara frequencies [48, 72]. As this thesis is only concerned with zero-temperature behavior, this method is not applicable here.

3.1. Abrikosov's pseudofermion representation

which should be $= \frac{1}{4}$ for physical states and $< \frac{1}{4}$ for unphysical states². This expectation value is particularly convenient for our purposes, since it is identical to the equal-site component of the zero-time spin susceptibility,

$$\chi_{ii}^{\mu\mu}|_{\tau=0} = \langle S_i^\mu(0) S_i^\mu(0) \rangle, \quad (3.8)$$

which is one of the primary observables used to characterize the results of pffRG simulations (see Sec. 4.3) [51].

An alternative test for the pseudofermion constraint was proposed in prior work [74]. This test consists of adding an on-site interaction term

$$H_{\mathbf{S}^2} = -J_0 \sum_i \mathbf{S}_i^2 \quad (3.9)$$

to the Hamiltonian. In terms of pseudofermion operators, it is equal to

$$\begin{aligned} H_{\mathbf{S}^2} &= -J_0 \sum_i \sum_\mu \sum_{\alpha\beta\gamma\delta} \frac{1}{4} \sigma_{\alpha\beta}^\mu \sigma_{\gamma\delta}^\mu f_{i\alpha}^\dagger f_{i\beta} f_{i\gamma}^\dagger f_{i\delta} \\ &= -J_0 \sum_i \left(\frac{3}{2} \sum_\alpha f_{i\alpha}^\dagger f_{i\alpha} - \frac{3}{4} \left[\sum_\alpha f_{i\alpha}^\dagger f_{i\alpha} \right]^2 \right), \end{aligned} \quad (3.10)$$

which is 0 for the unphysical states $|0\rangle$ (zero occupation) and $|2\rangle$ (double occupation). In a state that fulfills the exact pseudofermion constraint, this term is effectively a constant shift of $-\frac{3}{4}J_0$ per site. Therefore, any variation in $J_0 \geq 0$ should lead to no change in any observable except for a rescaling of effective energy scales [74]. A value of $J_0 < 0$ would lead to a bias in favor of unphysical states and should therefore be avoided. On the other hand, large values of $J_0 > 0$ introduce a bias towards physical states, and in principle $J_0 \rightarrow \infty$ should eliminate the unphysical states.

We tested this approach in practice for the kagome Heisenberg model (see Ref. [51]). There, we found through explicit evaluation of Eq. (3.7) that the particle number constraint is not fulfilled exactly (see Ref. [51, Sec. IV.C]). Furthermore, small to moderate values $J_0 \leq J$ did not cause significant changes in any observable despite the presence of particle number fluctuations. Larger values of $J_0 > J$ reduced these fluctuations, though the introduction of a new, large energy scale in the Hamiltonian lead to considerable numerical difficulties. At all values of J_0 where simulations did not become unstable, there was still significant deviation from exact fulfillment of the particle number constraint [51]. Therefore, we do not repeat this analysis for the pyrochlore XXZ model, and only discuss the original Hamiltonian without added $H_{\mathbf{S}^2}$ -term. Explicit tests of the pseudofermion constraint using Eq. (3.7) are shown in Sec. 5.2.

²This correlator is able to indicate violation of the pseudofermion constraint reliably despite the lack of an expectation value detecting the presence of $|0\rangle$, because any state that satisfies $\sum_\alpha \langle f_{i\alpha}^\dagger f_{i\alpha} \rangle = 1$ cannot contain zero occupation components $|0\rangle$ without an ‘equal amount’ of double occupation $|2\rangle$.

3.2 Parquet Formalism

3.2.1 Definition of the correlators

A system of interacting fermions can be described by an action

$$S = \sum_{1'1} \bar{\psi}_{1'} \underbrace{\left[(-i\omega_1 - \mu) \delta_{1'1} + H_0(1'; 1) \right]}_{-(G_0)^{-1}} \psi_1 - \frac{1}{4} \sum_{1'2'12} \Gamma_0(1', 2'; 1, 2) \bar{\psi}_{1'} \bar{\psi}_{2'} \psi_2 \psi_1, \quad (3.11)$$

where the indices $1', 2', 1, 2$ represent all quantum numbers including Matsubara frequency indices, the $\bar{\psi}, \psi$ are Grassmann fields, H^0 is the quadratic part of the Hamiltonian and Γ_0 is the bare interaction vertex, which is proportional to the quartic part of the Hamiltonian. In pseudofermion systems, the Hamiltonian does not contain a quadratic part and the bare propagator is

$$G_0 = \frac{\delta_{1'1}}{i\omega_1}, \quad (3.12)$$

where $\mu = 0$ corresponds to the mean particle number constraint (3.5) for Abrikosov pseudofermions [48, 75].

To understand the behavior of this system, it is necessary to evaluate correlators of the form

$$\langle \psi_1 \dots \psi_n \bar{\psi}_{1'} \dots \bar{\psi}_{n'} \rangle = \frac{1}{Z} \int D[\bar{\psi}, \psi] \psi_1 \dots \bar{\psi}_{n'} e^{-S[\bar{\psi}, \psi]}. \quad (3.13)$$

The most important correlators are the two-point correlator (propagator)

$$G(1', 1) = -\langle \psi_{1'} \bar{\psi}_1 \rangle \quad (3.14)$$

and the four-point correlator

$$G^{(4)}(1', 2'; 1, 2) = \langle \psi_{1'} \psi_2 \bar{\psi}_2 \bar{\psi}_1 \rangle. \quad (3.15)$$

The propagator and four-point correlator are already sufficient to calculate many physical quantities, such as the magnetic susceptibility χ in pseudofermion models. It is, however, not possible to obtain exact expressions in general models. The parquet formalism, which will be presented in the following sections, first decomposes these correlators into various contributions and then neglects some of these contributions which are both very difficult to evaluate and expected to be weaker than other contributions [76].

3.2.2 Self-energy and four-point vertex

The correlators $G, G^{(4)}$ can be decomposed into various parts with useful symmetry properties and relations to one another. The propagator G is connected to the bare propagator G_0 and the self-energy Σ via Dyson's equation [77]

$$G(1', 1) = G_0(1', 1) + \sum_{23} G_0(1', 2) \Sigma(2, 3) G(3, 1), \quad (3.16)$$

which can be expressed in diagrammatic language as

$$\text{---}\leftarrow = \text{---}\leftarrow\text{---} + \text{---}\leftarrow\text{---}\bigcirc\leftarrow, \quad (3.17)$$

where the continuous lines $\text{---}\leftarrow$ represent full propagators, dashed lines $\text{---}\leftarrow\text{---}$ represent bare propagators and the circle \bigcirc represents the self-energy.

The four-point correlator can be expressed as a perturbation series of diagrams. This series contains two disconnected diagrams, and all other diagrams are connected and one-particle irreducible³. In other words, there are no connected diagrams that can be decomposed into two disconnected parts by cutting a single propagator, because to generate such a diagram, a three-point vertex would be necessary, which is not part of the action (3.11). The one-particle irreducible part of $G^{(4)}$ defines the full four-point vertex Γ , which we refer to as ‘the vertex’:

$$\begin{aligned} G^{(4)}(1', 2'; 1, 2) &= G(1', 1) G(2', 2) - G(1', 2) G(2', 1) \\ &+ \sum_{3'4'34} G(1', 3) G(2', 4) \Gamma(3, 4; 3', 4') G(3', 1) G(4', 2) \end{aligned} \quad (3.18)$$

In diagrammatic language, the connectivity becomes more obvious:

$$G^{(4)}(1', 2'; 1, 2) = \begin{array}{c} \text{---}\leftarrow\text{---} \\ \text{---}\leftarrow\text{---} \end{array} - \begin{array}{c} \text{---}\leftarrow\text{---} \\ \text{---}\leftarrow\text{---} \end{array} + \begin{array}{c} \text{---}\leftarrow\text{---} \\ \text{---}\leftarrow\text{---} \end{array} + \begin{array}{c} \text{---}\leftarrow\text{---} \\ \text{---}\leftarrow\text{---} \end{array}, \quad (3.19)$$

where the vertex is represented by a gray rectangle.

The vertex Γ , already being one-particle irreducible, can be further decomposed into two-particle reducible parts γ and a fully two-particle irreducible part R . Two-particle reducible diagrams are composed of two simpler diagrams connected by two propagators. These connecting propagators can be parallel, anti-parallel or transverse to each other. Based on this property, the diagrams are categorized as diagrams reducible in the parallel p , anti-parallel a and transverse t channel, respectively. No diagram is two-particle reducible in more than one channel [54, 76, 78]. Therefore,

$$\Gamma = R + \gamma_a + \gamma_p + \gamma_t, \quad (3.20)$$

and we define the class of diagrams not reducible in channel r as [54]

$$I_r = \Gamma - \gamma_r = R + \sum_{r' \neq r} \gamma_{r'}. \quad (3.21)$$

³Inserting a vertex into an external leg of an irreducible diagram and connecting the two remaining legs of the inserted vertex with a propagator would result in a one-particle reducible diagram, but this contribution is already contained in the self-energy of the external propagator.

3.2.3 Bethe–Salpeter and Schwinger–Dyson equation

The reducible structure of γ_r can be made explicit by expressing γ_r as two parts connected by an r -bubble of propagators. To avoid overcounting ladder-like diagrams, which are reducible in multiple places, we demand that one part must be irreducible in that channel. Furthermore, there are combinatorial factors due to symmetries, which are chosen consistent with Kugler and von Delft [54]. Performing this decomposition separately for each channel, we obtain the so-called *self-consistent Bethe–Salpeter relations* [54, 76, 79]:

(3.22)

The factor $\frac{1}{2}$ in the p -channel compensates overcounting of the diagrams in γ_p , which are symmetric under exchange of their two indistinguishable internal propagators. The minus sign occurs because γ_a and γ_t are related by exchange of two fermion legs (see Eq. (3.45)) [52, 54]. For later convenience, we define the pair propagator, Π_r , as a pair of propagators in channel r including the negative sign in Π_t and the combinatorial factor $\frac{1}{2}$ in Π_p . Understanding all products as matrix products with respect to suitably chosen indices, we can summarize the Bethe–Salpeter equations (3.22) as

$$\gamma_r = I_r \Pi_r \Gamma, \quad r \in \{a, p, t\}. \quad (3.23)$$

These relations form a coupled system of equations: Each γ_r is part of the full vertex Γ and the vertex irreducible in other channels $I_{r' \neq r}$. There are still two unknowns, namely the self-energy Σ of the propagators and the irreducible part R of the vertex. The self-energy is related to the vertex through the *Schwinger–Dyson equation* [54, 77, 80, 81]

(3.24)

where the black dots \bullet represent the bare vertex Γ^0 .

3.2.4 The parquet approximation

Thus, if the irreducible part R of the vertex was known, all reducible parts γ_r as well as the self-energy Σ could in principle be obtained through self-consistent solution of the Bethe–Salpeter equations and the Schwinger–Dyson

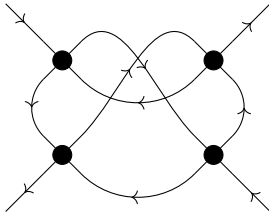


Figure 3.1: The fully two-particle irreducible envelope diagram, which is the lowest-order diagram not included in the parquet approximation.

equation, which are both exact. The simplest approximation for R is to set

$$R = \Gamma^0, \quad (3.25)$$

which is called the first-order solution [76] or parquet approximation [54]. The lowest-order diagram not contained in this approximation is the so-called envelope diagram shown in Fig. 3.1, which is not reducible in any of the three channels.

With this approximation, the system of Bethe–Salpeter equations (3.22) together with the Schwinger–Dyson equation (3.24) is fully specified and can be solved self-consistently. The parquet approximation, though it is the simplest approximation for R , already ensures full consistency on the one- and two-particle level [55, 76]. In a logarithmically divergent perturbation theory, it corresponds to a sum of the leading-order logarithmic contributions, neglecting all higher orders that would make calculations considerably more difficult [54, 71, 76, 78]. This method has been applied to problems such as meson-meson scattering [78], the Kondo effect [71], superconductivity in one dimension [82] and X-ray absorption and emission spectra [76].

In practice, it is not trivial to find a self-consistent solution and for general problems, numerical methods are necessary. While there are, in principle, numerical methods to solve self-consistent equation systems, obtaining a solution in a strongly correlated phase of the system requires considerable numerical effort. This is where the functional renormalization group method (fRG) becomes useful, as it is able to obtain a solution in a difficult (strongly correlated) regime from a solution in an easy (weakly correlated) regime.

3.3 Multiloop functional renormalization group

In condensed matter physics, systems such as the interacting fermions described by the action (3.11) show behavior on different energy scales. Renormalization group methods are based on the idea of treating each energy scale successively. Starting from high energy scales, the low-energy behavior can be approached iteratively, where in each iteration modes at lower energies are

3. Method

introduced and their effect on the behavior of the system is evaluated. Another advantage of these methods is that information about the physical behavior of the system is contained not only in the low-energy solution after the last iteration step, but also in the *renormalization group flow*, i.e. the way the iteration converges to the low-energy fixed points [83, 84]. In the following, we describe the multiloop functional renormalization group (mfRG) method without detailed discussion of conventional fRG methods⁴.

3.3.1 Energy cutoff

To focus on specific energy scales, an infrared energy cutoff⁵ parameter Λ is introduced artificially. The functional renormalization group method replaces the bare propagator G_0 contained in the action (3.11) by a scale-dependent version, which behaves like G_0 at large energies and vanishes for small energies, where the notion of ‘large’ and ‘small’ energy is defined in relation to Λ :

$$G_0^\Lambda(\omega) = \begin{cases} 0, & |\omega| \ll \Lambda \\ G_0(\omega), & |\omega| \gg \Lambda. \end{cases} \quad (3.26)$$

The functional integral expression (3.13) for the correlators then reads

$$\langle \psi_1 \dots \bar{\psi}_{n'} \rangle = \frac{1}{Z} \int \mathcal{D}[\bar{\psi}, \psi] \psi_1 \dots \bar{\psi}_{n'} \exp \left\{ \sum \bar{\psi} (G_0^\Lambda)^{-1} \psi + \dots \right\}. \quad (3.27)$$

The cutoff in G_0^Λ at low energies causes $(G_0^\Lambda)^{-1} \rightarrow -\infty$ and thus suppresses low-energy modes of the Hamiltonian in the functional integral expressions. Thus, the scale dependence of G_0^Λ introduces a scale dependence into the action S^Λ , and this in turn makes all correlators scale-dependent.

This behavior can be implemented in many different ways. We choose to multiply the bare propagator by a regulator function Θ^Λ which contains all Λ -dependence

$$G_0^\Lambda(\omega) = \Theta^\Lambda(\omega) G_0(\omega). \quad (3.28)$$

There is some freedom in choosing a regulator function Θ^Λ , and all choices should lead to identical solutions for $\Lambda \rightarrow 0$, as this choice is not meaningful for the physical system⁶ [54, 55].

⁴Conventional fRG methods are discussed in the review by Metzner et al. [83] and the book by Kopietz et al. [85].

⁵In principle, the flow parameter Λ is not necessarily an energy cutoff. There are fRG methods which use a momentum cutoff instead, and some fRG approaches even use a rescaling of temperatures or interaction strengths as flow parameter [83]. An overview of these approaches can be found in the review by Metzner et al. [83, pp. 309–311].

⁶This condition is fulfilled by multiloop fRG, while conventional fRG fails to give the same solution independent of regulator choice [55].

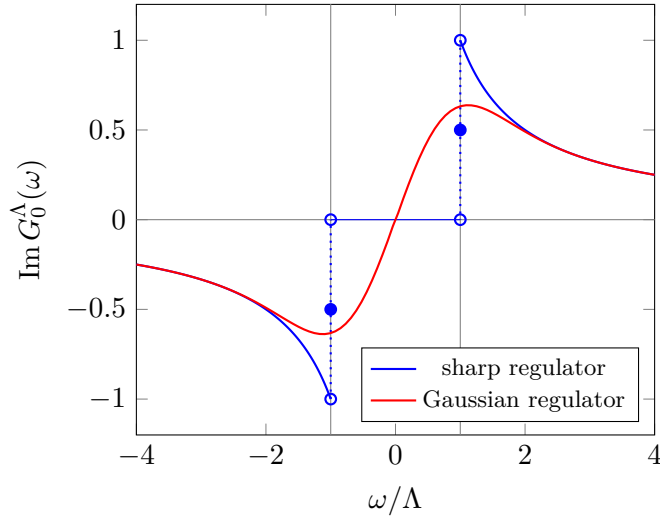


Figure 3.2: Shape of the scale-dependent Green's function $G_0^\Lambda(\omega)$ as a function of ω for two possible choices of regulator, the sharp cutoff using a Heaviside function (3.29) and the smooth Gaussian regulator function (3.30).

If the choice of regulator does not affect the calculated values of physical observables, this choice can be made based on technical considerations. The simplest choice for Θ^Λ is a sharp Heaviside function

$$\Theta^\Lambda(\omega) = \begin{cases} 0, & |\omega| < \Lambda \\ \frac{1}{2}, & |\omega| = \Lambda \\ 1, & |\omega| > \Lambda, \end{cases} \quad (3.29)$$

which is particularly easy to implement and simplifies the form of some integrals. However, the discontinuities at $|\omega| = \Lambda$ lead to some numerical difficulties in expressions that contain sums and products of multiple propagators, and we use a smooth (Gaussian) step function,

$$\Theta^\Lambda(\omega) = 1 - e^{-\omega^2/\Lambda^2}, \quad (3.30)$$

instead (see Fig. 3.2).

The scale-dependence of all other correlators can be understood in terms of a perturbation series as replacing all propagators G_0 by G_0^Λ in all diagrams. Therefore, in the parquet formalism (see Sec. 3.2), $G, \Sigma, G^{(4)}, \Gamma$ and $\gamma_{a,p,t}$ become scale-dependent as well. (For brevity, our notation does not display this scale dependence.) In the parquet approximation, the irreducible part R remains Λ -independent, since Γ_0 does not have any scale-dependence. Otherwise, for example when using an irreducible vertex R obtained from some other method, one still assumes R to be scale-independent [52].

3.3.2 Vertex flow

The dependence of G and Γ on Λ can be analyzed using the derivative $\partial_\Lambda = \frac{\partial}{\partial \Lambda}$, which we denote by a dot. The Λ -derivative of Γ is

$$\dot{\Gamma} = \partial_\Lambda \Gamma = \partial_\Lambda R + \sum_{r=a,p,t} \partial_\Lambda \gamma_r = \sum_{r=a,p,t} \dot{\gamma}_r. \quad (3.31)$$

Expanding γ_r using the Bethe–Salpeter equations (3.22), the vertex can be decomposed into r -irreducible components connected by r -channel loops. Using the same symbolic notation Π_r as in Eq. 3.23 for the r -channel pair propagator, this can be expressed as

$$\Gamma = I_r + \gamma_r = I_r + I_r \Pi_r I_r + I_r \Pi_r I_r \Pi_r I_r + \dots, \quad (3.32)$$

where all products are to be understood as matrix multiplication with respect to suitably chosen indices.

With this decomposition, the various parts of the derivative can be inspected separately:

$$\dot{\gamma}_r = \partial_\Lambda [I_r \Pi_r \Gamma] = \partial_\Lambda [I_r \Pi_r I_r + I_r \Pi_r I_r \Pi_r I_r + \dots] \quad (3.33)$$

All parts where the derivative acts on one of the propagator pairs Π_r have sums of repeated $I_r \Pi_r$ -patterns on the left and right side, which can be reassembled to a full vertex. This part is called the *one-loop contribution* [54]

$$\dot{\gamma}_r^{(1)} = (I_r + I_r \Pi_r I_r + \dots) \dot{\Pi}_r (I_r + I_r \Pi_r I_r + \dots) = \Gamma \dot{\Pi}_r \Gamma = \Gamma (\dot{G}G + G\dot{G}) \Gamma \quad (3.34)$$

since it contains one fermion ‘loop’ Π_r connecting full vertices.

The remaining parts are those where the derivative acts on one of the irreducible vertices I_r . By the same principle as above, the non-differentiated parts can be reassembled to full vertices, simplifying Eq. (3.33) to [52]

$$\dot{\gamma}_r = \dot{\gamma}_r^{(1)} + \dot{I}_r \Pi_r \Gamma + \Gamma \Pi_r \dot{I}_r \Pi_r \Gamma + \Gamma \Pi_r \dot{I}_r. \quad (3.35)$$

Since $\Gamma = R + \sum_r \gamma_r$ and $\dot{R} = 0$ in the parquet approximation,

$$\partial_\Lambda I_r = \partial_\Lambda (\Gamma - \gamma_r) = \sum_{r' \neq r} \dot{\gamma}_{r'}, \quad (3.36)$$

which again contains an infinite number of terms.

The summation can be further organized by the total number of fermion loops Π_r contained in each contribution. All terms that contain two loops in total are $\dot{\gamma}_{r'}^{(1)}$ contributions to $\partial_\Lambda I_r$ in the second or last term of Eq. (3.35). This contribution is called the *two-loop contribution* [54]

$$\dot{\gamma}_r^{(2)} = \sum_{r' \neq r} \dot{\gamma}_{r'}^{(1)} \Pi_r \Gamma + \Gamma \Pi_r \sum_{r' \neq r} \dot{\gamma}_{r'}^{(1)} = \dot{\gamma}_{\bar{r}}^{(1)} \Pi_r \Gamma + \Gamma \Pi_r \dot{\gamma}_{\bar{r}}^{(1)}, \quad (3.37)$$

3.3. Multiloop functional renormalization group

where $\dot{\gamma}_{\bar{r}}^{(1)} = \sum_{r' \neq r} \dot{\gamma}_{r'}^{(1)}$.

Taking $\dot{\gamma}_{\bar{r}}^{(2)}$ contributions instead of $\dot{\gamma}_{\bar{r}}^{(1)}$ results in a three-loop contribution. There is another three-loop contribution that occurs when considering $\dot{\gamma}_{\bar{r}}^{(1)}$ contributions to the third term of Eq. (3.35). Therefore, [54]

$$\dot{\gamma}_r^{(3)} = \dot{\gamma}_{\bar{r}}^{(2)} \Pi_r \Gamma + \Gamma \Pi_r \dot{\gamma}_{\bar{r}}^{(1)} \Pi_r \Gamma + \Gamma \Pi_r \dot{\gamma}_{\bar{r}}^{(2)}. \quad (3.38)$$

In fact, this construction is not limited to three loops: All contributions of an arbitrary loop order $\ell \geq 3$ can be constructed by adding one loop to the left or the right side of $\dot{\gamma}_{r'}^{(\ell-1)}$ and adding one loop to both sides of $\dot{\gamma}_{r'}^{(\ell-2)}$.

$$\dot{\gamma}_r^{(\ell)} = \dot{\gamma}_{\bar{r}}^{(\ell-1)} \Pi_r \Gamma + \Gamma \Pi_r \dot{\gamma}_{\bar{r}}^{(\ell-2)} \Pi_r \Gamma + \Gamma \Pi_r \dot{\gamma}_{\bar{r}}^{(\ell-1)} \quad (3.39)$$

Thus, all parts of $\dot{\gamma}_r$ have been organized into contributions $\dot{\gamma}_r^{(\ell)}$ and [54]

$$\dot{\gamma}_r = \sum_{\ell} \dot{\gamma}_r^{(\ell)}. \quad (3.40)$$

The iterative nature of Eq. (3.39) is convenient for numerical applications, since ℓ -loop contributions can be constructed from earlier iterations $\ell - 1$ and $\ell - 2$, thus avoiding repeated numerical effort. The vertex flow equations are presented in diagrammatic language in Table 3.1.

3.3.3 Self-energy flow

There are different ways of deriving the flow of the self-energy Σ , not all of which are immediately compatible with the parquet approximation [52, 54]. One derivation that avoids this problem uses the Λ -derivative of the Schwinger–Dyson equation (3.24)

$$\dot{\Sigma} = \partial_{\Lambda} \left[- \text{diagram} - \frac{1}{2} \text{diagram} \right]. \quad (3.41)$$

Again, the derivative can act on the propagators or the vertex in the second term and both parts will be analyzed separately. Since some parts involve lengthy algebra, not all steps in the derivation will be presented; they can be found in the work by Kugler and von Delft [52].

Contributions from applying ∂_{Λ} to the propagators are

$$\dot{\Sigma}_G = - \text{diagram} - \frac{1}{2} \left[\text{diagram} + \text{diagram} + \text{diagram} \right], \quad (3.42)$$

3. Method

1-loop contributions

$$\begin{aligned}
 \hat{\gamma}_a^{(1)} &= \text{[diagram 1]} + \text{[diagram 2]} & \hat{\gamma}_t^{(1)} &= -\text{[diagram 3]} - \text{[diagram 4]} \\
 \hat{\gamma}_p^{(1)} &= \frac{1}{2} \text{[diagram 5]} + \frac{1}{2} \text{[diagram 6]}
 \end{aligned}$$

2-loop contributions

$$\begin{aligned}
 \hat{\gamma}_a^{(2)} &= \text{[diagram 1]} + \text{[diagram 2]} & \hat{\gamma}_t^{(2)} &= -\text{[diagram 3]} - \text{[diagram 4]} \\
 \hat{\gamma}_p^{(2)} &= \frac{1}{2} \text{[diagram 5]} + \frac{1}{2} \text{[diagram 6]}
 \end{aligned}$$

contributions of order $\ell \geq 3$

$$\begin{aligned}
 \hat{\gamma}_a^{(\ell)} &= \text{[diagram 1]} + \text{[diagram 2]} + \text{[diagram 3]} \\
 \hat{\gamma}_p^{(\ell)} &= \frac{1}{2} \text{[diagram 4]} + \frac{1}{4} \text{[diagram 5]} + \frac{1}{2} \text{[diagram 6]} \\
 \hat{\gamma}_t^{(\ell)} &= -\text{[diagram 7]} + \text{[diagram 8]} - \text{[diagram 9]}
 \end{aligned}$$

Table 3.1: Vertex flow in the multiloop functional renormalization group in diagrammatic language [54]. Lines $\#$ correspond to differentiated propagators $\partial_\Lambda G^\Lambda$.

3.3. Multiloop functional renormalization group

where \dot{G} is represented by $\text{---}\blacklozenge\text{---}$. Using $\gamma_r = I_r \Pi_r \Gamma \stackrel{\text{PA}}{=} (\Gamma_0 + \gamma_{\bar{r}}) \Pi_r \Gamma$,

$$\begin{aligned} \dot{\Sigma}_G &= -\text{---}\blacklozenge\text{---} - \text{---}\gamma_a\text{---} - \text{---}\gamma_p\text{---} + \text{---}\gamma_{\bar{a}}\text{---} + \frac{1}{2} \text{---}\gamma_{\bar{p}}\text{---} \\ &= -\text{---}I_t\text{---} + \text{---}\gamma_{\bar{a}}\text{---} + \frac{1}{2} \text{---}\gamma_{\bar{p}}\text{---}. \end{aligned} \quad (3.43)$$

Applying ∂_Λ to the vertex parts in Eq. (3.41) yields

$$\dot{\Sigma}_\Gamma = -\frac{1}{2} \left[\text{---}\blacklozenge\text{---}\gamma_a + \text{---}\blacklozenge\text{---}\dot{\gamma}_p + \text{---}\blacklozenge\text{---}\dot{\gamma}_t \right]. \quad (3.44)$$

The vertex and its reducible parts are antisymmetric under exchange of two incoming or two outgoing arguments [52, 86].

$$\Gamma(1', 2'; 1, 2) = -\Gamma(1', 2'; 2, 1) = -\Gamma(2', 1'; 1, 2) \quad (3.45a)$$

$$\Gamma_0(1', 2'; 1, 2) = -\Gamma_0(1', 2'; 2, 1) = -\Gamma_0(2', 1'; 1, 2) \quad (3.45b)$$

$$\gamma_a(1', 2'; 1, 2) = -\gamma_t(1', 2'; 2, 1) = -\gamma_t(2', 1'; 1, 2) \quad (3.45c)$$

$$\gamma_p(1', 2'; 1, 2) = -\gamma_p(1', 2'; 2, 1) = -\gamma_p(2', 1'; 1, 2) \quad (3.45d)$$

Due to these so-called *crossing symmetries*, the first and last term in Eq. (3.44) are equal. With $\gamma_r = I_r \Pi_r \Gamma = (\Gamma^0 + \gamma_{\bar{r}}) \Pi_r \Gamma$,

$$\begin{aligned} \dot{\Sigma}_\Gamma &= -\text{---}I_a\text{---}\dot{\gamma}_a + \text{---}\gamma_{\bar{a}}\text{---}\dot{\gamma}_a - \frac{1}{2} \text{---}I_p\text{---}\dot{\gamma}_p + \frac{1}{2} \text{---}\gamma_{\bar{p}}\text{---}\dot{\gamma}_p \\ &= -\text{---}I_a\text{---}\dot{\gamma}_a + \text{---}\gamma_a\text{---}\dot{I}_a - \frac{1}{2} \text{---}I_p\text{---}\dot{\gamma}_a + \frac{1}{2} \text{---}\gamma_p\text{---}\dot{I}_p. \end{aligned} \quad (3.46)$$

Inserting the vertex flow from Eq. (3.39) and Eq. (3.40) for $\dot{\gamma}_r$ yields

$$\begin{aligned} \dot{\Sigma}_\Gamma &= - \left[\text{---}\gamma_a\text{---} + \text{---}\gamma_a\text{---} \right] - \text{---}\gamma_{\bar{a}}\text{---} \\ &\quad - \frac{1}{2} \left[\text{---}\gamma_p\text{---} + \text{---}\gamma_p\text{---} \right] - \frac{1}{4} \text{---}\gamma_{\bar{p}}\text{---}. \end{aligned} \quad (3.47)$$

3. Method

For convenience, we define the *center part*

$$\begin{array}{c} \text{Diagram: A central square with a top cap labeled } \dot{\gamma}_{\bar{t}}^{(C)} \text{ and a bottom cap labeled } \dot{\gamma}_{\bar{p}} \text{ is equal to the sum of two terms. The first term is a chain of three squares with a top cap labeled } \dot{\gamma}_{\bar{a}} \text{ and a bottom cap labeled } \dot{\gamma}_{\bar{p}}. The second term is a chain of three squares with a top cap labeled } \dot{\gamma}_{\bar{p}} \text{ and a bottom cap labeled } \dot{\gamma}_{\bar{p}}. \end{array} \quad (3.48)$$

Due to crossing symmetries, the last two terms of $\dot{\Sigma}_G$ in Eq. (3.43) cancel $\dot{\Sigma}_\Gamma$ except for the center part:

$$\dot{\Sigma} = \dot{\Sigma}_G + \dot{\Sigma}_\Gamma = - \begin{array}{c} \text{Diagram: A square with a top cap labeled } \dot{\gamma}_{\bar{t}} \end{array} - \begin{array}{c} \text{Diagram: A square with a top cap labeled } \dot{\gamma}_{\bar{t}}^{(C)} \end{array}. \quad (3.49)$$

The derivative of G is

$$\dot{G} = \partial_\Lambda \frac{1}{(G_0^\Lambda)^{-1} - \Sigma} = G \left[-\partial_\Lambda (G_0^\Lambda)^{-1} \right] G + G \dot{\Sigma} G. \quad (3.50)$$

We define the *single-scale propagator*⁷

$$S = G \left[-\partial_\Lambda (G_0^\Lambda)^{-1} \right] G. \quad (3.51)$$

As the derivative of the propagator (3.50) contains $\dot{\Sigma}$, Eq. (3.49) has $\dot{\Sigma}$ on both sides. Iterating Eq. (3.49) generates chains of $I_t \Pi_t$, which are capped by either a single-scale propagator or a $\dot{\gamma}_{\bar{t}}^{(C)}$ -term. The chains can then be reassembled to full vertices and [52, 54]

$$\dot{\Sigma} = - \begin{array}{c} \text{Diagram: A square with a top cap labeled } \dot{\gamma}_{\bar{t}} \end{array} - \begin{array}{c} \text{Diagram: A square with a top cap labeled } \dot{\gamma}_{\bar{t}}^{(C)} \end{array} - \begin{array}{c} \text{Diagram: A square with a top cap labeled } \dot{\gamma}_{\bar{t}}^{(C)} \text{ and a bottom cap labeled } \dot{\gamma}_{\bar{p}} \end{array}, \quad (3.52)$$

where the single-scale propagator is represented by \dashv .

3.3.4 Integrating the renormalization group flow

Thus, $\dot{\Gamma}$ and $\dot{\Sigma}$ are known for given Γ, Σ . A given state $\Psi = (\Gamma, \Sigma)$ at some $\Lambda = \Lambda_i$ can be evolved to a target Λ_f by solving an ordinary differential equation (ODE)

$$\partial_\Lambda \Psi = f(\Psi) \Big|_\Lambda. \quad (3.53)$$

The initial condition $\Psi|_{\Lambda_i} = (\Gamma|_{\Lambda_i}, \Sigma|_{\Lambda_i})$ can be chosen in different ways. One obvious way is to choose a Λ_i much larger than all other energy scales in the

⁷The name refers to the fact that $S \sim \delta(|\omega| - \Lambda)$ when using a sharp cutoff function Θ^Λ in the propagator (3.28).

3.3. Multiloop functional renormalization group

system and insert the $\lim_{\Lambda \rightarrow \infty} G_0^\Lambda = 0$ into the action (3.11). This immediately implies $\Gamma|_{\Lambda_i} = \Gamma_0$, since all other diagrams are suppressed by G_0^Λ [54, 55, 75]. Alternatively, the initial condition can be set equal to an approximation for the full vertex and self-energy obtained by other methods such as perturbation theory or dynamical mean-field theory (DMFT)⁸. Since the multiloop flow was constructed in accordance with the parquet method, we use a solution of the parquet equations for some large value of Λ_i as initial condition. The method used to solve the parquet equations will be discussed in Sec. 3.3.5.

There are several well-known algorithms for solving ODEs numerically⁹, such as the Runge–Kutta family of algorithms [88–90]. As Γ and Σ may change rapidly or start to diverge at some Λ comparable to J while behaving smoothly for $\Lambda > J$, it is advisable to use an error-estimating adaptive method, such as the 5th-order method of Cash and Karp [88]. These methods proceed iteratively from the initial to final Λ via intermediate steps Λ_m , where the size of the next step $\Lambda_{m+1} - \Lambda_m$ is adjusted after each iteration m . Assuming that the difficulty of the problem changes slowly, a heuristic can be used to predict the approximate error of the next step as a function of step size based on the estimated error in the last step. The step size may be decreased to reduce numerical error if the error threatens to become unacceptably large, or the step size may be increased to reduce numerical effort if the heuristic is confident that a sufficiently accurate step can be calculated.

For practical reasons, implementations of adaptive Runge–Kutta methods are inefficient if the difficulty of the problem is drastically different at different (not necessarily similar) Λ . Underestimation of the error in the step-size prediction heuristic may lead to very large steps that induce instabilities or miss features of the ODE entirely. Therefore, the heuristic must be adjusted such that appropriate step sizes are chosen in the most difficult part of the ODE, which leads to inefficient choices in less difficult parts. The integration of the pseudofermion fRG flow is such a problem: At $\Lambda/J > 1$, the appropriate step size (e.g. $\Lambda/J = 4.5$ to 3.7) is much larger than at smaller $\Lambda/J \ll 1$ (e.g. $\Lambda/J = 0.074$ to 0.066). This issue can be avoided by a change of variables in the flow equation Eq. (3.53). Introducing a variable t and an invertible function $\Lambda(t)$, Eq. (3.53) can be expressed as

$$\partial_t \Psi = \left. \frac{\partial \Lambda(t)}{\partial t} \right|_t f(\Psi) \Big|_{\Lambda(t)} \equiv \tilde{f}(\Psi) \Big|_t. \quad (3.54)$$

It is more efficient to integrate \tilde{f} in t if the function $\Lambda(t)$ has been chosen such that the appropriate step size in t is similar at all values of t . In pseudofermion fRG problems, this is roughly the case if $t \sim \log(\Lambda/J)$. We choose

$$\Lambda(t) = J e^{-t} \quad (3.55)$$

⁸The combination of DMFT and fRG is known as ‘DMF²RG’ [87].

⁹These algorithms are also known as ‘time integration’ algorithms.

3. Method

and integrate from $t = -\log(\Lambda_i/J)$ to ∞ .

In each Runge–Kutta step, most of the runtime is spent evaluating the frequency integrals in the expressions for $\dot{\Gamma}$ and $\dot{\Sigma}$. Therefore, within the adaptive Runge–Kutta methods, a higher-order method is thus generally preferable¹⁰, as the increase in the number of function evaluations is more than compensated by the increase in step size and the overhead of the ODE solver is negligible compared to the evaluation of $\dot{\Gamma}, \dot{\Sigma}$. In practice, we use the 5th-order method of Cash and Karp [88].

3.3.5 Parquet solutions at finite Λ

Since the multiloop flow was constructed to be compatible with the parquet equations, using a parquet solution as initial condition should lead to a flow along parquet solutions to the system at each Λ . At sufficiently high Λ , correlations are suppressed by small G_0^Λ . It is therefore possible to quite easily find a self-consistent solution of the parquet equations at large $\Lambda \gg J$ even for systems which are difficult to solve at $\Lambda \lesssim J$. To find this self-consistent parquet solution $\Psi_{\text{parquet}} = (\Gamma_{\text{parquet}}, \Sigma_{\text{parquet}})$, we regard the parquet equations as describing a fixed point

$$\Psi_{\text{parquet}} = F(\Psi_{\text{parquet}}) \quad (3.56)$$

of a function F given by the right-hand side of the parquet equations for γ_r and Σ . We then find this fixed point by iterating¹¹ [91]

$$\Psi_{M+1} = z F(\Psi_M) + (1 - z) \Psi_M \quad (3.57)$$

with a mixing factor z that is generally between 10^{-3} and 10^{-1} . For well-behaved F , this iteration converges to a fixed point $\Psi_M \rightarrow \Psi_{\text{parquet}}$, which is detected by vanishing¹² $\|F(\Psi_M) - \Psi_M\|$.

¹⁰While, as Reuther [48] reported, the Euler method is able to perform the Λ -integration, we found that higher-order adaptive Runge–Kutta methods offer many advantages such as gain in stability and numerical efficiency when compared to non-adaptive Euler integration. Furthermore, the error-estimating capabilities of these methods are able to detect difficulties in the flow, such as the onset of divergence, where non-adaptive methods would silently emit inaccurate values that are difficult to interpret.

¹¹There are more sophisticated methods to find fixed points that converge faster and for a larger class of functions, such as Anderson acceleration [91] or (generalized) Broyden’s methods [92, 93]. These have not been implemented since the fixed-point iteration with simple mixing already converges at sufficiently large Λ .

¹²Our implementation uses a maximum norm to detect convergence.

Implementation

Though the general method was described in the previous chapter, there are some non-obvious problems that arise in a practical implementation. This chapter shows how to avoid such problems as well as a few methods to speed up the algorithm. The first section deals with a clever parametrization of the vertex that is crucial to the practical success of this method. Thereafter, we present fully parametrized expressions for the loop and bubble functions which can be used as building blocks for the parquet equations as well as the mfRG flow. In the last section, a parametrized expression for the spin susceptibility is derived, as it cannot be constructed from these building blocks in an efficient way.

4.1 Parametrization of vertices and propagators

The pseudofermion fRG vertex is constrained by many symmetries which reduce the number of independent components. Any implementation should exploit as many of these symmetries as possible to reduce the numerical effort required. For the systems considered in this thesis, only about 1/100 of all components of the vertex are independent.

Several types of symmetries are relevant here, namely [86]

- gauge redundancy of the parton construction
- physical symmetries of the Hamiltonian
- lattice symmetries

and the effect of each of these symmetries will be described in the following sections. The basic idea is to evaluate only the independent components of all expressions and generate other components as needed using symmetry transforms. Efficiency can be further improved by decomposing the vertex into several components with different asymptotic structure in their frequency dependence [94]. Both symmetries and asymptotic structure have to be taken into account to find an efficient parametrization in frequency space. Lattice symmetries will be considered separately in Sec. 4.1.5, as the parametrization

4. Implementation

of the vertex in frequency space and in real space are independent of each other.

4.1.1 SU(2) gauge redundancy of the parton construction

Usually, the parton or Abrikosov pseudofermion construction is expressed as

$$S_i^\mu \rightarrow \frac{1}{2} \mathbf{f}_i^\dagger \sigma^\mu \mathbf{f}_i, \quad \text{where} \quad \mathbf{f}_i = \begin{pmatrix} f_{i\uparrow} \\ f_{i\downarrow} \end{pmatrix}. \quad (4.1)$$

The SU(2) redundancy is not very obvious in the above equation. It can be rewritten as a trace over a product of matrices [86, 95]

$$S_i^\mu \rightarrow \frac{1}{4} \text{Tr} \left(F_i^\dagger \sigma^\mu F_i \right), \quad \text{where} \quad F_i = \begin{pmatrix} f_{i\uparrow} & f_{i\downarrow}^\dagger \\ f_{i\downarrow} & -f_{i\uparrow}^\dagger \end{pmatrix}. \quad (4.2)$$

This construction is invariant under right-multiplication of F_i with a local matrix $g_i \in \text{SU}(2)$,

$$F_i \rightarrow F_i g_i, \quad (4.3)$$

due to the cyclic structure of the trace and $g_i g_i^\dagger = 1$. It is convenient to analyze this SU(2) symmetry as a composition of a U(1) and a particle-hole symmetry.

U(1) symmetry

Restricting the discussion to complex phases

$$g_i = \begin{pmatrix} e^{i\phi_i} & \\ & e^{-i\phi_i} \end{pmatrix} \in \text{SU}(2) \quad (4.4)$$

for the moment, this implies

$$\langle f_{i_1\alpha_1}^\dagger f_{i_1\alpha_1} \rangle = e^{i\phi_{i_1} - i\phi_{i_1'}} \langle f_{i_1\alpha_1}^\dagger f_{i_1\alpha_1} \rangle, \quad (4.5)$$

$$\langle f_{i_1\alpha_1}^\dagger f_{i_2\alpha_2}^\dagger f_{i_2\alpha_2} f_{i_1\alpha_1} \rangle = e^{i\phi_{i_1} + i\phi_{i_2} - i\phi_{i_2'} - i\phi_{i_1'}} \langle f_{i_1\alpha_1}^\dagger f_{i_2\alpha_2}^\dagger f_{i_2\alpha_2} f_{i_1\alpha_1} \rangle, \quad (4.6)$$

which is only true if the phases ϕ cancel or the correlator is zero. Since these phases ϕ can be chosen arbitrarily and independently for each lattice site, it follows that the propagator must be local,

$$G(1', 1) = \delta_{i_1' i_1} G(1', 1), \quad (4.7)$$

and the 4-point correlator must be bi-local,

$$G^{(4)}(1', 2'; 1, 2) = \delta_{i_1' i_1} \delta_{i_2' i_2} G(1', 2'; 1, 2) - \delta_{i_2' i_1} \delta_{i_1' i_2} G(2', 1'; 1, 2). \quad (4.8)$$

Both relations together imply that the vertex must be bi-local as well [86],

$$\Gamma(1', 2'; 1, 2) = \delta_{i_1' i_1} \delta_{i_2' i_2} \Gamma(1', 2'; 1, 2) - \delta_{i_2' i_1} \delta_{i_1' i_2} \Gamma(2', 1'; 1, 2). \quad (4.9)$$

Particle-hole symmetry

Furthermore, there are transforms

$$\begin{pmatrix} & 1 \\ 1 & \end{pmatrix} \in \text{SU}(2) \quad (4.10)$$

that correspond to local particle-hole symmetry. These swap f and f^\dagger operators:

$$f_{i\uparrow} \leftrightarrow f_{i\downarrow}^\dagger, \quad f_{i\downarrow} \leftrightarrow -f_{i\uparrow}^\dagger. \quad (4.11)$$

For convenience, we introduce notation where spin indices α appear as coefficients. We define α to have the numeric values $+1$ for $\alpha = \uparrow$ and -1 for $\alpha = \downarrow$, such that Eq. (4.11) can be expressed as

$$f_{i\alpha} \leftrightarrow \alpha f_{i\bar{\alpha}}^\dagger. \quad (4.12)$$

We introduce further notation for multi-indices,

$$1 \equiv (i_1, \omega_1, \alpha_1), \quad (4.13a)$$

$$-1 \equiv (i_1, -\omega_1, \alpha_1), \quad (4.13b)$$

$$\bar{1} \equiv (i_1, \omega_1, \bar{\alpha}_1), \quad (4.13c)$$

where $\bar{\alpha}$ is the inverse of α . Invariance under particle-hole symmetry implies [86]

$$G(1', 1) = -\alpha'_1 \alpha_1 G(-\bar{1}, -\bar{1}') \quad (4.14)$$

and

$$G(1', 2'; 1, 2) \delta_{i'_1 i_1} \delta_{i'_2 i_2} = -\alpha'_1 \alpha_1 G(-\bar{1}, 2'; -\bar{1}', 2) \quad (4.15a)$$

$$= -\alpha'_2 \alpha_2 G(1', -\bar{2}; 1, -\bar{2}'). \quad (4.15b)$$

4.1.2 Physical symmetries

Instead of re-deriving symmetries on the correlators, we will list them as described in the work by Buessen et al. [86].

Time reversal

Time reversal symmetry can be implemented as [86]

$$f_{i\alpha} \rightarrow i\alpha f_{i\bar{\alpha}} \quad (4.16)$$

and implies [86]

$$G(1', 1) = \alpha'_1 \alpha_1 \left[G(-\bar{1}', -\bar{1}) \right]^*, \quad (4.17)$$

$$G(1', 2'; 1, 2) \delta_{i'_1 i_1} \delta_{i'_2 i_2} = \alpha'_1 \alpha'_2 \alpha_1 \alpha_2 \left[G(-\bar{1}', -\bar{2}'; -\bar{1}, -\bar{2}) \right]^*. \quad (4.18)$$

4. Implementation

Hermitian symmetry

If the Hamiltonian is hermitian, the correlators are further constrained by [86]

$$G(1', 1) = \alpha'_1 \alpha_1 G(\bar{1}; \bar{1}') \quad (4.19)$$

and

$$G(1', 2'; 1, 2) \delta_{i'_1 i_1} \delta_{i'_2 i_2} = \alpha'_1 \alpha'_2 \alpha_1 \alpha_2 G(\bar{1}, \bar{2}; \bar{1}', \bar{2}'). \quad (4.20)$$

SU(2) spin rotation

In Heisenberg models with equal interaction strength in all directions $J^{\mu\lambda} = J\delta^{\mu\lambda}$, the Hamiltonian is invariant under global spin rotations $g_{\text{spin}} \in \text{SU}(2)$

$$S^\mu \rightarrow g_{\text{spin}}^\dagger S^\mu g_{\text{spin}}, \quad (4.21)$$

which can be implemented for Abrikosov pseudofermions as [86, 95]

$$F_i \rightarrow g_{\text{spin}} F_i, \quad (4.22)$$

where the matrix F is the same as the one in Eq. (4.2). This symmetry under a *global* transformation g_{spin} of the spin operators is distinct from the *local* transformation g_i corresponding to the SU(2) gauge redundancy (4.3) of Abrikosov's pseudofermion representation, which does not change the spin operators.

In XXZ models, the symmetry between the S^z component and the other components is broken, reducing the SU(2) symmetry of a fully symmetric Heisenberg model to a U(1) symmetry within the S^x - S^y plane. In this case, the transformation matrices g_{spin} are constrained to

$$g_{\text{spin}} = \begin{pmatrix} e^{i\phi} & \\ & e^{-i\phi} \end{pmatrix}, \quad \phi \in \mathbb{R}. \quad (4.23)$$

4.1.3 Parametrized form of the propagator and self-energy

Combined, the various constraints on the propagator imply that it is diagonal in all arguments [86]:

$$G(1', 1) = \delta_{i'_1 i_1} \delta_{\omega'_1 \omega_1} \delta_{\alpha'_1 \alpha_1} G(\omega_1). \quad (4.24)$$

It is also purely imaginary and antisymmetric:

$$G(\omega) = -G(-\omega) \in i\mathbb{R}. \quad (4.25)$$

Due to Dyson's equation

$$G(1', 1) = G_0(1', 1) + G_0(1', 1') \Sigma(1', 1) G(1, 1), \quad (4.26)$$

the self-energy is constrained by the same symmetries as the propagator [75, 86]. We parametrize the self-energy as

$$\Sigma(1', 1) = \delta_{i'_1 i_1} \delta_{\omega'_1 \omega_1} \delta_{\alpha'_1 \alpha_1} \Sigma(\omega_1), \quad (4.27)$$

and Eq. (4.25) implies

$$\Sigma(\omega) = -\Sigma(-\omega) \in i\mathbb{R}. \quad (4.28)$$

Because of the simple structure of the propagator and the definition of the vertex,

$$\begin{aligned} G^{(4)}(1', 2'; 1, 2) &= G(1', 1) G(2', 2) - G(2', 1) G(1', 2) \\ &+ \sum_{3' 4' 3 4} G(1', 3') G(2', 4') \Gamma(3', 4'; 3, 4) G(3, 1) G(4, 2), \end{aligned} \quad (4.29)$$

all symmetries of the 4-point correlator $G(1', 2'; 1, 2)$ apply directly to the vertex $\Gamma(1', 2'; 1, 2)$ as well [86].

4.1.4 Parametrization of spin and site dependence of the vertex

This enables us to parametrize the 4-point vertex as [86]

$$\begin{aligned} \Gamma(1', 2'; 1, 2) &= \Gamma(i'_1, \omega'_1, \alpha'_1, i'_2, \omega'_2, \alpha'_2; i_1, \omega_1, \alpha_1, i_2, \omega_2, \alpha_2) = \\ &= \sum_{\mu, \lambda=0}^3 \left[\Gamma_{i'_1 i'_2}^{\sim \mu \lambda}(\omega'_1, \omega'_2; \omega_1, \omega_2) \sigma_{\alpha'_1 \alpha_1}^\mu \sigma_{\alpha'_2 \alpha_2}^\lambda \delta_{i'_1 i_1} \delta_{i'_2 i_2} \right. \\ &\quad \left. - \Gamma_{i'_1 i'_2}^{\circ \mu \lambda}(\omega'_1, \omega'_2; \omega_2, \omega_1) \sigma_{\alpha'_1 \alpha_2}^\mu \sigma_{\alpha'_2 \alpha_1}^\lambda \delta_{i'_1 i_2} \delta_{i'_2 i_1} \right] \delta_{\omega'_1 + \omega'_2, \omega_1 + \omega_2}, \end{aligned} \quad (4.30)$$

where i are site indices, ω are frequencies, $\alpha \in \{\uparrow, \downarrow\}$ are spin indices and $\{\sigma^\mu\}_{\mu \in \{0 \dots 3\}}$ are Pauli matrices with $\sigma_{\alpha' \alpha}^0 = \delta_{\alpha' \alpha}$. In the following, we use the notations $\mu = x, y, z$ and $\mu = 1, 2, 3$ interchangeably.

The same parametrization can be used for the reducible parts of the vertex. While $\tilde{\Gamma} = \Gamma^{(\circ)}$ for the full vertex because of crossing symmetries (see Eq. (3.45)), the reducible parts γ_a and γ_t are exchanged by this symmetry as $\tilde{\gamma}_a = \gamma_t^{(\circ)}$ and vice versa. In the following, $\tilde{\circ}$ - and \circ -components will be referred to explicitly only where necessary. Relations with omitted indices (including $\tilde{\circ}$ and \circ) hold separately for each component. In addition, the crossing symmetries impose constraints on the frequency structure of the reducible vertex parts, which are discussed in Sec. 4.1.6 after some further refinement to the parametrization.

If the interaction $J^{\mu\lambda}$ is diagonal in $\mu\lambda$, the vertex $\Gamma^{\mu\lambda}$ is diagonal in $\mu\lambda$ as well:

$$\Gamma^{\mu\lambda} = \delta^{\mu\lambda} \Gamma^\mu. \quad (4.31)$$

4. Implementation

This is because the initial vertex is proportional to J and the fRG flow for a vertex $\sim \delta^{\mu\lambda}$ does not generate off-diagonal terms. In Heisenberg models with isotropic coupling $J^{\mu\lambda} = J\delta^{\mu\lambda}$, there is additionally a $SU(2)$ spin rotation symmetry (4.21) of the Hamiltonian, which reduces independent spin components of the vertex to Γ^0 and $\Gamma^1 = \Gamma^2 = \Gamma^3$. In prior work [48, 49, 75, 96], the two components are referred to as the *density part* $\Gamma^d = \Gamma^0$ and *spin part* $\Gamma^s = \Gamma^1$ of the vertex. In an XXZ model, only the components $J^x = J^y$ are equal, leading to the reduced symmetry $\Gamma^1 = \Gamma^2 \neq \Gamma^3$ in the vertex.

Furthermore, the flow does not generate imaginary terms for real interaction strength $J^{\mu\lambda} \in \mathbb{R}$. Therefore, for hermitian Hamiltonians,

$$\Gamma_{i_1 i_2}^\mu(\dots) \in \mathbb{R} \quad (4.32)$$

as well. These properties of the flow are shown explicitly in Sec. 4.2.

In diagrams, vertices are denoted as boxes with lines connecting the indices at equal sites:

$$\Gamma(1', 2'; 1, 2) = \begin{array}{c} \begin{array}{ccc} & 2 & \\ & \swarrow & \searrow \\ & \square & \\ & \nwarrow & \nearrow \\ & 1' & \end{array} & , & \begin{array}{ccc} & 2' & \\ & \swarrow & \searrow \\ & \square & \\ & \nwarrow & \nearrow \\ & 1 & \end{array} \end{array} \quad (4.33)$$

$$\Gamma_{i_1 i_2}^{\tilde{\mu}}(\omega'_1, \omega'_2; \omega_1, \omega_2) \delta_{i'_1 i_1} \delta_{i'_2 i_2} \delta_{\omega'_1 + \omega'_2, \omega_1 + \omega_2} = \begin{array}{c} \begin{array}{ccc} & 2 & \\ & \swarrow & \searrow \\ & \square & \\ & \nwarrow & \nearrow \\ & 1' & \end{array} & \begin{array}{ccc} & 2' & \\ & \swarrow & \searrow \\ & \square & \\ & \nwarrow & \nearrow \\ & 1 & \end{array} \end{array} \quad (4.34)$$

Thus, Eq. (4.30) can be expressed diagrammatically as

$$\begin{array}{c} \begin{array}{ccc} & 2 & \\ & \swarrow & \searrow \\ & \square & \\ & \nwarrow & \nearrow \\ & 1' & \end{array} & \begin{array}{ccc} & 2' & \\ & \swarrow & \searrow \\ & \square & \\ & \nwarrow & \nearrow \\ & 1 & \end{array} \end{array} = \sum_{\mu=0}^3 \left[\begin{array}{c} \begin{array}{ccc} & 2 & \\ & \swarrow & \searrow \\ & \square & \\ & \nwarrow & \nearrow \\ & 1' & \end{array} & \begin{array}{ccc} & 2' & \\ & \swarrow & \searrow \\ & \square & \\ & \nwarrow & \nearrow \\ & 1 & \end{array} \end{array} \sigma_{\alpha'_1 \alpha_1}^\mu \sigma_{\alpha'_2 \alpha_2}^\mu - \begin{array}{c} \begin{array}{ccc} & 2 & \\ & \swarrow & \searrow \\ & \square & \\ & \nwarrow & \nearrow \\ & 1' & \end{array} & \begin{array}{ccc} & 2' & \\ & \swarrow & \searrow \\ & \square & \\ & \nwarrow & \nearrow \\ & 1 & \end{array} \end{array} \sigma_{\alpha'_1 \alpha_2}^\mu \sigma_{\alpha'_2 \alpha_1}^\mu \right]. \quad (4.35)$$

4.1.5 Lattice symmetries

Given some basis vectors $\mathbf{a}_1, \dots, \mathbf{a}_d \in \mathbb{R}^d$, a lattice in d dimensions can be constructed by repetition of a unit cell using a group of translation operators $\mathbb{T} = \{T_{\mathbf{r}}\}_{\mathbf{r} \in \mathbb{Z}^d}$ where $\mathbf{r} = (r^1, \dots, r^d)$ and the action of $T_{\mathbf{r}}$ is a translation by $\sum_{\alpha=1}^d r^\alpha \mathbf{a}_\alpha$. The group composition law is $T_{\mathbf{r}_1} T_{\mathbf{r}_2} = T_{(\mathbf{r}_1 + \mathbf{r}_2)}$. All unit cells contained in the lattice can be indexed by \mathbf{r} such that the operator $T_{\mathbf{r}}$ transforms the original unit cell to the unit cell being indexed.

In Hubbard or Heisenberg type models, the unit cell is a collection of sites connected by edges. We index the sites using $c \in \mathbb{J}_B \cong \{1, \dots, B\} \subset \mathbb{Z}$ and

each site can now be specified by a unique tuple $(\underline{r}, c) \in \mathbb{L} \equiv \mathbb{Z}^d \times \mathbb{J}_B$. The translation operators do not change the inner structure of each unit cell:

$$T_{\underline{j}}(\underline{r}, c) = (\underline{r} + \underline{j}, c). \quad (4.36)$$

The fRG vertex Γ is invariant under lattice translation operations¹, i.e. for two sites $i_1 \equiv (\underline{r}_1, c_1), i_2 \equiv (\underline{r}_2, c_2)$,

$$\Gamma_{i_1 i_2} = \Gamma_{c_1 c_2}(\underline{r}_1, \underline{r}_2) = T_{-\underline{r}_2} \Gamma_{c_1 c_2}(\underline{r}_1, \underline{r}_2) = \Gamma_{c_1 c_2}(\underline{r}_1 - \underline{r}_2, \underline{0}), \quad (4.37)$$

and only vertex components with $\underline{r}_2 = \underline{0}$ have to be kept in memory.

Most lattices have further symmetries that can be exploited to reduce both runtime and memory usage. All other symmetries Q must be bijective and compatible with lattice translation symmetries. Therefore, they are length-preserving symmetries, i.e. rotation and reflection operators composed with translation operators. For each lattice site i , a symmetry operator Q generates an orbit $\{i, Qi, Q^2i, \dots\}$. The vertex is symmetric under lattice symmetries,

$$\Gamma_{i_1 i_2} = Q\Gamma_{i_1 i_2} = \Gamma_{Qi_1 Qi_2}. \quad (4.38)$$

Therefore, vertex components on sites that are part of the same orbit are always equal and it is sufficient to evaluate and keep only one of these components.

A symmetry Q generally acts on both the translation index \underline{r} as well as the unit cell index c and the action on each part is strongly constrained by the compatibility with translation symmetries mentioned above. Because Q is bijective, its action on \mathbb{J}_B can only be a permutation P . There is a redundancy in the action of Q on the \mathbb{Z}^d part of the lattice, as for any symmetry Q , the operators in $Q\mathbb{T} = \{QT_{\underline{r}}\}_{\underline{r} \in \mathbb{Z}^d}$ are symmetries as well. For each family of such symmetry operators, it is sufficient to pick one operator and investigate its action on \mathbb{L} . Due to the length-preserving property, there is always an operator in $Q\mathbb{T}$ that acts on \mathbb{Z}^d like a linear operator U and a translation by \underline{j}_c , which may depend on the site index c of the original site. In total,

$$Q(\underline{r}, c) = (U\underline{r} + \underline{j}_c, Pc). \quad (4.39)$$

¹The ground state may break symmetries of the Hamiltonian. In this case, correlators including the 2-particle correlator and the vertex may lose a subset of the translation invariance. If this leads to an ordered state, correlations describing the corresponding instability will diverge as described in [48, 97], and this divergence is taken as an indicator for order. If the symmetry-broken state is not ordered, but a valence bond solid or similar state with correlations whose strength differs on different bonds, representing such a state is only possible by defining \underline{r}_2 to be part of a cluster of the required size. As the fRG flow equations are symmetric, such a state can only be investigated by introducing a bias to the initial state. This type of construction was used in standard pffRG to investigate Heisenberg models by Suttner et al. [98] and Iqbal et al. [50]. Due to the numerical effort required to evaluate such a scheme for the pyrochlore XXZ model in multiloop fRG, this approach was not pursued in the course of this thesis and all vertices considered here are invariant under all lattice symmetries.

4. Implementation

This form is useful to describe symmetry relations in practice, because the linear operator U can be expressed and analyzed as a matrix². With this decomposition, lattice symmetries of the vertex (4.38) impose constraints

$$\Gamma_{c_1 c_2}(\mathbf{r}_1, \mathbf{r}_2) = \Gamma_{P c_1 P c_2}(U \mathbf{r}_1 + \mathbf{j}_{c_1}, U \mathbf{r}_2 + \mathbf{j}_{c_2}), \quad (4.40)$$

which can be implemented directly once U and \mathbf{j}_c are known. Expressions for the symmetries of the pyrochlore lattice are given in Appendix A.

In total, to exploit lattice symmetries, it is necessary to input the following information manually:

1. A unit cell \mathbb{J}_B of the lattice and the corresponding basis vectors. It is advantageous to choose a unit cell that contains as few sites as possible and has similar length in all directions.
2. A generating set of symmetry operators Q of the lattice, where each Q is represented by a matrix U , a set of displacements $\{\mathbf{j}_1, \dots, \mathbf{j}_B\}$ and a permutation P . Compositions of these operators should describe all symmetries of the lattice.
3. The symmetry-reduced unit cell \mathbb{J}'_B that contains only those sites within the unit cell that are not related by any symmetry. For many lattices, including the kagome and pyrochlore lattice, \mathbb{J}'_B contains only one site.
4. For each site $i \in \mathbb{J}'_B$, declare which sites are coupled to i by the bare interaction in the Hamiltonian.

This information is sufficient to symmetry-reduce the real-space components of the vertex. For this, a lattice-generation algorithm first obtains all sites within a certain cutoff distance r_{\max} from the origin. It then applies all symmetry operators to each site and categorizes all sites into sets of sites that are symmetric to one another. For each of these sets, only one component of the vertex is kept in memory.

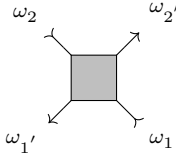
4.1.6 Asymptotic structure and natural frequency parametrization of the vertex

The parquet equations show that the vertex Γ is a sum of the fully irreducible part R and the reducible parts γ_a , γ_p and γ_t (see Eq. (3.20)). The reducible parts have asymptotic structure along different directions, which we call *natural frequency* directions [75, 94]. These natural frequencies ν_r, ν'_r, Ω_r will be used to parametrize the vertex in frequency space instead of $\omega'_1, \omega'_2, \omega_1, \omega_2$, which have to respect the constraint $\omega'_1 + \omega'_2 = \omega_1 + \omega_2$. Conversion formulae between the different frequency parametrizations are listed in Tab. 4.1.

The diagrams that contribute to each reducible vertex class can be classified by their asymptotic behavior in the limits $\nu_r \rightarrow \pm\infty$ and $\nu'_r \rightarrow \pm\infty$.

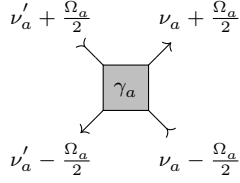
²As the operator U acts on index tuples $\in \mathbb{Z}^d$ which are defined depending on unit vectors $\mathbf{a}_1, \dots, \mathbf{a}_d$, the matrix representing U may have very different entries compared to the matrix that represents an equivalent operation in real space. For specific examples, see Appendix A.

fermionic frequencies



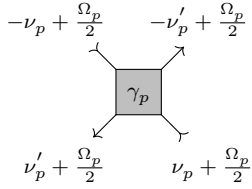
$$\begin{aligned}\omega'_1 &= \nu'_a - \frac{\Omega_a}{2} = \nu'_p + \frac{\Omega_p}{2} = \nu_t + \frac{\Omega_t}{2} \\ \omega'_2 &= \nu_a + \frac{\Omega_a}{2} = -\nu'_p + \frac{\Omega_p}{2} = \nu'_t - \frac{\Omega_t}{2} \\ \omega_1 &= \nu_a - \frac{\Omega_a}{2} = \nu_p + \frac{\Omega_p}{2} = \nu_t - \frac{\Omega_t}{2} \\ \omega_2 &= \nu'_a + \frac{\Omega_a}{2} = -\nu_p + \frac{\Omega_p}{2} = \nu'_t + \frac{\Omega_t}{2}\end{aligned}$$

a-channel



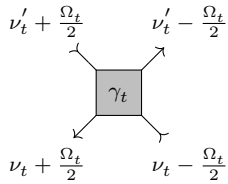
$$\begin{aligned}2\nu'_a &= \omega'_1 + \omega_2 = \nu'_p - \nu_p + \Omega_p = \nu'_t + \nu_t + \Omega_t \\ 2\nu_a &= \omega'_2 + \omega_1 = \nu_p - \nu'_p + \Omega_p = \nu'_t + \nu_t - \Omega_t \\ \Omega_a &= \omega_2 - \omega'_1 = -\nu'_p - \nu_p = \nu'_t - \nu_t\end{aligned}$$

p-channel



$$\begin{aligned}2\nu'_p &= \omega'_1 - \omega'_2 = \nu'_a - \nu_a - \Omega_a = \nu_t - \nu'_t + \Omega_t \\ 2\nu_p &= \omega_1 - \omega_2 = \nu_a - \nu'_a - \Omega_a = \nu_t - \nu'_t - \Omega_t \\ \Omega_p &= \omega_1 + \omega_2 = \nu'_a + \nu_a = \nu'_t + \nu_t\end{aligned}$$

t-channel



$$\begin{aligned}2\nu'_t &= \omega'_2 + \omega_2 = \nu'_a + \nu_a + \Omega_a = -\nu'_p - \nu_p + \Omega_p \\ 2\nu_t &= \omega'_1 + \omega_1 = \nu'_a + \nu_a - \Omega_a = \nu'_p + \nu_p + \Omega_p \\ \Omega_t &= \omega'_1 - \omega_1 = \nu'_a - \nu_a = \nu'_p - \nu_p\end{aligned}$$

Table 4.1: Natural frequency convention for reducible vertices and conversion formulae.

4. Implementation

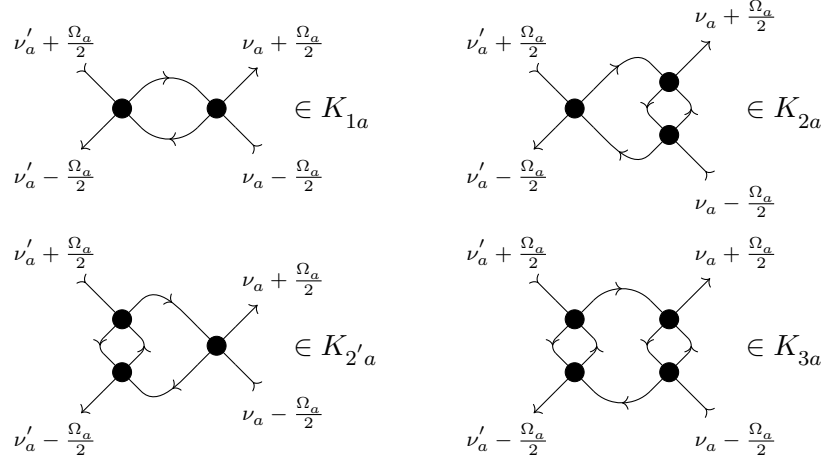


Figure 4.1: Examples for diagrams reducible in the a -channel that belong to the asymptotic classes $K_{1a}, K_{2a}, K_{2'a}, K_{3a}$.

The asymptotic behavior of each diagram is dictated by the manner in which the external legs are connected to bare vertices, as the bare vertex by itself does not have any frequency dependence. If two external legs are connected to the same bare vertex, the contribution of that diagram is depends only on either the difference (a - and t -channel) or the sum (p -channel) of the frequency arguments of those external propagators. In each channel, the natural frequency arguments are chosen such that the frequency Ω_r parametrizes this dependence, while ν_r and ν'_r correspond to an offset that does not affect the bare vertex. Thus, a diagram is independent of ν_r if the external legs on one side connect to the same bare vertex and independent of ν'_r if the external legs on the other side connect to the same bare vertex. We label these diagrammatic classes $K_{1r}^{\Omega_r}, K_{2r}^{\Omega_r, \nu_r}, K_{2'r}^{\Omega_r, \nu'_r}$ and $K_{3r}^{\Omega_r, \nu_r, \nu'_r}$. These classes are disjoint and for each channel $r \in \{a, p, t\}$, the reducible vertex is just the sum of the asymptotic classes³, i.e. [75, 94]

$$\gamma_r^{\mu; \Omega_r, \nu_r, \nu'_r} = K_{1r}^{\mu; \Omega_r} + K_{2r}^{\mu; \Omega_r, \nu_r} + K_{2'r}^{\mu; \Omega_r, \nu'_r} + K_{3r}^{\mu; \Omega_r, \nu_r, \nu'_r}. \quad (4.41)$$

Examples for each class of diagram in the a -channel are shown in Fig. 4.1.

As the external frequency arguments of propagators not connected to the same vertex always end up as part of the frequency arguments of internal propagators, asymptotic classes that are dependent on some frequency vanish in the limit where that frequency $\rightarrow \infty$ [75, 94]. Therefore,

$$\lim_{\nu_r \rightarrow \infty} \lim_{\nu'_r \rightarrow \infty} \gamma_r^{\mu; \Omega_r, \nu_r, \nu'_r} = K_{1r}^{\mu; \Omega_r}, \quad (4.42a)$$

³In a slight abuse of notation, we use the symbols $K_1, K_2, K_{2'}, K_3$ for both the set of diagrams in an asymptotic class and for the sum of these diagrams.

$$\lim_{\nu_r' \rightarrow \infty} \gamma_r^{\mu; \Omega_r, \nu_r, \nu_r'} = K_{1r}^{\mu; \Omega_r} + K_{2r}^{\mu; \Omega_r, \nu_r}, \quad (4.42b)$$

$$\lim_{\nu_r \rightarrow \infty} \gamma_r^{\mu; \Omega_r, \nu_r, \nu_r'} = K_{1r}^{\mu; \Omega_r} + K_{2r'}^{\mu; \Omega_r, \nu_r'}. \quad (4.42c)$$

The asymptotic classes in each channel are constrained by the symmetries listed in Sec. 4.1.1 and 4.1.2 as well as the crossing symmetries given in Eq. (3.45). Deriving symmetry relations for these asymptotic classes from symmetries of the reducible vertex components can be done most easily by inserting the natural frequency parametrization and taking one of the limits given in Eq. (4.42). As this procedure is straightforward, but somewhat lengthy, we do not show it explicitly here. The results are given elsewhere [51, Appendix B]. Equivalent symmetry relations have been derived independently by Kiese et al. as well [57, Appendix C]. These symmetries reduce the number of independent components drastically. Additionally, antisymmetry of the vertex component $\gamma_t^{0; \Omega_t, \nu_t, \nu_t'}$ in its fermionic frequency arguments ν_t and ν_t' implies

$$\gamma_t^{0; \Omega_t, \nu_t, \nu_t'} = K_{3t}^{-0; \Omega_t, \nu_t, \nu_t'}, \quad (4.43)$$

as all other components are equal to 0 at all frequencies [51].

The relations in Eq. (4.42) are crucial when constructing a numerical frequency mesh to sample the frequency dependence of the vertices. Using the asymptotic falloff $\rightarrow 0$, it is possible to choose boundaries for each class that contain all structures in the vertex which are larger than a given cutoff value. As these structures change during the flow, it is crucial to dynamically adjust these meshes after each Λ integration step. In principle, any choice of frequency mesh and dynamic adjustment algorithm that leads to sufficient resolution of all features at all values of Λ can be used for this. However, we encountered many subtle problems during implementation of the frequency meshes, and a very detailed description of our method is therefore included in this thesis as Appendix B.

4.2 Parametrized building blocks for the XXZ model

The multiloop functional renormalization group flow equations (see Tab. 3.1) relate derivatives of reducible vertex parts to diagrams that contain vertices connected by propagator bubbles. The propagators forming each bubble are either two full propagators G or one propagator G and one differentiated propagator \dot{G} . Therefore, to get the fully parametrized form of these equations, it is sufficient to parametrize the bubbles in the a , p and t channel, insert the required vertex parts, and replace G by \dot{G} as needed [48, 75]. Similarly, the fully parametrized self-energy flow equation (3.52) can be obtained by inserting appropriate vertex parts and propagators into the fully parametrized self-energy loop, which will be derived in the next section.

4. Implementation

Due to the bi-local nature of the vertex (see Eq. (4.9)), the fully parametrized bubble functions consist of a sum of two terms. One of these terms is proportional to $\delta_{i_1' i_1} \delta_{i_2' i_2}$, which we denote as \simeq , and the other is proportional to $\delta_{i_2' i_1} \delta_{i_1' i_2}$, which we denote as \succ . The crossing symmetries (3.45) relate all \succ -components to \simeq -components and it is therefore unnecessary to evaluate \succ -components explicitly.

4.2.1 Self-energy loop

We define the self-energy loop as

$$L[\Gamma, G](1', 1) = - \sum_2 \Gamma(1', 2; 1, 2) G(2) = - \sum_{1'} \left[\text{diagram} \right], \quad (4.44)$$

where the sign has been chosen according to the convention of Kugler and von Delft [54]. The fully parametrized form can be found by inserting the parametrized vertex from Eq. (4.30) and using the algebra of Pauli matrices:

$$\begin{aligned} L[\Gamma, G](1', 1) &= - \sum_{1'} \left[\text{diagram} \right] \\ &= - \frac{1}{\beta} \sum_{\omega_2} \sum_{\mu=0}^3 \left[\sum_{i_2} \left[\text{diagram} \right] \sum_{\alpha_2} \sigma_{\alpha_2 \alpha_2}^\mu \sigma_{\alpha_1' \alpha_1}^\mu - \sum_{i_2} \left[\text{diagram} \right] \sum_{\alpha_2} \sigma_{\alpha_1' \alpha_2}^\mu \sigma_{\alpha_2 \alpha_1}^\mu \right] = \\ &= - \frac{1}{\beta} \sigma_{\alpha_1' \alpha_1}^0 \sum_{\omega_2} \left[2 \sum_{i_2} \left[\text{diagram} \right] - \sum_{\mu=0}^3 \sum_{1'} \left[\text{diagram} \right] \right]. \quad (4.45) \end{aligned}$$

Translated back into symbolic language, this is

$$L[\Gamma, G](1', 1) = - \frac{1}{\beta} \sigma_{\alpha_1' \alpha_1}^0 \sum_{\omega_2} \left[2 \sum_{i_2} \Gamma_{i_1' i_2}^{\simeq 0}(\omega_1', \omega_2; \omega_1, \omega_2) - \sum_{\mu=0}^3 \Gamma_{i_1' i_1}^{\succ \mu}(\omega_1', \omega_2; \omega_1, \omega_2) \right] G(\omega_2). \quad (4.46)$$

4.2.2 a -bubble

Starting from the definition of the a -bubble

$$\begin{aligned}
 B_a(1', 2'; 1, 2) &= \frac{1}{\beta} \sum_{34} \Gamma(1', 3; 4, 2) \Gamma(4, 2'; 1, 3) G(3) G(4) \\
 &= \frac{1}{\beta} \sum_{34} \text{Diagram}, \tag{4.47}
 \end{aligned}$$

and inserting the vertex parametrization (4.30), we obtain

$$\begin{aligned}
 \frac{1}{\beta} \sum_{34} \text{Diagram} &= \\
 &= \frac{1}{\beta} \sum_{34} \sum_{\mu, \lambda=0}^3 \left(\text{Diagram}_\mu^\mu - \text{Diagram}_\mu^\mu \right) \\
 &\quad \times \left(\text{Diagram}_\lambda^\lambda - \text{Diagram}_\lambda^\lambda \right) G(\omega_3) G(\omega_4). \tag{4.48}
 \end{aligned}$$

As mentioned above, evaluating only \succ -components is sufficient, as all \succ -components can be generated by symmetry. The only contribution that is proportional to $\delta_{i_1' i_1} \delta_{i_2' i_2}$ and therefore a \succ -component is

$$\frac{1}{\beta} \sum_{34} \left| \text{Diagram} \right|_{\succ} = \frac{1}{\beta} \sum_{34} \sum_{\mu, \lambda=0}^3 \text{Diagram}_\mu^\mu \text{Diagram}_\lambda^\lambda \sigma_{\alpha_1 \alpha_4}^\mu \sigma_{\alpha_3 \alpha_2}^\mu \sigma_{\alpha_4 \alpha_1}^\lambda \sigma_{\alpha_2 \alpha_3}^\lambda. \tag{4.49}$$

The sum over spin indices α_3 and α_4 can now be evaluated. If at least one of $\mu, \lambda = 0$, the sum collapses to a single term. For example, $\mu = 0$ immediately gives

$$\sum_{\alpha_3 \alpha_4} \sigma_{\alpha_1 \alpha_4}^0 \sigma_{\alpha_3 \alpha_2}^0 \sigma_{\alpha_4 \alpha_1}^\lambda \sigma_{\alpha_2 \alpha_3}^\lambda = \sigma_{\alpha_1 \alpha_1}^\lambda \sigma_{\alpha_2 \alpha_2}^\lambda. \tag{4.50}$$

The case where $\mu \neq 0$ and $\lambda \neq 0$ is less trivial. This combination generates two distinct terms:

$$\sum_{\alpha_3, \alpha_4} \sigma_{\alpha_1 \alpha_4}^\mu \sigma_{\alpha_3 \alpha_2}^\mu \sigma_{\alpha_4 \alpha_1}^\lambda \sigma_{\alpha_2 \alpha_3}^\lambda = \left(\sum_{\alpha_3} \sigma_{\alpha_2 \alpha_3}^\lambda \sigma_{\alpha_3 \alpha_2}^\mu \right) \left(\sum_{\alpha_4} \sigma_{\alpha_1 \alpha_4}^\mu \sigma_{\alpha_4 \alpha_1}^\lambda \right) =$$

4. Implementation

$$\begin{aligned}
&= \left(\delta^{\lambda\mu} \sigma_{\alpha_2\alpha_2}^0 + i \sum_{\kappa=1}^3 \varepsilon^{\lambda\mu\kappa} \sigma_{\alpha_2\alpha_2}^\kappa \right) \left(\delta^{\mu\lambda} \sigma_{\alpha_1\alpha_1}^0 + i \sum_{\eta=1}^3 \varepsilon^{\mu\lambda\eta} \sigma_{\alpha_1\alpha_1}^\eta \right) = \\
&= \delta^{\mu\lambda} \sigma_{\alpha_2\alpha_2}^0 \sigma_{\alpha_1\alpha_1}^0 + \sum_{\kappa=1}^3 \left| \varepsilon^{\lambda\mu\kappa} \right| \sigma_{\alpha_2\alpha_2}^\kappa \sigma_{\alpha_1\alpha_1}^\kappa, \quad (4.51)
\end{aligned}$$

where the Levi-Civita symbol $\varepsilon^{\lambda\mu\kappa}$ in the last expression is 0 if any two of λ, μ, κ are equal. In other words, only combinations (λ, μ, κ) that are permutations of $(1, 2, 3)$ contribute. We define $\mathcal{P}(1, 2, 3)$ as the set of all such permutations. In total, the \simeq -component of the a -bubble is

$$\begin{aligned}
\frac{1}{\beta} \sum_{34} \left[\text{diagram} \right]_{\simeq} &= \frac{1}{\beta} \sum_{\omega_3\omega_4} \left\{ \sum_{\mu=0}^3 \left[\text{diagram} \right] \sigma_{\alpha_2\alpha_2}^0 \sigma_{\alpha_1\alpha_1}^0 \right. \\
&+ \sum_{\mu=1}^3 \left(\left[\text{diagram} \right] + \left[\text{diagram} \right] \right) \sigma_{\alpha_2\alpha_2}^\mu \sigma_{\alpha_1\alpha_1}^\mu \\
&\left. + \sum_{(\mu,\kappa,\lambda) \in \mathcal{P}(1,2,3)} \left[\text{diagram} \right] \sigma_{\alpha_2\alpha_2}^\mu \sigma_{\alpha_1\alpha_1}^\mu \right\} \quad (4.52)
\end{aligned}$$

for an XYZ model without off-diagonal interaction terms.

For later convenience, we introduce the abbreviation

$$\left[\Gamma \right]_{\text{sym}}(1', 2'; 1, 2) = \Gamma(1', 2'; 1, 2) + \Gamma(2', 1'; 2, 1) \quad (4.53)$$

to express sums that symmetrize vertex-like objects according to the crossing symmetry $\Gamma(1', 2'; 1, 2) = \Gamma(2', 1'; 2, 1)$. For example, in

$$\left[\text{diagram} \right]_{\text{sym}} = \text{diagram} + \text{diagram}, \quad (4.54)$$

the summands do not necessarily fulfill crossing symmetries, while the whole expression does.

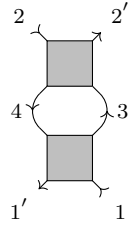
For an XXZ model, where $\Gamma^1 = \Gamma^2$, Eq. (4.52) can be simplified to

$$\begin{aligned}
\frac{1}{\beta} \sum_{34} \left[\text{diagram} \right]_{\simeq} &= \frac{1}{\beta} \sum_{\omega_3\omega_4} \left\{ \left(\left[\text{diagram} \right] + \left[\text{diagram} \right] \right) \sigma_{\alpha_2\alpha_2}^0 \sigma_{\alpha_1\alpha_1}^0 \right. \\
&+ 2 \left[\text{diagram} \right] \left(\sigma_{\alpha_2\alpha_2}^0 \sigma_{\alpha_1\alpha_1}^0 + \sigma_{\alpha_2\alpha_2}^3 \sigma_{\alpha_1\alpha_1}^3 \right) \\
&+ \sum_{\mu=1}^3 \left[\text{diagram} \right]_{\text{sym}} \sigma_{\alpha_2\alpha_2}^\mu \sigma_{\alpha_1\alpha_1}^\mu \\
&\left. + \left[\text{diagram} \right]_{\text{sym}} \left(\sigma_{\alpha_2\alpha_2}^1 \sigma_{\alpha_1\alpha_1}^1 + \sigma_{\alpha_2\alpha_2}^2 \sigma_{\alpha_1\alpha_1}^2 \right) \right\}. \quad (4.55)
\end{aligned}$$

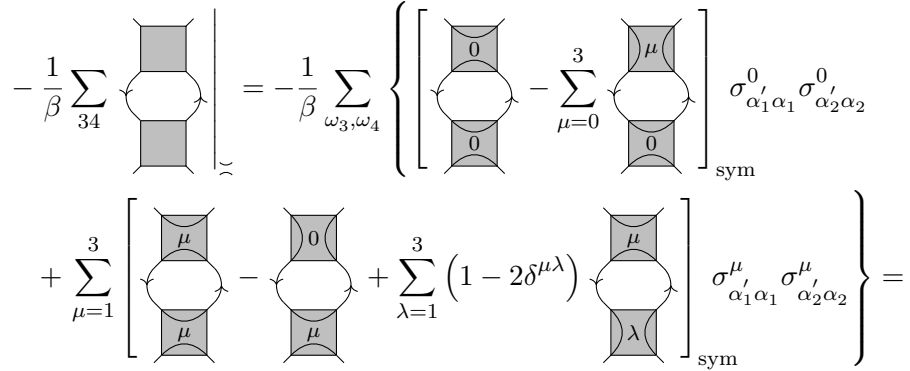
The parametrized form of bubbles in the other channels can be found analogously by inserting the parametrized vertex and evaluating the summations over spin indices. As this derivation is straightforward if a bit lengthy, we do not show it in detail for the other channels, where we only show the final result.

4.2.3 t -bubble

The fully parametrized t -bubble can be found analogously by inserting the parametrized vertex into the definition of the t -bubble. This definition contains a combinatorial minus sign consistent with the convention of Kugler and von Delft [54].

$$\begin{aligned}
 B_t(1', 2'; 1, 2) &= \\
 &= -\frac{1}{\beta} \sum_{34} \Gamma(1', 3; 1, 4) \Gamma(4, 2'; 3, 2) G(3) G(4) = -\frac{1}{\beta} \sum_{34} \text{Diagram} \cdot \quad (4.56)
 \end{aligned}$$


Inserting the fully parametrized vertex yields

$$\begin{aligned}
 -\frac{1}{\beta} \sum_{34} \text{Diagram} &= -\frac{1}{\beta} \sum_{\omega_3, \omega_4} \left\{ \left[\begin{array}{c} \text{Diagram with } 0 \\ \text{Diagram with } \mu \\ \text{Diagram with } 0 \end{array} \right]_{\text{sym}} \sigma_{\alpha'_1 \alpha_1}^0 \sigma_{\alpha'_2 \alpha_2}^0 \right. \\
 &+ \left. \sum_{\mu=1}^3 \left[\begin{array}{c} \text{Diagram with } \mu \\ \text{Diagram with } 0 \\ \text{Diagram with } \mu \\ \text{Diagram with } \lambda \end{array} \right]_{\text{sym}} \sigma_{\alpha'_1 \alpha_1}^\mu \sigma_{\alpha'_2 \alpha_2}^\mu \right\} =
 \end{aligned}$$


4. Implementation

$$\begin{aligned}
&= -\frac{1}{\beta} \sum_{\omega_3, \omega_4} \left\{ \left[\begin{array}{c} \text{Diagram 1} \\ \text{Diagram 2} \end{array} \right]_{\text{sym}} - \sum_{\mu=0}^3 \left[\begin{array}{c} \text{Diagram 3} \\ \text{Diagram 4} \end{array} \right]_{\text{sym}} \right\} \sigma_{\alpha'_1 \alpha_1}^0 \sigma_{\alpha'_2 \alpha_2}^0 \\
&+ \left[\begin{array}{c} \text{Diagram 5} \\ \text{Diagram 6} \\ \text{Diagram 7} \end{array} \right]_{\text{sym}} \left(\sigma_{\alpha'_1 \alpha_1}^1 \sigma_{\alpha'_2 \alpha_2}^1 + \sigma_{\alpha'_1 \alpha_1}^2 \sigma_{\alpha'_2 \alpha_2}^2 \right) \\
&+ \left[\begin{array}{c} \text{Diagram 8} \\ \text{Diagram 9} \\ \text{Diagram 10} \end{array} \right]_{\text{sym}} \left. \right\} \sigma_{\alpha'_1 \alpha_1}^3 \sigma_{\alpha'_2 \alpha_2}^3 \quad (4.57)
\end{aligned}$$

for the \simeq -components.

The diagrams in this expression have two different types of real-space structure, which is important in practice as it leads to large differences in numerical effort required for evaluation of these diagrams. Diagrams with one \simeq vertex and one \succ vertex, sometimes labeled ‘cup’ or ‘chalice’ diagrams, have two site arguments, of which only a few are independent after symmetry reduction. The numerical effort spent on evaluating these diagrams is therefore comparable to the diagrams in the a and p channel. The diagrams with two \simeq vertices, called ‘RPA-type diagrams’, have a closed internal loop, i.e. an additional, internal site parameter that is not constrained by external parameters. Therefore, all possibilities that are not related by symmetry must be evaluated and summed over. RPA-type diagrams are the only diagrams that require such an internal site summation, which makes them significantly more costly to evaluate than all other diagrams. For some systems, the runtime spent on evaluating these diagrams can be reduced by exploiting an internal convolution structure of the RPA-type diagrams. This approach is presented in Appendix C, though we did not implement it for the pyrochlore XXZ model, as it is inefficient for systems with a unit cell that contains more than one site.

4.2.4 p -bubble

Again proceeding analogously as in the other channels, we start from the definition of the p -bubble, which contains a combinatorial factor $\frac{1}{2}$ consistent

with the convention of Kugler and von Delft [54]:

$$\begin{aligned}
 B_p(1', 2'; 1, 2) &= \frac{1}{2\beta} \sum_{34} \Gamma(1', 2'; 4, 3) \Gamma(4, 3; 1, 2) G(3) G(4) \\
 &= \frac{1}{2\beta} \sum_{34} \text{Diagram} . \tag{4.58}
 \end{aligned}$$

After some algebra, we obtain

$$\begin{aligned}
 \frac{1}{2\beta} \sum_{34} \text{Diagram} &= \\
 &= \frac{1}{2\beta} \sum_{\omega_3, \omega_4} \left\{ \sum_{\mu=0}^3 \left(\text{Diagram}_\mu + \text{Diagram}_\mu \right) \sigma_{\alpha'_1 \alpha_1}^0 \sigma_{\alpha'_2 \alpha_2}^0 \right. \\
 &\quad \left. + \sum_{\mu=1}^3 \left[\text{Diagram}_\mu + \text{Diagram}_\mu \right]_{\text{sym}} \sigma_{\alpha'_1 \alpha_1}^\mu \sigma_{\alpha'_2 \alpha_2}^\mu \right. \\
 &\quad \left. + \sum_{(\mu, \kappa, \lambda) \in \mathcal{P}\{1, 2, 3\}} \left(\text{Diagram}_{\kappa\lambda} + \text{Diagram}_{\kappa\lambda} \right) \sigma_{\alpha'_1 \alpha_1}^\mu \sigma_{\alpha'_2 \alpha_2}^\mu \right\} . \tag{4.59}
 \end{aligned}$$

This can be simplified using symmetries known from the vertex parametrization (see Eq. (4.30)). Because the vertex is antisymmetric under exchange of two legs, the \succ -component and \prec -component satisfy

$$\Gamma_{i_1 i_2}^{\succ \mu}(\omega'_1, \omega'_2; \omega_1, \omega_2) = \Gamma_{i_1 i_2}^{\prec \mu}(\omega'_1, \omega'_2; \omega_2, \omega_1) . \tag{4.60}$$

Therefore, the contributions with two \succ -components are equal to those with two \prec -components:

$$\frac{1}{2\beta} \sum_{34} \text{Diagram}_{\mu\lambda} = \frac{1}{2\beta} \sum_{34} \text{Diagram}_{\mu\lambda} . \tag{4.61}$$

4. Implementation

Inserting this relation as well as $\Gamma^1 = \Gamma^2$, we obtain

$$\begin{aligned}
 \frac{1}{2\beta} \sum_{34} \left[\text{Diagram} \right] &= \frac{1}{\beta} \sum_{\omega_3, \omega_4} \left\{ \sum_{\mu=0}^3 \left[\text{Diagram} \right] \sigma_{\alpha'_1 \alpha_1}^0 \sigma_{\alpha'_2 \alpha_2}^0 \right. \\
 &+ \sum_{\mu=1}^3 \left[\text{Diagram} \right]_{\text{sym}} \sigma_{\alpha'_1 \alpha_1}^\mu \sigma_{\alpha'_2 \alpha_2}^\mu + 2 \left[\text{Diagram} \right] \sigma_{\alpha'_1 \alpha_1}^3 \sigma_{\alpha'_2 \alpha_2}^3 \\
 &\left. + \left[\text{Diagram} \right]_{\text{sym}} \left(\sigma_{\alpha'_1 \alpha_1}^1 \sigma_{\alpha'_2 \alpha_2}^1 + \sigma_{\alpha'_1 \alpha_1}^2 \sigma_{\alpha'_2 \alpha_2}^2 \right) \right\}. \quad (4.62)
 \end{aligned}$$

4.2.5 Symmetries preserved by the flow

There are several symmetries of the vertex that, if present in the bare vertex Γ^0 , remain unchanged over the entire flow. This enables us to conclude by induction that the full vertex has these properties at all points in the flow. As the reducible parts of the vertex are obtained by evaluating a subset of the same bubble diagrams, these properties are preserved for each individual reducible part as well, which can be checked explicitly by inspecting the bubble equations in the preceding sections. In the following, these symmetries will be explained for the full vertex Γ , but apply to reducible parts γ_a , γ_p and γ_t as well [48, 75].

Firstly, the bubble equations do not generate imaginary parts for real vertices. If the interaction $J^{\mu\lambda}$ in the Hamiltonian is real, it follows by induction that the vertex is real as well, i.e.

$$\text{Im } \Gamma = 0. \quad (4.63)$$

Furthermore, we are now able to check our previous statement that the flow does not generate off-diagonal terms if the interaction is diagonal in $\mu\lambda$ by simply examining the explicit form of the bubble functions. Since there is never an off-diagonal combination of Pauli matrices such as $\sigma^\mu \sigma^\lambda$ where $\lambda \neq \mu$,

$$\Gamma^{\mu\lambda} = \delta^{\mu\lambda} \Gamma^\mu \quad (4.64)$$

throughout the flow. If some of the components of the interaction are equal, the same components are equal in the full vertex as well. For example, in the XXZ model, $J^1 = J^2$ and the same is true for the vertex: $\Gamma^1 = \Gamma^2$.

4.3 Spin susceptibility

The spin susceptibility is the primary quantity we use to characterize the states obtained by the fRG flow. It is defined as [48, 66]

$$\chi_{ij}^{\mu\lambda}(\Omega) = \int_0^\beta d\tau e^{i\Omega\tau} \langle \mathcal{T}_\tau S_i^\mu(\tau) S_j^\lambda(0) \rangle, \quad (4.65)$$

where $\mu, \lambda \in \{x, y, z\} \cong \{1, 2, 3\}$. Both the susceptibility in the global basis $\tilde{\chi}$ as well as the neutron scattering structure factor \mathcal{S} can be derived from χ using the equations in Sec. 2.4. As the parametrized expression for the susceptibility contains some diagrams which are not part of the building blocks defined in the previous sections, it will be derived separately in the following, starting from the general pffRG expression for an XYZ model.

4.3.1 Evaluation of the spin susceptibility in pffRG

In pseudofermion terms, the expectation value in the definition of the susceptibility (4.65) is a two-particle correlation function. It can be calculated from Green's functions and the two-particle vertex as follows:

$$\begin{aligned} \chi_{ij}^{\mu\mu}(\Omega) &= \\ &= \int_0^\beta d\tau e^{i\Omega\tau} \sum_{\alpha_1\alpha'_1\alpha_2\alpha'_2} \frac{1}{4} \sigma_{\alpha_1\alpha'_1}^\mu \sigma_{\alpha_2\alpha'_2}^\mu \langle \mathcal{T}_\tau \bar{\psi}_{i\alpha_1}(\tau) \psi_{i\alpha'_1}(\tau) \bar{\psi}_{j\alpha_2}(0) \psi_{j\alpha'_2}(0) \rangle = \\ &= \frac{1}{4\beta^2} \int_0^\beta d\tau \sum_{\omega_1\omega'_1\omega_2\omega'_2} \delta(\omega_1 + \omega_2 - \omega'_1 - \omega'_2) e^{i(\Omega + \omega_1 - \omega'_1)\tau} \\ &\quad \times \sum_{\alpha_1\alpha'_1\alpha_2\alpha'_2} \sigma_{\alpha_1\alpha'_1}^\mu \sigma_{\alpha_2\alpha'_2}^\mu \langle \bar{\psi}_{i\alpha_1}(\omega_1) \psi_{i\alpha'_1}(\omega'_1) \bar{\psi}_{j\alpha_2}(\omega_2) \psi_{j\alpha'_2}(\omega'_2) \rangle = \\ &= \frac{1}{4\beta^2} \sum_{\omega_1\omega_2} \sum_{\alpha_1\alpha'_1\alpha_2\alpha'_2} \sigma_{\alpha_1\alpha'_1}^\mu \sigma_{\alpha_2\alpha'_2}^\mu \\ &\quad \times \langle \bar{\psi}_{i\alpha_1}(\omega_1) \psi_{i\alpha'_1}(\omega_1 + \Omega) \bar{\psi}_{j\alpha_2}(\omega_2) \psi_{j\alpha'_2}(\omega_2 - \Omega) \rangle = \\ &= -\frac{1}{4\beta} \sum_{\omega_1} \sum_{\alpha_1\alpha_2} \overbrace{\sigma_{\alpha_1\alpha_2}^\mu \sigma_{\alpha_2\alpha_1}^\mu}^2 \delta_{ij} G(\omega_1) G(\omega_1 + \Omega) \\ &\quad - \frac{1}{4\beta^2} \sum_{\omega_1\omega_2} \sum_{\alpha_1\alpha'_1\alpha_2\alpha'_2} \sigma_{\alpha_1\alpha'_1}^\mu \sigma_{\alpha_2\alpha'_2}^\mu G(\omega_1) G(\omega_1 + \Omega) G(\omega_2) G(\omega_2 - \Omega) \\ &\quad \times \Gamma(i, \omega_1 + \Omega, \alpha'_1, j, \omega_2 - \Omega, \alpha'_2; j, \omega_2, \alpha_2, i, \omega_1, \alpha_1). \end{aligned} \quad (4.66)$$

In the last step, the other possible pairing of $\bar{\psi}\psi\bar{\psi}\psi$ that gives a non-interacting propagator bubble does not contribute: It is $\sim \delta(\Omega) (\sum_\omega G(\omega))^2$, which is zero

4. Implementation

due to antisymmetry of the propagators. Shifting the frequencies by $\Omega/2$ for convenience and inserting the vertex parametrization of Eq. (4.30), we get

$$\begin{aligned}
\chi_{ij}^{\mu\mu}(\Omega) &= -\frac{1}{2\beta} \delta_{ij} \sum_{\nu} G(\nu - \frac{\Omega}{2}) G(\nu + \frac{\Omega}{2}) \\
&\quad - \frac{1}{4\beta^2} \sum_{\nu\nu'} \sum_{\alpha_1\alpha_1'\alpha_2\alpha_2'} \sigma_{\alpha_1\alpha_1'}^{\mu} \sigma_{\alpha_2\alpha_2'}^{\mu} G(\nu - \frac{\Omega}{2}) G(\nu + \frac{\Omega}{2}) G(\nu' + \frac{\Omega}{2}) G(\nu' - \frac{\Omega}{2}) \\
&\quad \times \sum_{\lambda=0}^3 \left[\begin{array}{cc} \begin{array}{c} \nu - \frac{\Omega}{2} \quad \nu' - \frac{\Omega}{2} \\ \diagdown \quad \diagup \\ \lambda \\ \diagup \quad \diagdown \\ \nu + \frac{\Omega}{2} \quad \nu' + \frac{\Omega}{2} \end{array} & \sigma_{\alpha_1\alpha_2}^{\lambda} \sigma_{\alpha_2\alpha_1}^{\lambda} - \delta_{ij} \\ & \begin{array}{c} \nu - \frac{\Omega}{2} \quad \nu' - \frac{\Omega}{2} \\ \diagdown \quad \diagup \\ \lambda \\ \diagup \quad \diagdown \\ \nu + \frac{\Omega}{2} \quad \nu' + \frac{\Omega}{2} \end{array} & \sigma_{\alpha_1\alpha_1}^{\lambda} \sigma_{\alpha_2\alpha_2}^{\lambda} \end{array} \right]. \quad (4.67)
\end{aligned}$$

These combinations of Pauli matrices evaluate to

$$\sum_{\alpha_1\alpha_1'\alpha_2\alpha_2'} \sigma_{\alpha_1\alpha_1'}^{\mu} \sigma_{\alpha_2\alpha_2'}^{\mu} \sigma_{\alpha_1\alpha_2}^{\lambda} \sigma_{\alpha_2\alpha_1}^{\lambda} = \text{Tr}(\sigma^{\mu} \sigma^{\lambda} \sigma^{\mu} \sigma^{\lambda}) = \begin{cases} 2, & \lambda = 0 \\ 4\delta^{\mu\lambda} - 2, & \lambda \neq 0 \end{cases} \quad (4.68)$$

and

$$\sum_{\alpha_1\alpha_1'\alpha_2\alpha_2'} \sigma_{\alpha_1\alpha_1'}^{\mu} \sigma_{\alpha_2\alpha_2'}^{\mu} \sigma_{\alpha_1\alpha_1}^{\lambda} \sigma_{\alpha_2\alpha_2}^{\lambda} = [\text{Tr}(\sigma^{\mu} \sigma^{\lambda})]^2 = \begin{cases} 0, & \lambda = 0 \\ 4\delta^{\mu\lambda}, & \lambda \neq 0. \end{cases} \quad (4.69)$$

Thus,

$$\begin{aligned}
\chi_{ij}^{\mu\mu}(\Omega) &= -\frac{1}{2\beta} \delta_{ij} \sum_{\nu} G(\nu - \frac{\Omega}{2}) G(\nu + \frac{\Omega}{2}) \\
&\quad - \frac{1}{4\beta^2} \sum_{\nu\nu'} G(\nu - \frac{\Omega}{2}) G(\nu + \frac{\Omega}{2}) G(\nu' + \frac{\Omega}{2}) G(\nu' - \frac{\Omega}{2}) \\
&\quad \times 2 \left[\begin{array}{c} \delta_{ij} \begin{array}{c} \nu - \frac{\Omega}{2} \quad \nu' - \frac{\Omega}{2} \\ \diagdown \quad \diagup \\ 0 \\ \diagup \quad \diagdown \\ \nu + \frac{\Omega}{2} \quad \nu' + \frac{\Omega}{2} \end{array} + \delta_{ij} \sum_{\lambda=1}^3 (2\delta^{\mu\lambda} - 1) \begin{array}{c} \nu - \frac{\Omega}{2} \quad \nu' - \frac{\Omega}{2} \\ \diagdown \quad \diagup \\ \lambda \\ \diagup \quad \diagdown \\ \nu + \frac{\Omega}{2} \quad \nu' + \frac{\Omega}{2} \end{array} - 2 \begin{array}{c} \nu - \frac{\Omega}{2} \quad \nu' - \frac{\Omega}{2} \\ \diagdown \quad \diagup \\ \mu \\ \diagup \quad \diagdown \\ \nu + \frac{\Omega}{2} \quad \nu' + \frac{\Omega}{2} \end{array} \right] =
\end{aligned}$$

$$\begin{aligned}
 &= -\frac{1}{2\beta} \delta_{ij} \sum_{\nu} G(\nu - \frac{\Omega}{2}) G(\nu + \frac{\Omega}{2}) \\
 &\quad - \frac{1}{2\beta^2} \sum_{\nu\nu'} G(\nu - \frac{\Omega}{2}) G(\nu + \frac{\Omega}{2}) G(\nu' + \frac{\Omega}{2}) G(\nu' - \frac{\Omega}{2}) \\
 &\quad \times \left[\delta_{ij} \Gamma_{ii}^{\tilde{0}}(\nu + \frac{\Omega}{2}, \nu' - \frac{\Omega}{2}; \nu' + \frac{\Omega}{2}, \nu - \frac{\Omega}{2}) \right. \\
 &\quad \quad + \delta_{ij} \sum_{\lambda=1}^3 \left(2\delta^{\mu\lambda} - 1 \right) \Gamma_{ii}^{\tilde{\lambda}}(\nu + \frac{\Omega}{2}, \nu' - \frac{\Omega}{2}; \nu' + \frac{\Omega}{2}, \nu - \frac{\Omega}{2}) \\
 &\quad \quad \left. - 2\Gamma_{ij}^{\lambda(\mu)}(\nu + \frac{\Omega}{2}, \nu' - \frac{\Omega}{2}; \nu' + \frac{\Omega}{2}, \nu - \frac{\Omega}{2}) \right]. \quad (4.70)
 \end{aligned}$$

In the XXZ model, the sum in the second-to-last line of (4.70) collapses to

$$\delta_{ij} \sum_{\lambda=1}^3 \left(2\delta^{\mu\lambda} - 1 \right) \Gamma_{ii}^{\tilde{\lambda}} = \delta_{ij} \times \begin{cases} \left(-\Gamma_{ii}^{\tilde{3}} \right), & \mu = 1, 2 \\ \left(-2\Gamma_{ii}^{\tilde{1}} + \Gamma_{ii}^{\tilde{3}} \right), & \mu = 3. \end{cases} \quad (4.71)$$

The susceptibility in the Heisenberg model can be obtained from this by setting $\Gamma^1 = \Gamma^2 = \Gamma^3$. The expression for $\chi_{ij}^z(\Omega)$ thus obtained is consistent with the one in Refs. [51, 75].

The static susceptibility is obtained by direct evaluation of Eq. (4.70) at $\Omega = 0$. In contrast, obtaining the zero-time susceptibility by integrating over Ω in Eq. (4.70) is not straightforward. The numerical quadrature that has to be evaluated suffers from numerical inaccuracy due to partial cancellation of components. In the next subsection, we discuss a more efficient way to compute this quantity.

4.3.2 Efficient evaluation of the zero-time susceptibility

The numerical problems one encounters when trying to evaluate the zero-time susceptibility directly from Eq. (4.70) can be solved using the vertices' asymptotic behavior described in Sec. 4.1.6. As all vertices on the right-hand side of Eq. (4.70) are integrated over all frequency arguments, the integration variables ν , ν' and Ω can be freely transformed within the three-dimensional space on which the vertices are defined. Thus, each reducible vertex γ_r can be integrated separately using the natural frequency arguments of channel r (see Tab. 4.1). This is advantageous, as parametrization of the reducible vertices using asymptotic classes K_1, K_2, K_2' and K_3 can now be exploited as follows:

$$\sum_{\Omega_r, \nu_r, \nu_r'} G(\nu_r - \frac{\Omega_r}{2}) G(\nu_r + \frac{\Omega_r}{2}) G(\nu_r' + \frac{\Omega_r}{2}) G(\nu_r' - \frac{\Omega_r}{2}) \gamma_{r;ij}^{\mu; \Omega_r, \nu_r, \nu_r'} =$$

4. Implementation

$$\begin{aligned}
&= \beta^2 \sum_{\Omega_r} (\Pi(\Omega_r))^2 K_{1r;ij}^{\mu;\Omega_r} + \beta \sum_{\Omega_r \nu_r} G(\nu_r - \frac{\Omega_r}{2}) G(\nu_r + \frac{\Omega_r}{2}) \Pi(\Omega_r) K_{2r;ij}^{\mu;\Omega_r, \nu_r} \\
&\quad + \beta \sum_{\Omega_r \nu'_r} \Pi(\Omega_r) G(\nu'_r - \frac{\Omega_r}{2}) G(\nu'_r + \frac{\Omega_r}{2}) K_{2'r;ij}^{\mu;\Omega_r, \nu'_r} \\
&\quad + \sum_{\Omega_r \nu_r \nu'_r} G(\nu_r - \frac{\Omega_r}{2}) G(\nu_r + \frac{\Omega_r}{2}) G(\nu'_r + \frac{\Omega_r}{2}) G(\nu'_r - \frac{\Omega_r}{2}) K_{3r;ij}^{\mu;\Omega_r, \nu_r, \nu'_r},
\end{aligned} \tag{4.72}$$

where $\Pi(\Omega) = \frac{1}{\beta} \sum_{\nu} G(\nu - \frac{\Omega}{2}) G(\nu + \frac{\Omega}{2})$. The integration within $\Pi(\Omega)$ can be performed in advance, reducing overall numerical effort. The contribution of $\Gamma_{ii}^{\sim 0}$ is zero because $\gamma_{a;ii}^{0;\Omega, \nu, \nu'} = -\gamma_{p;ii}^{0;-\Omega, \nu, \nu'}$ and $\gamma_{t;ii}^{0;\Omega, \nu, \nu'} = -\gamma_{t;ii}^{0;\Omega, -\nu, \nu'}$. Furthermore, the non-interacting contribution to the zero-time susceptibility (first term in Eq. (4.70)) can be evaluated analytically [51]:

$$\begin{aligned}
&-\frac{1}{2\beta^2} \delta_{ij} \sum_{\Omega \nu} G(\nu - \frac{\Omega}{2}) G(\nu + \frac{\Omega}{2}) = -\frac{1}{2} \delta_{ij} \lim_{\delta\tau \rightarrow 0} G(+\delta\tau) G(-\delta\tau) = \\
&\quad = \frac{1}{2} \delta_{ij} \lim_{\delta\tau \rightarrow 0} \langle \bar{\psi}_{i\alpha}(\delta\tau) \psi_{i\alpha}(0) \rangle \langle \psi_{i\beta}(0) \bar{\psi}_{i\beta}(\delta\tau) \rangle = \frac{1}{8} \delta_{ij}, \tag{4.73}
\end{aligned}$$

where the indices α, β in the last line take an arbitrary single value and are not summed over. The last line shows that $\chi_{ii}^z|_{\tau=0}$ is identical to the non-interacting contribution to $\langle S_i^z S_i^z \rangle$, consistent with Ref. [51]. Thus, violation of the pseudofermion constraint can be detected efficiently using the zero-time susceptibility.

Now, each term in Eq. (4.70) can be decomposed by channel and asymptotic class, leading to a somewhat lengthy expression. Since each integration in the fully decomposed expression has much less structure to contend with compared to an integration over the full vertex, it is now possible to perform each integral with sufficient numerical accuracy.

When evaluated at equal sites, horizontal Γ_{ii}^{\sim} and vertical Γ_{ii}^{\langle} contribution to the zero-time susceptibility in Eq. (4.70) are equal, because they can be transformed into each other using crossing symmetry and substitution of integration variables as

$$\begin{aligned}
&\frac{1}{2\beta^2} \sum_{\Omega \nu \nu'} GGGG \Gamma_{ii}^{\sim \mu}(\nu + \frac{\Omega}{2}, \nu' - \frac{\Omega}{2}; \nu' + \frac{\Omega}{2}, \nu - \frac{\Omega}{2}) = \\
&\quad = \frac{1}{2\beta^2} \sum_{\Omega \nu \nu'} GGGG \Gamma_{ii}^{\langle \mu}(\nu' - \frac{\Omega}{2}, \nu + \frac{\Omega}{2}; \nu' + \frac{\Omega}{2}, \nu - \frac{\Omega}{2}) = \\
&\quad = \frac{1}{2\beta^2} \sum_{\Omega \nu \nu'} GGGG \Gamma_{ii}^{\langle \mu}(\nu + \frac{\Omega}{2}, \nu' - \frac{\Omega}{2}; \nu' + \frac{\Omega}{2}, \nu - \frac{\Omega}{2}). \tag{4.74}
\end{aligned}$$

Thus, only contributions of Γ^{\langle} have to be evaluated explicitly. The value of $\chi_{ii}^{\mu\mu}|_{\tau=0}$ can be obtained by inserting the above relation into Eq. (4.70), which

yields

$$\begin{aligned}
 \chi_{ii}^{\mu\mu}|_{\tau=0} &= \\
 &= \frac{1}{8} - \frac{1}{2\beta^2} \sum_{\Omega\nu\nu'} GGGG \left[\sum_{\lambda=1}^3 (2\delta^{\mu\lambda} - 1) \Gamma_{ii}^{(\lambda)}(\nu + \frac{\Omega}{2}, \nu' - \frac{\Omega}{2}; \nu' + \frac{\Omega}{2}, \nu - \frac{\Omega}{2}) \right. \\
 &\quad \left. - 2 \Gamma_{ii}^{(\mu)}(\nu + \frac{\Omega}{2}, \nu' - \frac{\Omega}{2}; \nu' + \frac{\Omega}{2}, \nu - \frac{\Omega}{2}) \right] = \\
 &= \frac{1}{8} + \frac{1}{2\beta^2} \sum_{\Omega\nu\nu'} GGGG \sum_{\lambda=1}^3 \Gamma_{ii}^{(\lambda)}(\nu + \frac{\Omega}{2}, \nu' - \frac{\Omega}{2}; \nu' + \frac{\Omega}{2}, \nu - \frac{\Omega}{2}). \quad (4.75)
 \end{aligned}$$

This expression is independent of μ and thus guarantees the equality $\langle S_i^x S_i^x \rangle = \langle S_i^y S_i^y \rangle = \langle S_i^z S_i^z \rangle$ by construction.

Results

In this chapter, we present results obtained from the multiloop pffRG flows. To establish whether our approach is suitable for all parts of the phase diagram, we performed one calculation in each phase predicted in prior work by Benton et al. [28] (see Fig 5.1). The symbols \diamond , \square , \circ , \triangle , and \diamond used in the following refer to Fig. 5.1. We expect to find two ordered phases, the all-in-all-out phase (AIAO) at $\theta = 180^\circ$ (\diamond) and an easy-plane antiferromagnet (AF_\perp) at $\theta = -90^\circ$ (\square). The quantum spin ice phases QSI_0 and QSI_π should be present at $\theta = -1^\circ$ (\circ) and 20° (\triangle), respectively. At $\theta = 90^\circ$ (\triangle), prior work found a quantum spin nematic phase [28, 43]. Results for physical observables will follow after a discussion of loop convergence and the pseudofermion constraint, which may be seen as an indicator for the degree of reliability of our results in different domains.

All results, at all points θ in the phase diagram and for all loop orders ℓ , were obtained from mFRG flows on a spherical correlation graph with radius

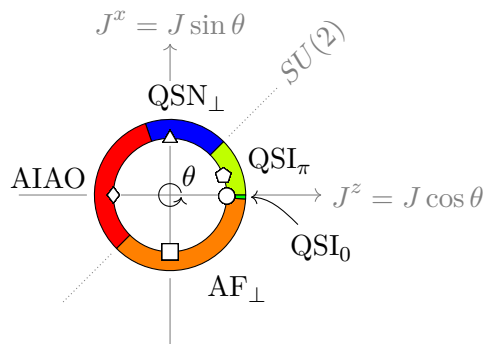


Figure 5.1: Zero-temperature phase diagram of the pyrochlore XXZ model found in cluster-variational calculations. Symbols mark the values of θ where we performed multiloop pffRG calculations, namely at $\theta = 180^\circ$ (\diamond), at $\theta = -90^\circ$ (\square), at $\theta = -1^\circ$ (\circ), at $\theta = 20^\circ$ (\triangle), and at $\theta = 90^\circ$ (\triangle). Adapted with permission from Benton et al. [28, Fig. 1(a)].

Quantity	Symbol	Value
cutoff radius for correlations	r_{\max}/a	6
\Rightarrow number of real-space vertex components i'	BN	651
\Rightarrow number of independent components		68
initial IR cutoff	Λ_i/J	8.0
\Rightarrow initial integration parameter	$t(\Lambda_i)$	-2.08
minimal step size in t	δt_{\min}	0.01
maximal step size in t	δt_{\max}	0.5
mixing factor for initial parquet iteration	z	0.5
maximum number of iterations	M_{\max}	200

Table 5.1: Choice of numerical parameters used to obtain the results presented in this chapter.

$r_{\max} = 6a$ that contains 651 sites, initialized with self-consistent parquet states at¹ $\Lambda_i/J = 8.0$. A detailed list of numerical parameters is shown in Tab. 5.1; the representation of the structure of vertex components in frequency space is more complicated and discussed in Appendix B.

5.1 Loop convergence

With growing loop order $\ell \rightarrow \infty$, the multiloop fRG solutions are expected to converge to the parquet solution of the regulated system [55]. All features of parquet solutions, such as fulfillment of the Mermin-Wagner theorem, therefore apply to converged mFRG solutions as well. In this sense, loop convergence is a central feature of the mFRG approach, and statements about physical observables should be obtained from a loop-converged solution at small Λ/J .

However, loop convergence is not guaranteed, as it requires the contribution of diagrams to decrease quickly with their loop order. This is a highly non-trivial property of the system and may depend on system-specific parameters such as interaction strength [55]. Thus, eventual convergence of the solution in loop order is an assumption that has to be tested for each application of multiloop fRG. In prior work, this has been done already for the X-ray edge singularity [55] and the Hubbard model [56].

¹This value of Λ_i is larger than the one used in kagome Heisenberg calculations [51]. Although the initial parquet iteration converges at $\Lambda_i/J \approx 5$, further increase of Λ_i leads to quicker convergence at the cost of more runtime used for integration of the mFRG flow. As we found that the parquet iteration generally needed a larger fraction of the total runtime for the pyrochlore XXZ model than for the kagome Heisenberg model, we increased Λ_i to decrease the total runtime. Provided that the parquet iteration converges, this choice has no effect on loop-converged results, which satisfy the parquet relations (see Sec. 3.3 and Refs. [51, 55]).

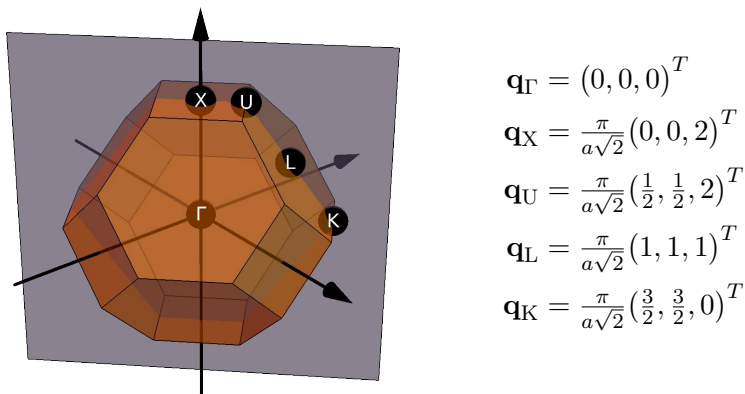


Figure 5.2: Extended Brillouin Zone of the pyrochlore lattice (orange) and plane that will be used for contour plots of the susceptibility (gray) relative to the reciprocal cubic coordinate axes (black). High-symmetry points Γ , X , U , L and K are labeled for later use. Their coordinates are shown on the right, where a is the distance between nearest neighbors.

In this respect, reaching loop convergence in multiloop pffRG seems particularly difficult: Due to the lack of a kinetic term in the pseudofermion Hamiltonian, pffRG is inherently in the strong-coupling limit. Consistent with our results for the kagome Heisenberg model [51], we find that spin susceptibilities for the XXZ model in disordered phases² (see Fig. 5.3) do not change significantly for loop orders $\ell > 2$ down to $\Lambda/J \approx 0.25$. At smaller Λ , deviations between loop orders become visible. This dependence on the ratio Λ/J is not surprising, since the IR cutoff Λ is the only bare energy scale that regularizes interactions in the absence of a kinetic term. Between $\Lambda/J = 0.2$ and 0.1 , numerical artifacts caused by insufficient resolution of the K_{3t}^0 vertex component become visible. These are discussed further below.

In the vertex and self-energy, convergence is more difficult to reach than in the susceptibility. Fig. 5.4 shows the evolution of the self-energy Σ and the vertex reducible in the t -channel $\gamma_{t;\langle ij \rangle}^{\mu;\Omega,\nu,\nu'}$ for two nearest-neighbor sites i and j at $\theta = 20^\circ$ (\diamond in Fig. 5.1). For all vertex components $\mu \neq 0$, a cut along the bosonic Ω axis and a cut along the fermionic diagonal $\nu = \nu'$ is shown. For $\mu = 0$, the plot along the bosonic axis is omitted as $\gamma_{t;ij}^{0;\Omega,\nu,\nu'} = 0$ for $\nu = \nu' = 0$. Already at $\Lambda/J = 3.0$, where the susceptibilities are almost identical across all loop orders, differences between $\ell = 1$ and higher loop orders become visible. The deviations between loop orders increase slowly as Λ is lowered, until at $\Lambda/J = 0.1$, the $\ell = 2$ and $\ell = 3$ curves do not seem converged any more.

²Correlations diverge in ordered phases, and reaching loop convergence in such phases is rather challenging, though it has been demonstrated by Kiese et al. [57] for the cubic and fcc lattice. Since the present analysis focuses on disorder due to frustration, the specific manner of divergence is not of particular interest and we did not attempt to reach loop convergence for choices of θ where we found ordered states in an $\ell = 1$ calculation.

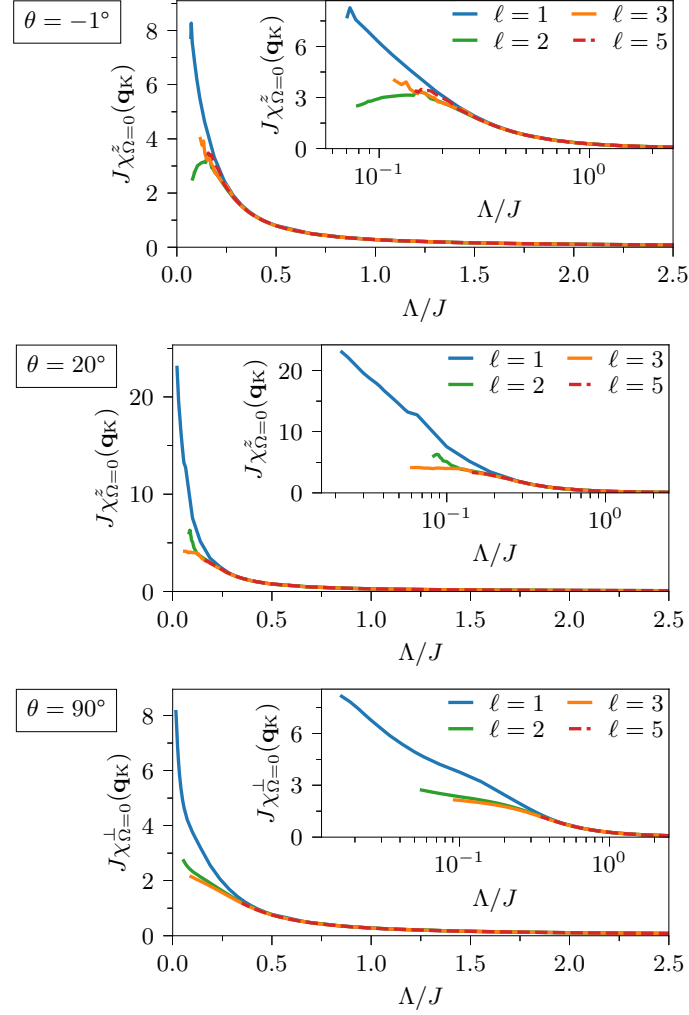


Figure 5.3: Loop convergence in the susceptibility flow in the disordered phases at $\theta = -1^\circ$, 20° and 90° (\circ , \diamond and \triangle in Fig. 5.1). Shown are components of the static susceptibility $\chi_{\Omega=0}^{\mu\mu}(\mathbf{q}_K)$ as a function of Λ at \mathbf{q}_K in reciprocal space (see Fig. 5.2). In each phase, the component μ has been chosen to correspond to the dominant component, where $\chi^z \equiv \chi^{zz}$ and $\chi^\perp \equiv \chi^{xx}$. In all phases, the susceptibility flow converges with loop order ℓ , though numerical artifacts make data for $\theta = -1^\circ$ and 20° unreliable below $\Lambda/J \approx 0.1$.

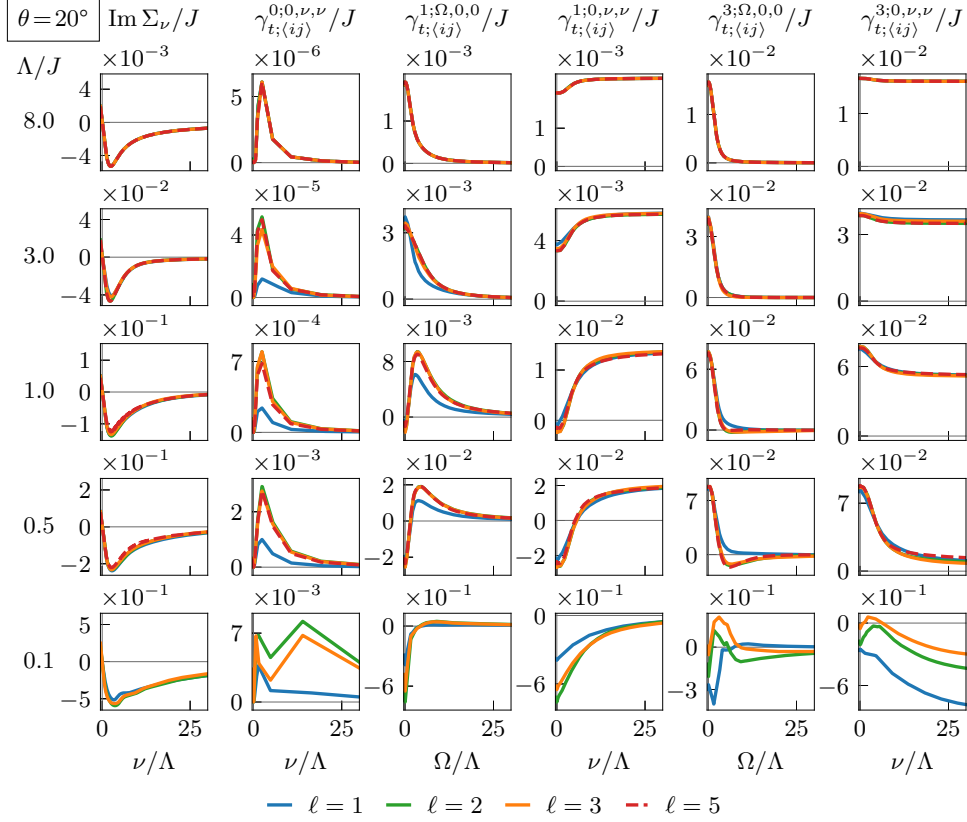


Figure 5.4: Loop convergence in the pseudofermion self-energy and four-point vertex at $\theta = 20^\circ$ (\diamond in Fig. 5.1). Each column corresponds to a specific component, and each row corresponds to a specific value of Λ , decreasing from top to bottom. Colors signify loop order ℓ . First column: The pseudofermion self-energy Σ_ν as a function of fermionic frequency ν . Second to fourth column: Selected components of the t -reducible vertex $\gamma_{t;\langle ij \rangle}^{\mu;\Omega,\nu,\nu}$ are shown as a function of bosonic frequencies Ω and fermionic frequencies ν . As expected from observations for the Heisenberg J_1 - J_2 model on the kagome lattice [51], loop convergence in the self-energy and vertex requires higher loop order ℓ compared to convergence in the spin susceptibility. At $\Lambda/J = 0.1$, numerical artifacts are visible, which cause those present in the susceptibility flow (see Fig. 5.3). Data for $\ell = 5$ was not available at $\Lambda/J = 0.1$ due to insufficient computation time.

5. Results

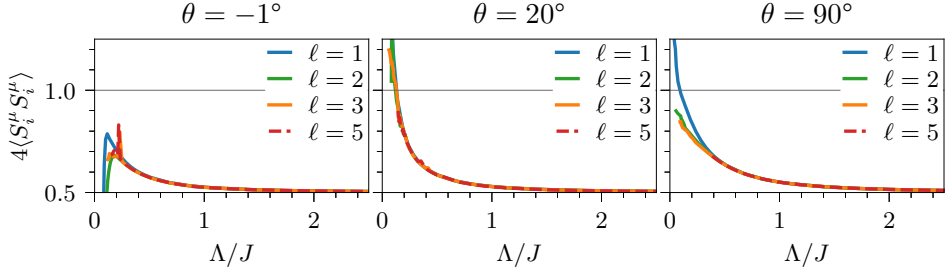


Figure 5.5: Equal-time same-site spin-spin correlator $\langle S_i^z S_i^z \rangle$, which is an indicator for the violation of the pseudofermion constraint (3.4), at $\theta = -1^\circ$, 20° and 90° (\circ , \diamond and \triangle in Fig. 5.1). The pseudofermion constraint is not inherently fulfilled by multiloop pffRG ground states, independent of loop order, though the violation is rather small for $\ell > 1$ at $\theta = 90^\circ$. At $\theta = -1^\circ$, the same numerical artifacts as in the susceptibility (see Fig. 5.3) and vertex (see Fig. 5.4) are visible around $\Lambda/J = 0.1$.

The numerical artifacts in the susceptibility at $\Lambda/J = 0.1$ have their origin in oscillations close to $\Omega = \nu = 0$ in vertex components which are likely caused by insufficient resolution of the structure of γ_t^0 . Already for the kagome Heisenberg model³ [51], we found that γ_t^0 was particularly difficult to evaluate and represent accurately because of two unique properties of this component: This component of the vertex is generally more than one order of magnitude smaller than all other components, leading to numerical problems due to evaluation of differences of similar large values. It is the only component of the vertex that is antisymmetric in its fermionic frequencies [51, 57]. Therefore, K_{1t}^0 and K_{2t}^0 are identically zero, and the entire component is represented by $\gamma_t^0 = K_{3t}^0$. As increased resolution in the K_3 class is expensive in both runtime and memory requirements, it is necessary to work with limited frequency resolution and adjust the frequency meshes used to represent vertices dynamically during the flow (see Appendix B). Finding an appropriate heuristic to ensure accurate representation of all vertex components is difficult, and our choice that worked well for the Heisenberg model (see Ref. [51]) appears unsuitable for pffRG flows in the XXZ model. Further work is required to design an algorithm that generates appropriate meshes for arbitrary models. Should this prove too difficult, at least a heuristic specifically tailored to the XXZ model is necessary to reach reliable conclusions for the zero-temperature behavior at small $\Lambda \ll J$.

5.2 Pseudofermion constraint

Pseudofermion fRG enforces the constraint that excludes unphysical states of the pseudofermion Hilbert space (Eq. (3.4)) only on average. Another assumption inherent in the multiloop pffRG approach is therefore either the convergence of solutions to exact fulfillment of the constraint, or the irrelevance of violation of this constraint for physical observables. As described in Sec. 3.1, deviations from the exact constraint for each site can be measured through evaluation of the equal-time same-site spin-spin correlator $\langle S_i^\mu S_i^\mu \rangle$. At large $\Lambda > J$, this correlator takes the free-fermion value $4\langle S_i^\mu S_i^\mu \rangle = \frac{1}{2}$, and with progressively smaller Λ/J , the correlator should approach the physical value of $4\langle S_i^\mu S_i^\mu \rangle = 1$ [51].

Our results for $4\langle S_i^\mu S_i^\mu \rangle$ (see Fig. 5.5) indicate that multiloop pffRG solutions generally do not satisfy the pseudofermion constraint, which is consistent with the behavior for the kagome Heisenberg model (see Ref. [51]). The behavior of the correlator is highly dependent on θ : At $\theta = -1^\circ$, the correlator $4\langle S_i^\mu S_i^\mu \rangle$ remains far from reaching the correct value 1. On the other hand, it reaches and exceeds 1 in all loop orders at $\theta = 20^\circ$. Perhaps closest to the satisfying the constraint are the multiloop $\ell > 1$ solutions at $\theta = 90^\circ$, where $4\langle S_i^\mu S_i^\mu \rangle$ approaches 1 at small $\Lambda < J$, reaching a value of 0.9 at $\Lambda/J \approx 0.05$. Our data demonstrates that pffRG does not inherently enforce the pseudofermion constraint, and that violation of the pseudofermion constraint is highly system-dependent. This dependence includes sensitivity to changes in the system's interaction parameters, which was not observed in the Heisenberg model [51].

Moreover, while the correlator is bounded by $4\langle S_i^\mu S_i^\mu \rangle \leq 1$ in the operator formalism (see Sec. 3.1), this bound is violated for flows at $\theta = 20^\circ$ and for $\ell = 1$ at $\theta = 90^\circ$. This is partially due to the sensitive dependence of the evaluation of the zero-time susceptibility on partial cancellation of contributions: In its frequency arguments, the vertex components have regions with differing sign in three-dimensional frequency space, which are integrated over. As already mentioned in Sec. 4.3.2, this makes accurate evaluation of the zero-time spin susceptibility rather challenging. The method presented there is able to mitigate problems with the numerical evaluation of these integrals; however, the accuracy of the value thus obtained is limited by the accuracy of the integrand. Thus, inaccuracies in the representation of the vertex are apparent in the zero-time susceptibility as well. Indeed, the numerical artifacts due to limited resolution of the vertex components in their frequency arguments are clearly visible at $\theta = -1^\circ$. Furthermore, inaccuracies are also caused by exclusion of diagrams due to finite loop order, the parquet approximation as well as finite maximal correlation length r_{\max} in real space. It may be

³In the Heisenberg model, the components $\gamma_r^1 = \gamma_r^2 = \gamma_r^3$ are equal because of the SU(2) symmetry of the Hamiltonian (see Sec. 4.1.2 and 4.1.4). Therefore, work on the Heisenberg model generally uses the labels ‘density part’ $\gamma_r^d = \gamma_r^0$ and ‘spin part’ $\gamma_r^s = \gamma_r^1 = \gamma_r^2 = \gamma_r^3$.

worthwhile to investigate the effect of a finer frequency mesh and increased real-space cutoff radius r_{\max} on $\langle S_i^\mu S_j^\mu \rangle$ systematically, though this is outside the scope of this thesis due to the required numerical resources. Nevertheless, work on the kagome Heisenberg model indicates that the spin susceptibilities are barely affected by violation of the pseudofermion constraint [51].

5.3 Physical observables

As mentioned in Sec. 2.4.1, the primary observable we use to characterize states is the spin susceptibility. Of the many possible ways of interpreting the susceptibility, we focus on two specific points of view. Microscopic correlations and ordering instabilities are most obvious in the static spin-spin correlator in the local basis, which is equal to the spin susceptibility

$$\chi_{\Omega=0}^{\mu\mu}(\mathbf{q}) = \frac{1}{N} \sum_{ij} e^{i\mathbf{q}(\mathbf{r}_i - \mathbf{r}_j)} \int d\tau \langle \mathcal{T} S_i^\mu(\tau) S_j^\mu(0) \rangle. \quad (5.1)$$

This correlator has only two independent components due to the U(1) symmetry of the XXZ Hamiltonian, namely $\chi^z \equiv \chi^{zz}$ and $\chi^\perp \equiv \chi^{xx} = \chi^{yy}$.

To compare to experiments, we calculate the inelastic neutron scattering structure factor (see Sec. 2.4.2), which is very directly related to the spin-spin correlator in the global basis. Following Fenell et al. [10], we decompose the inelastic neutron scattering structure factor $\mathcal{S}(\mathbf{q})$ into the spin-flip

$$\mathcal{S}_{\text{SF}}(\mathbf{q}) \equiv \int d\Omega \mathcal{S}_{\text{SF}}(\mathbf{q}, \Omega) = \sum_{\mu\lambda} \frac{(\mathbf{P} \times \mathbf{q})^\mu (\mathbf{P} \times \mathbf{q})^\lambda}{\|\mathbf{q}\|^2} \tilde{\chi}^{\mu\lambda}(\mathbf{q}) \Big|_{\tau=0} \quad (5.2)$$

and non-spin-flip channels

$$\mathcal{S}_{\text{NSF}}(\mathbf{q}) \equiv \int d\Omega \mathcal{S}_{\text{NSF}}(\mathbf{q}, \Omega) = \sum_{\mu\lambda} P^\mu P^\lambda \tilde{\chi}^{\mu\lambda}(\mathbf{q}) \Big|_{\tau=0}, \quad (5.3)$$

where the neutron polarization vector is $\mathbf{P} = (+1, -1, 0)$. This decomposition helps to identify signature patterns of dipole correlations, which predominantly occur in the spin-flip channel. Furthermore, experimental data to compare to is available for this setup.

These two quantities thus form a connection between microscopic theory and experimental observables, though they are both merely different components of the same type of correlator.

5.4 Ordered phases

At⁴ $\theta = 180^\circ$ and -90° (\diamond and \square in Fig. 5.1), interactions are not frustrated and ferromagnetic order develops. This is visible in Fig. 5.6(b, c) as a divergence

⁴In this section, we only discuss results for $\theta = 180^\circ$ and $\theta = -90^\circ$, where the system shows conventional long-range order in $\langle S_i^\mu S_j^\mu \rangle$. The state at $\theta = 90^\circ$ will be discussed separately in Sec. 5.6, though a nematic order has been proposed for this point in the phase diagram in prior work [28, 43, 63].

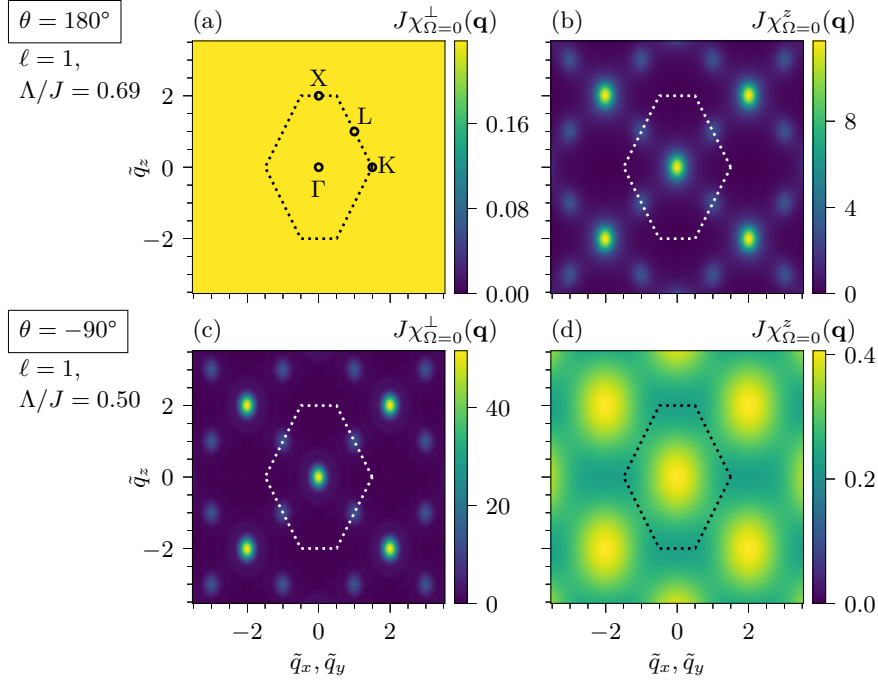


Figure 5.6: Static susceptibility in the local basis $\chi_{\Omega=0}^{\mu\mu}(\mathbf{q})$ at $\theta = 180^\circ$ and -90° (\diamond and \square in Fig. 5.1), where we find ordered phases. Shown is the $q_x = q_y$ plane in reciprocal space (see Fig. 5.2), where plot axes are expressed in terms of the rescaled (unitless) wave vector $\tilde{\mathbf{q}} = \frac{\sqrt{2}}{\pi} a \mathbf{q}$, and dashed lines show the boundary of the extended Brillouin zone. Data shown is the last stable solution obtained from multiloop pffRG flows with $\ell = 1$. (a, b) Static susceptibility at $\theta = 180^\circ$ showing a sharp Bragg peak at $\mathbf{q}_\Gamma = (0, 0, 0)^T$ in the χ^z component, indicating AIAO order. (c, d) Static susceptibility at $\theta = -90^\circ$ showing a sharp Bragg peak at $\mathbf{q}_\Gamma = (0, 0, 0)^T$ in the χ^\perp component, indicating AF_\perp order.

in the spin-spin correlator at $\mathbf{q}_\Gamma = (0, 0, 0)^T$ in the component with nonzero coupling. The resulting ordered ground state can be identified by the position of the divergences. At $\theta = 180^\circ$, there is no interaction in the S^x - S^y plane and the model is effectively an Ising ferromagnet. The local S^z -components of the spins are aligned due to ferromagnetic interaction J^z , which corresponds to the *all-in-all-out* (AIAO) order shown in Fig. 2.3. Thus, all correlations $\langle S_i^x S_j^x \rangle$ and $\langle S_i^y S_j^y \rangle$ are zero except for the on-site component $i = j$. In Fourier space, this corresponds to an entirely featureless constant correlator $\chi_{\Omega=0}^\perp(\mathbf{q})$ (see Fig. 5.6(a)). At $\theta = -90^\circ$, the spins align in the *local* S^x - S^y plane due to ferromagnetic interaction $J^x = J^y$, leading to large antiparallel components in the *global* basis. Therefore, this type of order is called the *easy-plane antiferromagnet* (AF_\perp). As the XXZ model is symmetric under global

5. Results

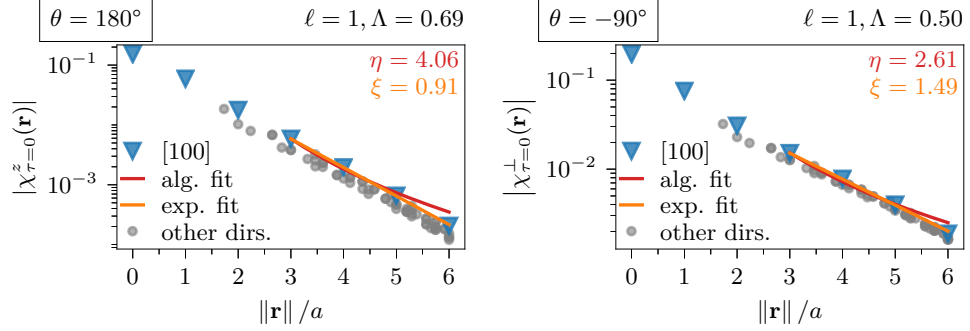


Figure 5.7: Decay of equal-time spin-spin correlations $\langle S_i^\mu S_j^\mu \rangle$ as a function of distance in real space in the ordered phases at $\theta = 180^\circ$ and $\theta = -90^\circ$ (\diamond and \square in Fig. 5.1). Shown is the dominant component of the zero-time spin susceptibility $\chi_{\tau=0}^{\mu\mu}(\mathbf{r})$ as a function of distance $\|\mathbf{r}\|$. To test whether the decay for large distances is algebraic or exponential, we fit an algebraic decay $\sim \|\mathbf{r}\|^{-\eta}$ (dark red) and an exponential decay $\sim e^{-\|\mathbf{r}\|/\xi}$ (light orange) to the data points in [100]-direction (triangles) at distances $\|\mathbf{r}\| > 2a$ (one unit cell). In both ordered phases, the data is consistent with exponential decay. Fit results are shown in detail in Tab. 5.2.

rotation of spins within the local S^x - S^y plane, there is an infinite number of equivalent states that satisfy this order; two examples are shown in Fig. 2.3.

The behavior of the divergent component $\chi_{\Omega=0}^\perp$ at $\theta = -90^\circ$ is extremely similar to the behavior of $\chi_{\Omega=0}^z$ at $\theta = 180^\circ$, as may be expected due to the similar structure of interactions (see Fig. 5.6(b, c)): At $\theta = 180^\circ$, the interaction is Ising-like ($J^z = -J$ and $J^x = J^y = 0$), while at $\theta = -90^\circ$, the interaction is purely transverse ($J^x = J^y = -J$ and $J^z = 0$). However, going from $\theta = 180^\circ$ to $\theta = -90^\circ$ is not simply a rotation in spin space that would correspond to an exchange of the corresponding components χ^z and χ^\perp , as is evident from comparison of the non-divergent channels (see Fig. 5.6(a, d)). The reason for this is that the effective Ising Hamiltonian at $\theta = 180^\circ$ only contains S^z terms, while the Hamiltonian at $\theta = -90^\circ$ contains two distinct terms, one quadratic in S^x and one quadratic in S^y . These generate correlations between S^z components indirectly. In pseudofermion fRG, this is implemented in the flow equations, which generate correlations in Γ^3 from a bare vertex which is only nonzero in the $\Gamma_0^1 = \Gamma_0^2$ component, but not *vice versa*.

In real space, an ordered state is expected to show exponential decay in the spin-spin correlator $\langle S_i^\mu S_j^\mu \rangle$, with a correlation length ξ that diverges as $\Lambda \rightarrow 0$. This divergence is limited by the finite cutoff radius r_{\max} in our calculations. Quantum spin ice states, on the other hand, are predicted to show algebraic decay in the equal-time spin-spin correlator $\langle S_i^\mu S_j^\mu \rangle$ [38, 42, 99]. To study the type of decay, we fit both an algebraic function $\sim \|\mathbf{r}\|^{-\eta}$ and an exponential $\sim e^{-\|\mathbf{r}\|/\xi}$ to data points at a distance $> 2a$ (one unit cell)

		$\theta = 180^\circ$	$\theta = -90^\circ$
alg. fit	exponent η	4.06	2.61
	standard deviation	0.22	0.20
	SSR	4.4×10^{-8}	7.4×10^{-7}
exp. fit	correlation length ξ	0.9097	1.487
	standard deviation	0.0032	0.022
	SSR	1.6×10^{-10}	2.4×10^{-8}

Table 5.2: Results of fitting algebraic decay $\sim \|\mathbf{r}\|^{-\eta}$ and exponential decay $\sim e^{-\|\mathbf{r}\|/\xi}$ to the spin-spin correlations in real space at $\theta = 180^\circ$ and -90° shown in Fig. 5.7. Shown are the best fit parameters η and ξ , the standard deviation in that parameter and the sum of squared residuals (SSR). The SSR for the exponential decay fit is more than one order of magnitude smaller than for algebraic decay. This indicates that exponential decay fits the data significantly better, as is expected for an ordered state.

in the direction⁵ [100], i.e. along the first unit vector $\mathbf{a}_1 = \sqrt{2}a(1, 1, 0)^T$. This direction is where we observe the slowest decay of correlations, though the decay is almost uniform in all directions. Data points and the result of these fits are shown in Fig. 5.7. As an indicator of how well the data is modeled by the decay function, we calculate the sum of squared residuals (SSR)

$$\text{SSR} = \sum_n \left| f(\|\mathbf{r}_n\|) - \chi_{\tau=0}^{\mu\mu}(\mathbf{r}_n) \right|^2, \quad (5.4)$$

where \mathbf{r}_n are the available data points in [100] direction and f is the fit function. A small SSR indicates good fit of the data to the chosen decay function. The values we obtained for the best fit as well as the standard deviation and SSR resulting from this procedure are listed in Tab. 5.2. The SSR for exponential decay is more than one order of magnitude smaller than for algebraic decay, confirming our expectation of an exponential decay.

Patterns of scattering peaks in the neutron scattering structure factors, shown in Fig. 5.8, clearly indicate the presence of long-range order. Clear differences in the pattern between $\theta = 180^\circ$ and $\theta = -90^\circ$ allow identification of the state in experiment. For example, neutron scattering at $\text{NaCaCo}_2\text{F}_7$ with small energy transfer⁶ produces a pattern [19, Figs. 4(a) and 8(a)] that

⁵This is the direction along one of the nearest-neighbor bonds. Depending on the definition of the basis vectors, the same direction may be labeled differently in terms of Miller indices: Our convention uses the basis vectors corresponding to a minimal, non-cubic unit cell; thus, there is a basis vector parallel to the nearest-neighbor bond and this direction is considered [100]. Some prior work prefers a cubic unit cell, in which case the definition of the basis vectors changes such that this direction is considered ‘[110]’.

⁶The pattern for large energy transfer includes excitation into states with symmetry-breaking collinear order [19] that are inaccessible to our method due to enforced symmetries of the vertex (see Sec. 4.1.5).

5. Results

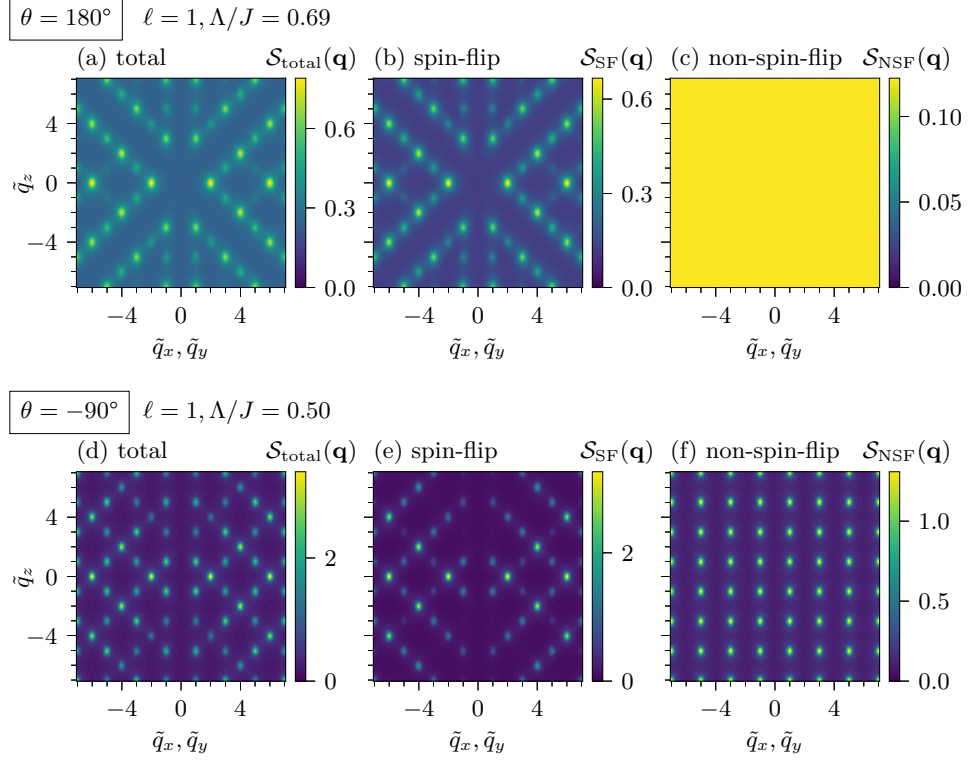


Figure 5.8: Neutron scattering structure factor as a function of the rescaled scattering vector $\tilde{\mathbf{q}} = \frac{\sqrt{2}}{\pi} \mathbf{a}\mathbf{q}$ in the ordered phases. Shown is (a, d) the total structure factor $\mathcal{S}_{\text{total}}(\mathbf{q})$ and its decomposition into (b, e) the spin-flip channel \mathcal{S}_{SF} and (c, f) non-spin flip channels \mathcal{S}_{NSF} (see Sec. 2.4.2). (a–c) Neutron scattering structure factor for the state at $\theta = 180^\circ$ (\diamond in Fig. 5.1), where we find AIAO order. (d–f) Neutron scattering structure factor for the state at $\theta = -90^\circ$ (\square in Fig. 5.1), where we find AF_\perp order. Data shown is the last stable solution obtained from multiloop pffRG flows with $\ell = 1$. Both phases show patterns of scattering peaks indicating presence of long-range order.

matches our results for $\theta = -90^\circ$ (see Fig. 5.8(d)), indicating presence of easy-plane antiferromagnetic (AF_\perp) order.

5.5 Quantum spin ice

For antiferromagnetic J^z at $\theta = -1^\circ$ and 20° (\circ and \diamond in Fig. 5.1), the system is highly frustrated. Prior analytical work [38, 60] predicted two quantum spin ice phases in the vicinity of $\theta = 0^\circ$ that are described by the same effective U(1) field theory. The two phases differ in the background flux enclosed by each hexagonal plaquette of the dual lattice (see Sec. 2.3). For $\theta < 0$, this background flux is 0, while for $\theta > 0$, the background flux takes the value π [60]. Following the notation of Benton et al. [28], we label these phases QSI_0 and QSI_π , respectively. The QSI_π is predicted to be stable phase up to the SU(2) point at $\theta = 45^\circ$ [28, 60]. This claim cannot be confirmed using Quantum Monte Carlo techniques due to a sign problem in this part of the phase diagram [28, 43]. The predicted transition point at $\theta = 45^\circ$, where the XXZ model becomes a SU(2)-symmetric Heisenberg model, has been studied extensively in the past. Prior work consistently predicted absence of order at this point, though the exact nature of the ground state has proven difficult to identify [31, 32, 39, 40, 44, 47, 57, 100–106].

Our results for the static spin susceptibility at $\theta = -1^\circ$ and $\theta = 20^\circ$, shown in Fig. 5.9, have smooth structures without sharp divergent peaks. This indicates the absence of any long-range order, consistent with the above-mentioned predictions [38, 58, 60]. The structure of the χ^z component with a minimum at \mathbf{q}_Γ and a plateau along the edge of the extended Brillouin zone corresponds to antiferromagnetic correlations. The bow tie and pinch point structures at \mathbf{q}_X and \mathbf{q}_L are signatures of algebraic decay in correlations typical for spin liquid states. The pattern we obtain at $\theta = -1^\circ$ for χ^z is consistent with prior work on quantum spin ice [107, Fig. 9].

At $\theta = 20^\circ$, the χ^z component (see Fig. 5.9(d)) shows antiferromagnetic correlations that are very similar to those at $\theta = -1^\circ$ (see Fig. 5.9(b)), indicating behavior close to quantum spin ice. Due to the frustrated transverse coupling J^x , the transverse component χ^\perp shows similar antiferromagnetic correlations as well (see Fig. 5.9(c)). The patterns we obtain are similar to results for the antiferromagnetic SU(2) Heisenberg model ($\theta = 45^\circ$) from prior work⁷ [31, 32, 39, 47, 57, 105, 106]. This is evidence in favor of the stability of the QSI_π phase up to $\theta = 45^\circ$ claimed in Ref. [28]. A careful analysis of the quantum phase transition near $\theta = 45^\circ$ would be intriguing, though accessing the low-temperature behavior at this point in the phase diagram is notoriously

⁷See Refs. [31, Fig. 4, 32, Fig. 6, 39, Fig. 3, right panel, 47, Fig. 5(d), 57, Fig. 13(a), 105, Fig. 7, upper left panel, 106, Fig. 6, last column]. Note that these prior publications exclusively use the *local* spin basis S^μ . Therefore, the definition of the ‘static structure factor $S(\mathbf{Q})$ ’ used there is proportional to our definition of the ‘static susceptibility in the local spin basis $\chi_{\Omega=0}^{\mu\mu}(\mathbf{q})$ ’.

5. Results

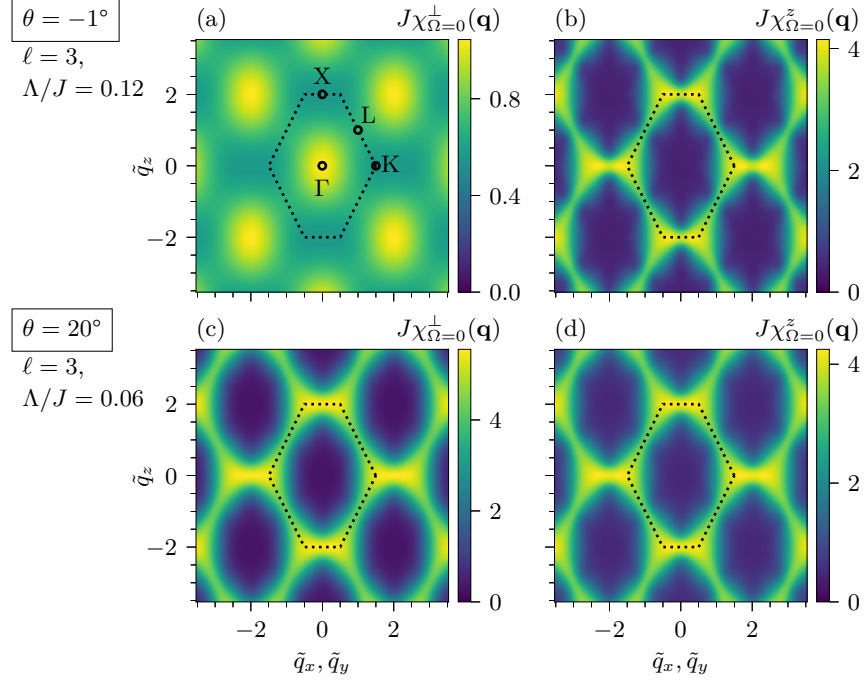


Figure 5.9: Static susceptibility in the local basis $\chi_{\Omega=0}^{\mu\mu}(\mathbf{q})$ at $\theta = -1^\circ$ and 20° (○ and ◻ in Fig. 5.1), where we find quantum spin ice phases. Shown is the $q_x = q_y$ plane in reciprocal space (see Fig. 5.2), where plot axes are expressed in terms of the rescaled (unitless) wave vector $\tilde{\mathbf{q}} = \frac{\sqrt{2}}{\pi}a\mathbf{q}$, and dashed lines show the boundary of the extended Brillouin zone. At both points in the phase diagram, we find absence of sharp Bragg peaks, indicating a state without long-range order. (a, b) Static susceptibility at $\theta = -1^\circ$. The dominant χ^z component has a maximal plateau along the edge of the extended Brillouin zone, corresponding to antiferromagnetic correlations, and bow tie patterns consistent with a quantum spin ice state. The χ^\perp component shows ferromagnetic correlations, indicated by the maximum at the origin \mathbf{q}_Γ . These are much weaker than the correlations in S^z -direction because of the much weaker coupling $J^x < J^z$. (c, d) Static susceptibility at $\theta = 20^\circ$. The χ^z component is very similar to χ^z at $\theta = -1^\circ$, and we conclude that $\theta = 20^\circ$ corresponds to a quantum spin ice state as well. The χ^\perp component shows antiferromagnetic correlations instead of ferromagnetic ones due to the sign change in J^x at $\theta = 0^\circ$.

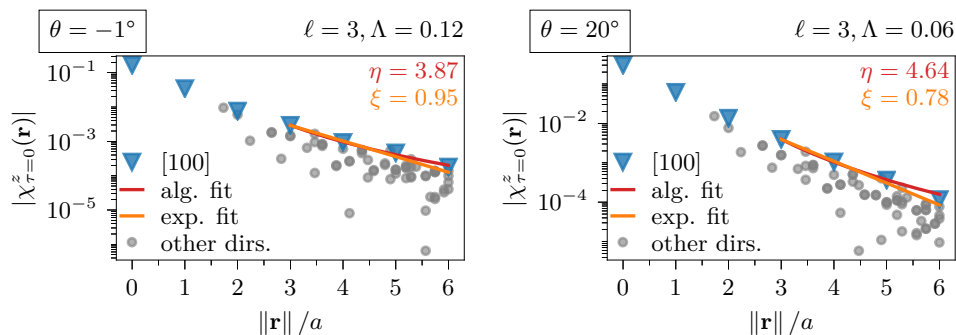


Figure 5.10: Decay of spin-spin correlations in real space in the quantum spin ice phases at $\theta = -1^\circ$ and $\theta = 20^\circ$ (\circ and \diamond in Fig. 5.1). Shown is the dominant component of the zero-time spin susceptibility $\chi_{\tau=0}^z$ as a function of distance $\|\mathbf{r}\|$. To test whether the decay for large distances is algebraic or exponential, we fit an algebraic decay $\sim \|\mathbf{r}\|^{-\eta}$ (dark red) and an exponential decay $\sim e^{-\|\mathbf{r}\|/\xi}$ (light orange) to the data points in [100]-direction (triangles) at distances $\|\mathbf{r}\| > 2a$ (one unit cell). In the spin ice phases, both fits produce similar sums of squared residuals. Fit results are shown in detail in Tab. 5.3.

		$\theta = -1^\circ$	$\theta = 20^\circ$
alg. fit	exponent η	3.87	4.637
	standard deviation	0.13	0.089
	SSR	3.5×10^{-5}	6.2×10^{-5}
exp. fit	correlation length ξ	0.954	0.783
	standard deviation	0.077	0.028
	SSR	3.5×10^{-5}	6.2×10^{-5}

Table 5.3: Results of fitting algebraic decay $\sim \|\mathbf{r}\|^{-\eta}$ and exponential decay $\sim e^{-\|\mathbf{r}\|/\xi}$ to the spin-spin correlations in real space at $\theta = -1^\circ$ and 20° shown in Fig. 5.10. Shown are the best fit parameters η and ξ , the standard deviation in that parameter and the sum of squared residuals (SSR). The almost identical SSR indicates that both functions fit the decay of correlations equally well within the available data. To distinguish algebraic and exponential decay, simulations on larger lattices are necessary.

difficult [57, 106, 108]. Therefore, it is left for future work, where we plan to map out the phase diagram of the XXZ model on the pyrochlore lattice.

For quantum spin ice phases, prior work predicts a power-law decay of spin-spin correlations in real space

$$\langle S_i^z(0) S_j^z(0) \rangle \sim \|\mathbf{r}_i - \mathbf{r}_j\|^{-\eta} \quad (5.5)$$

5. Results

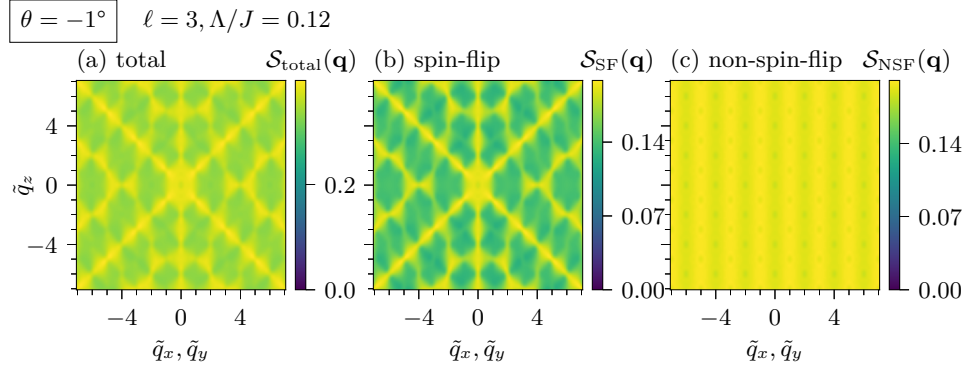


Figure 5.11: Neutron scattering structure factor at $\theta = -1^\circ$ (\circ in Fig. 5.1) as a function of rescaled scattering vector $\tilde{\mathbf{q}} = \frac{\sqrt{2}}{\pi} a \mathbf{q}$. Shown is (a) the total structure factor $\mathcal{S}_{\text{total}}(\mathbf{q})$, and its decomposition into (b) the spin-flip channel $\mathcal{S}_{\text{SF}}(\mathbf{q})$ and (c) the non-spin flip channel $\mathcal{S}_{\text{NSF}}(\mathbf{q})$ (see Sec. 2.4.2). We find a pattern of pinch points and a minimum at the origin $\tilde{\mathbf{q}} = (0, 0, 0)^T$, consistent with prior work on QSI₀.

at large distances $\|\mathbf{r}_i - \mathbf{r}_j\|$, where $\eta = 4$ near $\theta = 0^\circ$ [38, 42, 99]. We are able to extract predictions for this correlator $\langle S_i^z(0) S_j^z(0) \rangle = \chi_{\tau=0}^z(\mathbf{r})$ from our data, and these are shown in Fig. 5.10. To study the type of decay, we fit both algebraic decay $\sim e^{-\|\mathbf{r}\|/\xi}$ and exponential decay $\sim \|\mathbf{r}\|^{-\eta}$ to data points at a distance $> 2a$ (one unit cell) in the direction [100], where we observe the slowest decay of correlations. Contrary to the fairly uniform decay of correlations in all directions for the ordered states discussed in the previous section, the data points at $\theta = -1^\circ$ and 20° show complex dependence on direction, as is typical for frustrated antiferromagnetic correlations [38]. The best fits produce nearly identical sums of squared residuals (see Tab. 5.3), in contrast to the ordered case, where exponential decay was clearly preferred. However, this is not enough to conclude that algebraic decay is indeed present, and simulations with increased maximum correlation length r_{max} are necessary to determine the type of decay at large distance. Already with the cutoff used here, the exponent $\eta = 3.87 \pm 0.13$ we obtain for algebraic decay is remarkably close to the analytical value of $\eta = 4$ at $\theta = -1^\circ$, though it is unclear whether this will still be true for increased r_{max} .

To compare to prior work, both experimental and theoretical, we calculate the neutron scattering structure factors, which are shown in Fig. 5.11 and Fig. 5.13. For instance, our result for the spin-flip structure factor at $\theta = -1^\circ$, shown in Fig. 5.11(b), is similar to patterns observed in the low-energy part⁸ for the quantum spin ice candidate Pr₂Zr₂O₇ [16, Fig. 3, 24, Fig. 3(c)], as

⁸Scattering with high energy transfer in Pr₂Zr₂O₇ is affected by structural disorder [24], which is not part of our model.

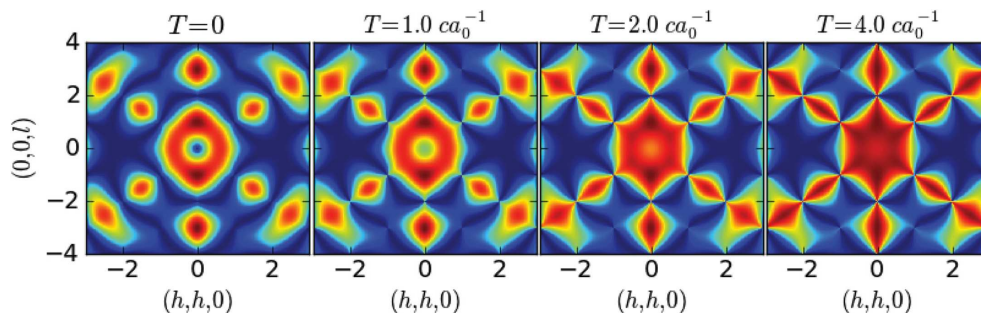


Figure 5.12: Comparison between Quantum Monte Carlo neutron scattering structure factors in the spin-flip channel, \mathcal{S}_{SF} , for a quantum spin ice state at different temperatures. Our results for $\theta = -1^\circ$ at zero temperature, shown in Fig. 5.11(b), are most similar to the second and third panel as opposed to the zero-temperature Quantum Monte Carlo result. Units used in this plot: $h = \tilde{q}_x = \tilde{q}_y$, $l = \tilde{q}_z$. Note that the unit lengths on the vertical and horizontal axis have an aspect ratio of $1 : \sqrt{2}$ here, whereas we use an aspect ratio of $1 : 1$ in all other figures. The unit of temperature corresponds to $ca_0^{-1} \approx 0.02J$. Adapted with permission from Benton et al. [107, Fig. 16].

well as the pattern produced by the classical spin ice material $\text{Ho}_2\text{Ti}_2\text{O}_7$ [10, Fig. 2A]. Prior work indicates that the differences in the non-spin-flip channel are due to additional, longer-ranged interactions, which are not part of our model [10].

To determine whether the state predicted here is closer to classical or quantum spin ice, we compare to prior theoretical work. Our results for $\theta = -1^\circ$ (see Fig. 5.11) reproduce the quantum spin ice structure factor close to the Ising point $\theta = 0^\circ$ that was found in prior work [107, Fig. 1(b, c) and Fig. 16, 109, Fig. 3(a)]. For ease of reference, an adapted version of Fig. 16 from Ref. [107] is included here as Fig. 5.12. This figure shows the spin flip channel $\mathcal{S}_{\text{SF}}(\mathbf{q})$ and can therefore be compared directly with our Fig. 5.11(b).

We find pinch points at $\tilde{\mathbf{q}} = (1, 1, 1)^T$ in the spin-flip structure factor, indicating presence of algebraic correlations characteristic for a $U(1)$ spin liquid [43]. Compared to the classical spin liquid state at $\theta = 0^\circ$, quantum fluctuations induced by finite $J^x = J^y$ have been predicted to suppress the value of \mathcal{S}_{SF} at the pinch points and at the origin $\tilde{\mathbf{q}} = (0, 0, 0)^T$ [107]. In our results, these effects seem to be much weaker than in prior work, though the reason may simply be proximity to the classical spin ice phase at $\theta = 0^\circ$. Direct comparison to data at finite temperature, shown in Fig. 5.12, reveals that our results match predictions for small but non-zero temperature more closely than zero-temperature data. This can be explained by the role of the IR cutoff Λ , which acts similar to a finite temperature T in the sense that it suppresses low-energy modes [50]. Based on arguments in the large N limit, a direct mapping $\Lambda \rightarrow \frac{2}{\pi}T$ has been proposed in prior work [47, 50, 57],

5. Results

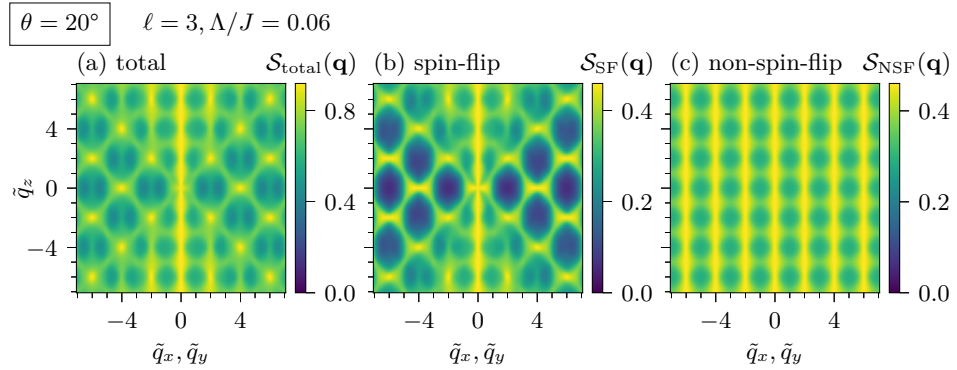


Figure 5.13: Neutron scattering structure factor at $\theta = 20^\circ$ (\diamond in Fig. 5.1) as a function of rescaled scattering vector $\tilde{\mathbf{q}} = \frac{\sqrt{2}}{\pi} a \mathbf{q}$. Shown is (a) the total structure factor $\mathcal{S}_{\text{total}}(\mathbf{q})$, and its decomposition into (b) the spin-flip channel $\mathcal{S}_{\text{SF}}(\mathbf{q})$ and (c) the non-spin flip channel $\mathcal{S}_{\text{NSF}}(\mathbf{q})$ (see Sec. 2.4.2).

though this mapping from the energy cutoff in our zero-temperature formalism should be carefully distinguished from a true finite-temperature calculation. Nevertheless, through this correspondence, our results at finite $\Lambda/J \approx 0.1$ are expected to be roughly similar to a system at T/J of the same order of magnitude. With this assumption, there is excellent agreement between our data and Quantum Monte Carlo simulations (see Fig. 5.12, see also [109, Fig. 3(a)]). It would be interesting to observe whether the predicted structure factor still undergoes significant changes when integrated to smaller Λ/J . This is possible in principle as we showed for the Heisenberg model [51], though more work is necessary to overcome some technical challenges related to accurate representation of the vertex at all values of Λ/J (see Sec. 5.1).

At $\theta = 20^\circ$, the structure factor, shown in Fig. 5.13, forms patterns that are qualitatively different from the case at $\theta = -1^\circ$. In the spin-flip channel (see Fig. 5.13(a)), a chain of bow ties replaces the very prominent diagonals of the $\theta = -1^\circ$ case (compare Fig. 5.11(b)). The bow tie patterns at $\tilde{q}_x = \tilde{q}_y > \tilde{q}_z$ that indicate algebraic correlations remain, consistent with our expectation of a spin liquid state. In the non-spin-flip channel, which is almost featureless at $\theta = -1^\circ$ (see Fig. 5.11), a pattern of diamond shapes arranged in a regular grid appears (see Fig. 5.13(c)). These qualitative differences make the neutron scattering structure factor a suitable indicator for the low-temperature phase in experiments.

Since interactions are frustrated in all components at values of $\theta > 0^\circ$, Quantum Monte Carlo methods are not applicable due to the sign problem. Predictions for the structure factor that can be compared with our results are therefore scarce in this region of the phase diagram. Classical Monte Carlo calculations give results similar to ours for the structure factors in the SU(2) Heisenberg model at $\theta = 45^\circ$ [43, Fig. 2(c)]. From this perspective, the state at

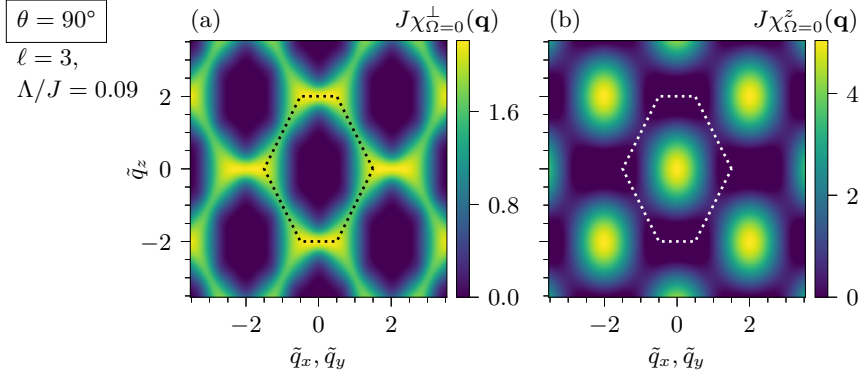


Figure 5.14: Static susceptibility in the local basis $\chi_{\Omega=0}^{\mu\mu}(\mathbf{q})$ at $\theta = 90^\circ$ (Δ in Fig. 5.1), where we find an easy-plane quantum spin liquid phase. Shown is the $q_x = q_y$ plane in reciprocal space (see Fig. 5.2), where plot axes are expressed in terms of the rescaled (unitless) wave vector $\tilde{\mathbf{q}} = \frac{\sqrt{2}}{\pi} a \mathbf{q}$, and dashed lines show the boundary of the extended Brillouin zone. We find absence of sharp Bragg peaks, indicating a state without long-range order. (a) The χ^\perp component has maxima along the boundary of the extended Brillouin zone, consistent with antiferromagnetic correlations in the S^x - S^y plane found in an easy-plane quantum spin liquid. (b) The χ^z component shows strong ferromagnetic correlations as maximum around the origin, which are generated indirectly by the $J^x = J^y$ coupling.

$\theta = 20^\circ$ seems to be remarkably similar to $\theta = 45^\circ$ despite the different ratio J^x/J^z , as we already noted based on similarities in the spin-spin correlations.

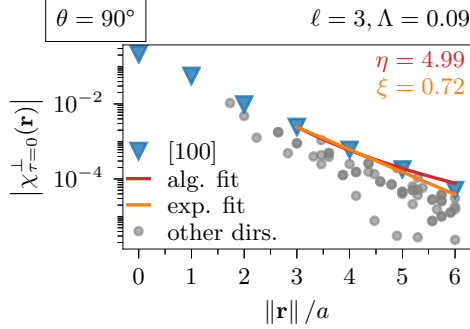
5.6 Easy-plane quantum spin liquid

At θ significantly above⁹ 45° , the dominant component of the coupling is $J^x = J^y > J^z$. Since the system is still frustrated in all components, a transition from QSI_π with dominant correlations in S^z to some form of $\text{U}(1) \times \text{U}(1)$ spin-liquid state with dominant correlations in the S^x - S^y plane may be expected, and has indeed been proposed in the past [28]. Schematically, such states can be generated by

$$|\text{nematic}_\perp\rangle = g^z(\phi) g^y\left(\frac{\pi}{2}\right) |\text{QSI}_\pi\rangle, \quad (5.6)$$

⁹We do not discuss $\theta \approx 45^\circ$ here, as it is unknown whether the ground state of the $\text{SU}(2)$ Heisenberg model at $\theta = 45^\circ$ is a third phase distinct from those at θ significantly above and below 45° . As mentioned previously, there has been extensive research on this ground state [31, 32, 39, 40, 44, 47, 57, 100–106], without consensus so far. Additionally, behavior similar to quantum criticality might also influence the states around the $\text{SU}(2)$ point [28]. Therefore, study of this transition is left to future work, where we plan to map out the phase diagram of the XXZ model on the pyrochlore lattice.

5. Results



$\theta = 90^\circ$		
alg. fit	η	4.99 ± 0.12
	SSR	2.4×10^{-5}
exp. fit	ξ	0.724 ± 0.018
	SSR	2.4×10^{-5}

Figure 5.15: Results of fitting exponential decay $\sim e^{-\|\mathbf{r}\|/\xi}$ and algebraic decay $\sim \|\mathbf{r}\|^{-\eta}$ to the spin-spin correlations in real space at $\theta = 90^\circ$ (Δ in Fig. 5.1). Shown are the best fit parameters η and ξ , the standard deviation in that parameter and the sum of squared residuals (SSR). The almost identical SSR indicates that both functions fit the decay of correlations equally well within the available data. To distinguish algebraic and exponential decay, simulations on larger lattices are necessary.

where $g^\mu(\phi)$ is a rotation around axis μ by ϕ in spin space. However, there is an important difference to the quantum spin ice states discussed in the previous section: As the Hamiltonian is symmetric under rotations g^z , such a state is necessarily symmetry-breaking, i.e. it shows *nematic order*. Prior work based on cluster variational methods [28, 43] predicts a nematic spin liquid ground state for $45^\circ < \theta < 110^\circ$.

Our result for the spin susceptibility at $\theta = 90^\circ$ (Δ in Fig. 5.1) is shown in Fig. 5.14. As no Bragg peaks form at any \mathbf{q} , this state is paramagnetic. The shape of χ^\perp with its plateau along the edge of the extended Brillouin zone, shown in Fig. 5.14(a), confirms our expectation of antiferromagnetic correlations in the S^x - S^y plane. Similar to the ferromagnetic case at $\theta = -90^\circ$, the coupling in J^x and J^y indirectly generates ferromagnetic correlations in χ^z , which are visible as a maximum at $\mathbf{q}_\Gamma = (0, 0, 0)^T$ (see Fig. 5.14(b)). Though these correlations are remarkably strong, the peak has a finite width much larger than that of a divergent peak that would indicate an instability to long-range order.

In real space, the decay of correlations is again consistent with a spin liquid in the S^x - S^y plane (see Fig. 5.15). We find very similar behavior in $\chi_{\tau=0}^\perp(\mathbf{r})$ as we observed for $\chi_{\tau=0}^z(\mathbf{r})$ at $\theta = -1^\circ$ and 20° , with complex dependence of correlations on direction. The fit to exponential and algebraic decay produces an inconclusive result with nearly identical SSR, as it did for $\theta = -1^\circ$ and 20° .

The neutron scattering structure factor, shown in Fig. 5.16, shows features that are easily distinguishable from those in quantum spin ice: While bowtie structures remain at large $q_x = q_y$ in the spin-flip channel (Fig. 5.16(b)), the 6-spoke wheel structure that is characteristic for quantum spin ice is absent.

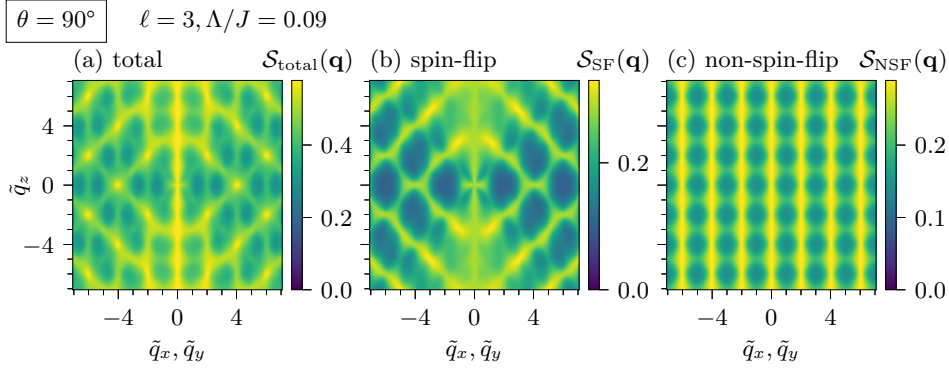


Figure 5.16: Neutron scattering structure factor at $\theta = 90^\circ$ (Δ in Fig. 5.1) as a function of rescaled scattering vector $\tilde{\mathbf{q}} = \frac{\sqrt{2}}{\pi} \mathbf{a}\mathbf{q}$. Shown is (a) the total structure factor $\mathcal{S}_{\text{total}}(\mathbf{q})$, and its decomposition into (b) the spin-flip channel $\mathcal{S}_{\text{SF}}(\mathbf{q})$ and (c) the non-spin flip channel $\mathcal{S}_{\text{NSF}}(\mathbf{q})$ (see Sec. 2.4.2).

At large $q_z > q_x = q_y$, a broad, diffuse structure becomes visible. The non-spin-flip channel (see Fig. 5.16(c)) shows a grid of diamonds similar to its structure at $\theta = 20^\circ$ (see Fig. 5.13(c)). Thus, an easy-plane quantum spin liquid is most easily identified in the spin-flip channel.

Concerning the symmetry-breaking, nematic nature of the QSN_\perp phase described by Taillefer et al. [43], our analysis has to remain incomplete within the scope of this thesis. Though an expectation value for the nematic order parameter from Eq. (2.12) for the S^x - S^y plane,

$$O_{ij}^{xy} = \frac{1}{2}(S_i^x S_j^y + S_j^x S_i^y), \quad (5.7)$$

can be evaluated in our formalism, the value of $\langle O_{ij}^{xy} \rangle$ is zero because of the enforced $U(1)$ symmetry of the vertex (see Sec. 4.1.2 and 4.1.4). Positive identification of nematic order can be made in two ways: Evaluation of the order parameter susceptibility, a quadrupolar expectation value with four spin operators [43, Appendix B], is difficult within our formalism, though it might in principle be possible to obtain an estimate. Alternatively, an approach in the spirit of prior pffRG investigations of possible dimer and plaquette orders [50] can be pursued by introducing a slight asymmetry $J^x = J^y + \varepsilon$, which should be enhanced during the flow and lead to significant asymmetry in correlations for a nematic state.

Summary and outlook

We implemented a multiloop functional renormalization group approach to spin systems in the pseudofermion representation. We derived explicit flow equations for the XXZ model and implemented multiple lattices, among them the pyrochlore lattice, as well as many technical improvements to the numerical approaches that are used by our implementation. At many points, in particular concerning the frequency parametrization, we found that implementation details are crucial for the success of this method. On the technical level, our results show loop convergence for large Λ , though some numerical problems lead to numerical artifacts below $\Lambda/J = 0.1$ for some parameter choices. Consistent with our work on the kagome Heisenberg model [51], we find that the pseudofermion constraint is not inherently fulfilled in pseudofermion fRG, independent of loop order.

On the physical side, our method is able to give predictions for spin-spin correlators and neutron scattering cross sections. These physical observables can be directly compared to prior theoretical work and experimental data. Guided by the phase diagram Benton et al. [28] obtained using cluster mean-field and cluster variational methods, we chose five values of θ that are predicted to have different ground states to test the method. Comparison of our data to predictions given by other methods, including Quantum Monte Carlo where available, shows excellent correspondence for all choices of θ . This includes three quantum spin liquids and two ordered states. For some values of θ , the calculated neutron scattering cross section is recognizably similar to those found in some experiments on rare-earth pyrochlore oxides. Concerning the algebraic decay of correlations predicted for quantum spin ice in prior work [38], further investigation with larger system size is necessary to verify whether the states found by our method satisfy that prediction.

Our results reinforce that multiloop fRG is a powerful, versatile tool suitable for many systems, and that this includes spin systems in the pseudofermion representation. The latter in particular is a non-trivial statement, as the validity of the pffRG approach is not clear a priori due to its inherent

strong-coupling nature. Together with results presented elsewhere [51] and the parallel work of Kiese et al. [57], we conclude that multiloop pffRG is a consistent approach with applicability to arbitrary Heisenberg-type spin systems. In particular, it is one of very few approaches to frustrated three-dimensional systems. The consistency of our results with those obtained using other methods, where available, is strong evidence for the reliability of multiloop pffRG.

However, there are many open questions. Numerical artifacts caused by insufficient resolution of some vertex components prevent us from exploring the small- Λ regime of the spin liquid states. Though we find loop convergence at large $\Lambda/J > 0.1$, this does not imply loop convergence for smaller values of Λ , and further work is required to find a way to construct dynamic frequency meshes that resolve all vertex components accurately at all values of Λ in the XXZ flow. We do not expect this to be more difficult than for the Heisenberg model in principle, though a practical implementation is non-trivial.

Once this problem has been resolved, states at very small Λ/J can be investigated further. One quantity that is particularly interesting in this context is the self-energy Σ , as there are analytical predictions for its behavior in different types of states. Verifying consistency with other analytical predictions such as the power-law decay of correlations in real space would then also be possible through numerically more expensive simulations with larger cutoff radius r_{\max} .

Another physical prediction that has not yet been verified is the nematic instability of the easy-plane quantum spin liquid at $\theta = 90^\circ$. This may be investigated by breaking the U(1) symmetry of the XXZ Hamiltonian with a small asymmetric term in the interaction. The implementation of the mRG flow for the non-symmetric system would require some further effort. Furthermore, the reduced symmetry of the system leads to more required computation time, though there are no conceptual obstacles to this approach. Using a similar method, possible dimer order can be investigated as well.

Finally, having shown that multiloop pseudofermion fRG is applicable to this model for all θ , the next step would be to produce a phase diagram of the pyrochlore XXZ model. This would be particularly valuable as pseudofermion fRG does not suffer the drawbacks commonly associated with mean-field methods and related approaches. Most important for accurate prediction of quantum phase transition points is its ability to treat disordered and ordered phases on equal footing without bias. At the cost of increased computation time and memory requirements, this phase diagram can also be extended to the case of less symmetric interactions. Once a general model is implemented, an intriguing possibility might be to use values for the bare coupling constants in the Hamiltonian obtained using an experimental setup described by Ross et al. [20]. Thereby, multiloop pffRG predictions for observables could be compared to experiment in an even more direct way.

The pyrochlore lattice

Though the general approach to handling lattice symmetries of the vertex was already presented in Sec. 4.1.5, the steps described there are not entirely trivial and we will briefly show how the pyrochlore lattice is represented in practice.

A.1 Definition

The pyrochlore lattice is a face-centered cubic lattice with a 4-site unit cell [20, 70]. The unit cell is a tetrahedron centered on the origin with sites at its corners

$$\begin{aligned} \mathbf{r}_0 &= \frac{a}{2\sqrt{2}} (+1, +1, +1)^T, & \mathbf{r}_1 &= \frac{a}{2\sqrt{2}} (+1, -1, -1)^T, \\ \mathbf{r}_2 &= \frac{a}{2\sqrt{2}} (-1, +1, -1)^T, & \mathbf{r}_3 &= \frac{a}{2\sqrt{2}} (-1, -1, +1)^T, \end{aligned} \quad (\text{A.1})$$

where a is the distance between nearest neighbors. This unit cell is repeated with the translation operator group $\{T_{\mathbf{r}}\}_{\mathbf{r} \in \mathbb{Z}^3}$, where the action of $T_{\mathbf{r}}$ is a translation by $r^1 \mathbf{a}_1 + r^2 \mathbf{a}_2 + r^3 \mathbf{a}_3$. The vectors $\mathbf{a}_{1,2,3}$ are standard fcc basis vectors

$$\mathbf{a}_1 = \frac{2a}{\sqrt{2}} (1, 1, 0)^T, \quad \mathbf{a}_2 = \frac{2a}{\sqrt{2}} (1, 0, 1)^T, \quad \mathbf{a}_3 = \frac{2a}{\sqrt{2}} (0, 1, 1)^T, \quad (\text{A.2})$$

corresponding to a cubic unit cell with side length $a_{\text{fcc}} \equiv 4a/\sqrt{2}$. Now, each site can be enumerated by a tuple \mathbf{r} and an index $c \in \{0, 1, 2, 3\}$, such that the site (\mathbf{r}, c) is at position $T_{\mathbf{r}} \mathbf{r}_c$.

A.2 Symmetries of vertices on a pyrochlore lattice

In the following, we will present the symmetries of the pyrochlore lattice in a slightly unusual way. Our goal when using these symmetries is to automatically

A. The pyrochlore lattice

detect those components of the vertex that are related by symmetry. As the two-particle vertices $\gamma_{r;i_1,i_2}^{\mu;\Omega,\nu,\nu'}$ have two site arguments i_1 and i_2 , this is effectively a discussion of the symmetries of pairs of sites on the pyrochlore lattice.

We will identify symmetry-related components in a multi-step process. Given a pair of sites $i_1 = (\mathbf{r}_1, c_1)$ and $i_2 = (\mathbf{r}_2, c_2)$, the first goal is to find a site i' such that the pair $\{i', (\mathbf{0}, 0)\}$ is equivalent to $\{i_1, i_2\}$. To this end, we apply the translation operator $T_{-\mathbf{r}_2}$ to both sites and get

$$T_{-\mathbf{r}_2} \left\{ \begin{array}{l} (\mathbf{r}_1, c_1) \\ (\mathbf{r}_2, c_2) \end{array} \right\} = \left\{ \begin{array}{l} (\mathbf{r}_1 - \mathbf{r}_2, c_1) \\ (\mathbf{0}, c_2) \end{array} \right\}. \quad (\text{A.3})$$

Now, symmetry operators can be used to transform both sites such that c_2 is mapped to 0, reducing the two-argument pair to a single, equivalent argument i' . One possible choice of symmetry operators are the rotations $\{Q^c\}_{c=0,1,2,3}$ described below. These operators satisfy $Q^c(\mathbf{0}, c) = (\mathbf{0}, 0)$ for each c , such that

$$Q^{c_2} T_{-\mathbf{r}_2} \left\{ \begin{array}{l} (\mathbf{r}_1, c_1) \\ (\mathbf{r}_2, c_2) \end{array} \right\} = \left\{ \begin{array}{l} Q^{c_2}(\mathbf{r}_1 - \mathbf{r}_2, c_1) \\ (\mathbf{0}, 0) \end{array} \right\}, \quad (\text{A.4})$$

and we can identify $i' = Q^{c_2}(\mathbf{r}_1 - \mathbf{r}_2, c_1) = Q^{c_2} T_{-\mathbf{r}_2} i_1$.

To give explicit expressions for the operators Q^c , some notation has to be introduced. We denote symmetry operators Q in terms of a matrix U , a displacement \mathbf{j}_c and a permutation P . The effect of Q acting on an arbitrary site (\mathbf{r}, c) is

$$Q(\mathbf{r}, c) = (U\mathbf{r} + \mathbf{j}_c, Pc). \quad (\text{A.5})$$

Permutations are specified by listing their cycles, where each cycle is enclosed by parentheses. For example, $P = (123)$ means that P maps 1 to 2, 2 to 3 and 3 to 1; 0 is unchanged by P and not denoted explicitly.

Using this notation, the operators Q^c are

$$U^0 = \begin{pmatrix} 1 & 0 & 0 \\ 0 & 1 & 0 \\ 0 & 0 & 1 \end{pmatrix}, \quad \mathbf{j}_c^0 = (0, 0, 0), \quad P^0 = (), \quad (\text{A.6a})$$

$$U^1 = \begin{pmatrix} 0 & 1 & 0 \\ 1 & 0 & 0 \\ -1 & -1 & -1 \end{pmatrix}, \quad \mathbf{j}_c^1 = (0, 0, 0), \quad P^1 = (01)(23), \quad (\text{A.6b})$$

$$U^2 = \begin{pmatrix} 0 & 0 & 1 \\ -1 & -1 & -1 \\ 1 & 0 & 0 \end{pmatrix}, \quad \mathbf{j}_c^2 = (0, 0, 0), \quad P^2 = (02)(13), \quad (\text{A.6c})$$

$$U^3 = \begin{pmatrix} -1 & -1 & -1 \\ 0 & 0 & 1 \\ 0 & 1 & 0 \end{pmatrix}, \quad \mathbf{j}_c^3 = (0, 0, 0), \quad P^3 = (03)(12), \quad (\text{A.6d})$$

where $P^0 = ()$ is the identity. Now that an effective displacement $i' = Q^{c_2} T_{-r_2} i_1$ has been obtained such that the pair $\{i', (\underline{0}, 0)\}$ is equivalent to $\{i_1, i_2\}$, all vertex components can be held in memory as function of a single site argument. There are some remaining symmetries that reduce the number of independent arguments even further. However, these symmetries have to be formulated such that each symmetry operator Q always leaves $(\underline{0}, 0)$ invariant to avoid spoiling the equivalence of i' to the original pair of arguments.

A.3 Symmetry reduction of the effective displacement

In the following, we will list a generating set for the point group of the pyrochlore lattice that leaves $(\underline{0}, 0)$ invariant¹.

Inversion symmetry The pyrochlore lattice is symmetric under inversion at site $(\underline{0}, 0)$. In terms of the index tuples, this symmetry operator is defined through

$$U^{\text{inv}} = \begin{pmatrix} -1 & 0 & 0 \\ 0 & -1 & 0 \\ 0 & 0 & -1 \end{pmatrix}, \quad \begin{array}{l} \underline{j}_0^{\text{inv}} = (0, 0, 0), \\ \underline{j}_1^{\text{inv}} = (0, 0, 1), \\ \underline{j}_2^{\text{inv}} = (0, 1, 0), \\ \underline{j}_3^{\text{inv}} = (1, 0, 0), \end{array} \quad P^{\text{inv}} = (). \quad (\text{A.7})$$

Three-fold rotation symmetry There is a three-fold rotation symmetry around the $(1, 1, 1)^T$ axis, corresponding to

$$U^{\text{rot}} = \begin{pmatrix} 0 & 1 & 0 \\ 0 & 0 & 1 \\ 1 & 0 & 0 \end{pmatrix}, \quad \underline{j}_c^{\text{rot}} = (0, 0, 0), \quad P^{\text{rot}} = (123). \quad (\text{A.8})$$

Mirror symmetry The lattice is symmetric under reflection at the plane perpendicular to $(+1, -1, 0)^T$. This corresponds to

$$U^{\text{mirr}} = \begin{pmatrix} 0 & 1 & 0 \\ 1 & 0 & 0 \\ 0 & 0 & 1 \end{pmatrix}, \quad \underline{j}_c^{\text{mirr}} = (0, 0, 0), \quad P^{\text{mirr}} = (12). \quad (\text{A.9})$$

This set $\{Q^{\text{inv}}, Q^{\text{rot}}, Q^{\text{mirr}}\}$ can be used to find all displacements i' that are equivalent through a simple search algorithm. It is sufficient to apply all symmetry operators to i' and then iteratively to all displacements that

¹The set presented here is not the generating set with the minimal number of elements. A minimal set with only two operators, a screw-rotation and a six-fold roto-reflection, is analyzed in the work by Liu et al. [70]. The operators in that set contains operators that do not preserve $(\underline{0}, 0)$.

A. The pyrochlore lattice

were newly generated in the previous iteration until no new displacements are generated any more. The set of all displacements thus generated corresponds to vertex components that are identical. Thus, all components within the set can be symmetry-reduced to a single one.

Frequency meshes for pffRG

The frequency meshes we use to represent the self-energy and two-particle vertex are specified here. The basic structure of the frequency meshes is a cartesian product of symmetric 1d meshes with equidistant points around the origin and algebraic scaling at large frequencies. While the maximum frequency that is part of the mesh, i.e. the last frequency point, is pre-determined, the linear part is expanded or shrunk dynamically according to the structures that form in the vertex during the flow.

This approach is the same we used for the kagome Heisenberg model [51]. The algorithm was designed and implemented by Julian Thönni. It is described here, as our results would not be reproducible otherwise.

B.1 Structure of the frequency meshes

The meshes for bosonic frequencies Ω and fermionic frequencies ν, ν' have the same structure. We use w to describe general properties of both meshes, and substitute w with Ω and ν, ν' to recover the distinction between bosonic and fermionic arguments where necessary.

Each frequency mesh $\{w_i\}_i$ is symmetric around $w = 0$. The positive half contains two parts, divided by a threshold frequency w_{lin} : a linear mesh for small frequencies $w \in [0, w_{\text{lin}}]$, and an algebraic mesh for large frequencies $w \in (w_{\text{lin}}, w_{\text{max}}]$. On the linear part, the i -th frequency point w_i is at

$$w_i = \delta_{\text{lin}} \cdot i, \quad i \in \{0, \dots, n_{\text{lin}}\}, \quad (\text{B.1})$$

where $\delta_{\text{lin}} \cdot n_{\text{lin}} = w_{\text{lin}}$. On the algebraic part, the i -th frequency point w_i is at

$$w_i = w_{\text{lin}} + \delta_{\text{lin}} \cdot (i - n_{\text{lin}})^\alpha, \quad i \in \{n_{\text{lin}} + 1, \dots, n_{\text{tot}}\}, \quad (\text{B.2})$$

where $w_{\text{lin}} + \delta_{\text{lin}} \cdot (n_{\text{tot}} - n_{\text{lin}})^\alpha = w_{\text{max}}$ and $\alpha \geq 1$. The mesh of negative frequencies is obtained from this by mirroring the positive mesh at $w = 0$.

B. Frequency meshes for pffRG

component	frequency	mesh size	linear part	maximum frequency
		n_{tot}	n_{lin}	$\Omega_{\text{max}}, \nu_{\text{max}}$
Σ_ν	ν	4000	2400	$\max(150\Lambda, 70J)$
$K_{1r}^{\eta;\omega}$	ω	500	150	$\max(500\Lambda, 500J)$
$K_{2r}^{\eta;\omega,\nu}$	ω	125	37	$\max(300\Lambda, 140J)$
$K_{2r}^{\eta;\omega,\nu}$	ν	75	22	$\max(150\Lambda, 70J)$
$K_{3r}^{\eta;\omega,\nu,\nu'}$	ω	30	9	$\max(150\Lambda, 70J)$
$K_{3r}^{\eta;\omega,\nu,\nu'}$	ν, ν'	22	13	$\max(70\Lambda, 35J)$

Table B.1: Values of some constants as they were chosen to produce the data shown in this thesis. The values given here describe the positive part of each mesh; the full mesh has twice the number of frequency points in each dimension.

The frequency mesh as defined above is entirely determined by the parameters $n_{\text{lin}}, n_{\text{tot}}, w_{\text{lin}}, w_{\text{max}}$. To control runtime and memory usage, the number of frequency points n_{lin} and n_{tot} is manually set before the start of each simulation run and needs to be chosen such that the required resolution is achieved. During the simulation, i.e. while integrating the fRG flow, the parameters $w_{\text{lin}}, w_{\text{max}}$ are adjusted such that all features in the data are properly resolved, even as their position and width changes.

Generally, the linear part of the mesh contains 30% of the frequency points (i.e. $n_{\text{lin}} = 0.3n_{\text{tot}}$). As the $K_3^{\eta;\omega,\nu,\nu'}$ class also contains sharp features that are not centered at the origin in the fermionic frequencies ν and ν' , the mesh of fermionic frequencies for K_3 is constructed with $n_{\text{lin}} = 0.6n_{\text{tot}}$, such that also these features are well resolved. Values are shown in Tab. B.1.

B.2 Dynamic adjustment algorithm

When adjusting a frequency mesh to a given vertex, our algorithm first chooses an appropriate w_{max} large enough to contain all features. It is generally sufficient to let w_{max} shrink proportional to Λ with the flow, until a minimum w_{max} is reached. The minimum w_{max} is chosen based on observation. Values are shown in Tab. B.1.

Having chosen w_{max} , an iterative algorithm searches for an appropriate value of w_{lin} . In each iteration, a heuristic is evaluated to determine whether a given linear frequency mesh is appropriate to resolve the central part of a given function. Depending on the heuristic, the mesh spacing δ_{lin} is then reduced or expanded, and the same heuristic is applied to the new mesh. The function is represented using the old mesh throughout this adjustment process, as multiple interpolation might distort features.

The heuristic used to determine whether to shrink or expand the mesh spacing comprises a set of criteria, given below. As these criteria examine the

data only at a few frequency points, they are only useful in connection with a few assumptions about the shape of the function. These assumptions are fulfilled by the vertex components in all phases and at all values of Λ ; however, the algorithm using this heuristic should not be regarded as a general-purpose algorithm for arbitrary functions.

These criteria might give conflicting information. The heuristic is biased towards shrinking the mesh spacing in this case. This has a few reasons: The conflicting information might be due to improperly resolved features around the origin. Furthermore, features move closer to the origin with the flow; many features scale proportional to or quicker than Λ . Expanding the mesh spacing is also generally more dangerous, as information about features close to the origin might be lost.

B.3 Criteria for the adjustment heuristic

The following is a list of criteria the heuristic uses to examine a frequency mesh, given data points $(w, f(w))$ of a vertex component that should be represented on the new mesh. Except where stated explicitly, all other frequencies are set to 0 when evaluating criteria for vertex components with multiple dimensions, e.g. $f(w) = K_{2r}^{\eta;0,w}$ for the fermionic mesh of the K_2 class.

1. Curvature close to the origin. Instead of directly evaluating the curvature, we use the quantity

$$C = \frac{f(w_{c+1}) - f(w_c)}{f(w_c) - f(w_{c-1})}, \quad (\text{B.3})$$

for some index c close to the origin. This is an approximation to a ratio of slopes that changes depending on the curvature at w_c :

$$C \approx \frac{f'(w_c + \delta_{\text{lin}}/2)}{f'(w_c - \delta_{\text{lin}}/2)}. \quad (\text{B.4})$$

To measure the curvature close to the origin, c should be close to 0. The algorithm then tries to adjust the frequency mesh such that C is close to a target value C_{target} . If it is significantly larger, the distance between mesh points is too small. If $C < 0$, the mesh spacing is too large. As the mesh contains significantly more frequencies in K_1 than in all other classes, we choose a target $C_{\text{target}} = 0.45$ at $c = 6$ for K_1 , and a target $C_{\text{target}} = 0.75$ at $c = 3$ for all other components.

2. Sign change. Some components change their sign as a function of frequency and therefore contain two peaks, as all components fall off to 0 at large frequencies. Enough frequency points must be distributed before and after the sign change to properly resolve both the peak around the origin and the peak that follows the sign change. If there is a sign change between w_0 and some frequency point w_z , the mesh spacing is too large. We choose $z = 3$.

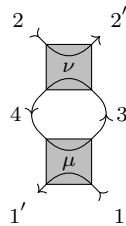
B. Frequency meshes for pffRG

3. Slope between the origin and the first frequency point. If the slope $L = |f(w_0) - f(w_1)|$ is very small, one can afford a larger frequency spacing. We demand $L \geq 0.2 |f(w_0)|$.
4. Minimum mesh spacing. Some components develop very sharp cusp-like features around the origin at $\Lambda < J$. This, together with the bias to shrink the mesh, might lead to very small linear meshes and insufficient resolution of features not directly at 0 frequency. Therefore, the algorithm is prevented from choosing $\delta_{\text{lin}} < 0.05\Lambda$.
5. Monotonic behavior close to the origin in K_{3t}^0 . The component $K_{3t}^{0;\omega,\nu,\nu'}$ is antisymmetric in ν and ν' . Apart from a cusp at the origin, all features (several peaks) are at finite ν, ν' . To ensure sufficient resolution of these features, the values of $f(w) = K_{3t}^{0;0,w,w}$ should be monotonically growing across the first M frequency points, i.e. $|f(w_0)| < |f(w_1)| < \dots < |f(w_M)|$. We choose $M = 5$.

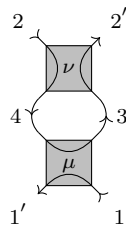
Fast convolution for RPA-type diagrams

The main numerical effort in calculating diagrams is the numerical integration over Matsubara frequencies. Therefore, reducing the number of integrations that need to be performed leads to a near-proportional reduction in runtime and memory usage.

In principle, the frequency integrals in a particular bubble diagram have to be executed for every combination of non-frequency arguments (site indices and spin direction indices) separately. The number of permissible combinations is reduced significantly by constraints that are imposed by the structure of the vertex, such as the bi-local structure (see Eq. (4.9)). RPA diagrams, that is, diagrams that contain free bubbles such as



are not constrained in the site argument $i_3 = i_4$ of the internal propagators, while all other bubble diagrams are. Because of this, RPA diagrams require far more runtime to evaluate. For translation-invariant systems, the cost of non-RPA diagrams such as



C. Fast convolution for RPA-type diagrams

is proportional to the number of independent real-space components of the vertex, which is parametrized according to Eq. (4.37) as $\Gamma_{c_1 c_2}(\underline{\mathbf{r}})$. We use the definitions

N number of unit cells used in the calculation,

B number of sites per unit cell, and

b number of sites in the symmetry-reduced unit cell, where $(1 \leq b \leq B)$.

As $\underline{\mathbf{r}}$ enumerates unit cells, there are N independent values of $\underline{\mathbf{r}}$. The indices c_1 and c_2 can take B^2 different values, of which only Bb are independent after symmetry reduction. Therefore, the total number of components of Γ scales $\mathcal{O}(BbN)$, and the cost of evaluating non-RPA diagrams is proportional to this.

RPA diagrams, meanwhile, scale $\mathcal{O}(B^2 b N^2)$ due to the additional site summation over i_3 , which can take BN distinct values. The cost of evaluating each combination of argument values is similar, and RPA-type diagrams are therefore much more costly to integrate than other diagrams. In practice, the majority of computation time is spent calculating the RPA bubble for usual parameter choices.

C.1 Convolution structure of the RPA bubble

In a translation-invariant system, the scaling behavior of the RPA bubble can be improved using fast convolution algorithms. Going back from diagrammatic to symbolic notation, the RPA bubble reads

$$\begin{aligned}
 B_{i_1 i_2}(\omega'_1, \omega'_2; \omega_1, \omega_2) &= - \sum_{34} \text{Diagram} = \\
 &= - \sum_{i_3} \sum_{\omega_3 \omega_4} \Gamma_{i_1 i_3}(\omega'_1, \omega_3; \omega_1, \omega_4) \Gamma'_{i_3 i_2}(\omega_4, \omega'_2; \omega_3, \omega_2) G(\omega_3) G(\omega_4), \quad (\text{C.1})
 \end{aligned}$$

where Γ, Γ' are arbitrary vertex-like quantities such as the full vertex or some reducible parts. For clarity, the frequency indices will be dropped in the following. Due to the local structure of the propagators the real-space structure is entirely contained in the indices of $\Gamma \Gamma'$:

$$\Phi_{i_1 i_2} \equiv \sum_{i_3} \Gamma_{i_1 i_3} \Gamma'_{i_3 i_2}. \quad (\text{C.2})$$

On a lattice, all unit cells are translation-symmetric to one another, while the sites within each unit cell are not necessarily symmetric to one another. To exploit lattice symmetries of the vertices, we use the same notation as in Sec. 4.1.5 and decompose each site index i into a translation index $\underline{\mathbf{r}} \in \mathbb{Z}^d$

and an index for sites within each unit cell $c \in \mathbb{J}_B = \{1, \dots, B\}$. Translation symmetry of the vertex (4.37)

$$\Gamma_{i_1 i_2} = \Gamma_{c_1 c_2}(\mathbf{r}_1, \mathbf{r}_2) = \Gamma_{c_1 c_2}(\mathbf{r}_1 - \mathbf{r}_2) \quad (\text{C.3})$$

immediately leads to translation symmetry of Φ

$$\Phi_{c_1 c_2}(\mathbf{r}_1, \mathbf{r}_2) = \sum_{c_3=1}^B \sum_{\mathbf{r}_3} \Gamma_{c_1 c_3}(\mathbf{r}_1 - \mathbf{r}_3) \Gamma'_{c_3 c_2}(\mathbf{r}_3 - \mathbf{r}_2) = \Phi_{c_1 c_2}(\mathbf{r}_1 - \mathbf{r}_2), \quad (\text{C.4})$$

and there is a convolution structure in the \mathbf{r} arguments in the sum. Therefore, the scaling behavior of the calculation can be improved using one of the known fast convolution algorithms. In the next sections, an algorithm with better scaling behavior based on the convolution theorem and fast Fourier transform (FFT) will be derived.

C.2 Circular convolution theorem

Restricting the discussion to one dimension for simplicity, the convolution of two functions $f, g: \mathbb{R} \rightarrow \mathbb{R}$ is defined as

$$(f * g)(x) = \int_{\mathbb{R}} dy f(x - y) g(y). \quad (\text{C.5})$$

The convolution theorem states that the Fourier transformed convolution of two functions f, g is equal to the product of the Fourier transformed functions [110], i.e.¹

$$\text{FT}[f * g](k) = \sqrt{2\pi} \text{FT}[f](k) \cdot \text{FT}[g](k). \quad (\text{C.6})$$

However, the above equation is not immediately useful for numerical applications since the functions f and g as well as their Fourier transformed counterparts have continuous and infinite support \mathbb{R} . As only a finite number of samples can be held in memory, we require a version of the convolution theorem that makes it possible to calculate a discrete convolution of discrete functions (sequences) $f, g: \mathbb{Z} \rightarrow \mathbb{R}$, defined as

$$(f * g)(x) = \sum_{y \in \mathbb{Z}} f(x - y) g(y), \quad (\text{C.7})$$

using only discrete functions with finite support. Unfortunately, the Fourier transform of f and g is still continuous unless f and g are periodic.

Restricting f, g to be periodic functions $f(x + n) = f(x), g(x + n) = g(x)$ with period n for the moment, there is indeed an analogue of the convolution

¹Depending on the normalization of the Fourier transform, the normalization factor in this equation may be different.

C. Fast convolution for RPA-type diagrams

theorem (C.6). The appropriate version of the Fourier transform to use here is the discrete Fourier transform (DFT), which transforms discrete and periodic functions [110, 111]:

$$\mathcal{F}[f](k) = \frac{1}{\sqrt{n}} \sum_{x=0}^{n-1} e^{-ikx} f(x), \quad (\text{C.8})$$

where $k \in \frac{2\pi}{n}\mathbb{Z}$ and $\mathcal{F}[f](k)$ is 2π -periodic, with n values of k in each period.

The circular convolution theorem states that for two such functions f, g , the DFT of the circular convolution,

$$(f \circledast g)(x) = \sum_{y=0}^{n-1} f(x-y) g(y), \quad (\text{C.9})$$

is equal to the product of the DFTs of the functions² [110]:

$$\mathcal{F}[f \circledast g](k) = \sqrt{n} \mathcal{F}[f](k) \cdot \mathcal{F}[g](k). \quad (\text{C.10})$$

While superficially similar to (C.6), this equation requires f and g to be periodic, as an aperiodic function has a continuous Fourier transform and the DFT would not be applicable here. To calculate the discrete convolution of aperiodic functions with finite support $x \in \left\{-\left\lfloor \frac{L}{2} \right\rfloor, \dots, \left\lceil \frac{L}{2} \right\rceil - 1\right\}$ using the circular convolution theorem, we define helper functions f_n, g_n with period n . Inside the first period, i.e. between $-\lfloor \frac{n}{2} \rfloor$ and $\lceil \frac{n}{2} \rceil - 1$, they are defined as

$$f_n(x) = \begin{cases} 0 & -\lfloor \frac{n}{2} \rfloor \leq x < -\lfloor \frac{L}{2} \rfloor, \\ f(x) & -\lfloor \frac{L}{2} \rfloor \leq x < \lceil \frac{L}{2} \rceil, \\ 0 & \lceil \frac{L}{2} \rceil \leq x < \lceil \frac{n}{2} \rceil, \end{cases} \quad (\text{C.11})$$

which effectively means zero-padding the function on both sides of the original domain. This period is then repeated infinitely:

$$f_n(x) = f_n(x+n) \quad \forall x. \quad (\text{C.12})$$

The same procedure is applied for g_n . Because of the zero-padding, the circular convolution of f_n and g_n coincides with the discrete convolution of f and g on some interval. The smallest n that is sufficient for our purposes is $n = \lceil \frac{3}{2}L \rceil - 1$, in which case this interval is exactly the domain where f and g were originally defined [110]:

$$(f_n \circledast g_n)(x) = (f * g)(x) \quad \text{for} \quad -\left\lfloor \frac{L}{2} \right\rfloor \leq x < \left\lceil \frac{L}{2} \right\rceil. \quad (\text{C.13})$$

²This property can also be understood in terms of linear algebra: Sequences of real numbers form a vector space, and because both the convolution and the DFT are linear, they can be described using matrices. Then, the Fourier basis is the basis in which the convolution is diagonal, and the Fourier transform is the matrix that diagonalizes the convolution.

Outside of this interval, the circular convolution and the discrete convolution differ³.

Therefore, the discrete convolution can be obtained through

$$(f * g)(x) = \sqrt{n} \mathcal{F}^{-1} \left[\mathcal{F}[f_n] \cdot \mathcal{F}[g_n] \right](x) \text{ for } - \left\lfloor \frac{L}{2} \right\rfloor \leq x < \left\lceil \frac{L}{2} \right\rceil, \quad (\text{C.14})$$

where \mathcal{F} is a length- n DFT. The generalization of this result to multiple dimensions is straightforward, as a multidimensional DFT can be defined by simply taking DFTs in orthogonal directions.

Using (C.14) combined with an FFT algorithm, discrete convolutions can be calculated with computational effort scaling as $\mathcal{O}(n \log n) = \mathcal{O}(L \log L)$ where L is the number of data points. For comparison, directly executing the sum in the definition of the convolution (C.7) yields an algorithm scaling as $\mathcal{O}(L^2)$, because L values of f and g must be added for each of the L values of x .

C.3 Discrete Fourier transform of vertices

Returning to the discussion of the RPA diagrams, their evaluation can be accelerated using (C.14). Before executing the DFT, a zero-padded and periodically repeated version Γ^p, Γ'^p of the vertices Γ, Γ' must first be constructed. If the vertex is calculated on a $N_1 \times \dots \times N_d$ grid⁴, the repeated version of the vertex has $n_1 \times \dots \times n_d$ entries, where $n_j \geq \left\lceil \frac{3}{2} N_j \right\rceil - 1$.

The DFT of a padded and repeated vertex Γ^p in its \mathbf{r} -argument (and all other objects with the same real-space structure) can be defined as

$$\mathcal{F} \left[\Gamma_{c_1 c_2}^p \right](\mathbf{k}) \equiv \frac{1}{\sqrt{n}} \sum_{\mathbf{r}} e^{-i \mathbf{k}^T \mathbf{r}} \Gamma_{c_1 c_2}^p(\mathbf{r}), \quad (\text{C.15})$$

where $n = \prod_{j=1}^d n_j$, $\mathbf{k} \in \frac{2\pi}{n_1} \mathbb{Z} \times \dots \times \frac{2\pi}{n_d} \mathbb{Z}$ and $\mathbf{k}^T \mathbf{r}$ is to be understood as a matrix product:

$$\mathbf{k}^T \mathbf{r} = \sum_{j=1}^d k^j r^j. \quad (\text{C.16})$$

³The interval where circular and discrete convolution coincide can be enlarged by choosing larger n , which is not necessary for our purposes. For example, for $n \geq 2L - 1$, the circular and discrete convolution are equal for $-\left\lfloor \frac{n}{2} \right\rfloor \leq x < \left\lceil \frac{n}{2} \right\rceil$, i.e. the interval where the discrete convolution has potentially nonzero value.

⁴When using a grid with boundaries that are not orthogonal (box-shaped) in \mathbf{r} -index space, it is necessary to temporarily switch to such a grid to perform the DFT. For example, in this thesis, we generally use a distance-based spherical cutoff in real space, which corresponds to an ellipsoid-like shape in index space. The DFT is then performed over the smallest box that contains all sites that fulfill the original cutoff criteria. Similarly, the inverse DFT results in a vertex that has values in a box-shaped region in index space, and all values outside the original cutoff boundary are discarded.

C. Fast convolution for RPA-type diagrams

The inverse Fourier transform corresponding to (C.15) is

$$\Gamma_{c_1 c_2}^p(\underline{\mathbf{r}}) = \frac{1}{\sqrt{n}} \sum_{\underline{\mathbf{k}}} e^{+i\underline{\mathbf{k}}^T \underline{\mathbf{r}}} \mathcal{F}[\Gamma_{c_1 c_2}^p](\underline{\mathbf{k}}), \quad (\text{C.17})$$

because

$$\frac{1}{n} \sum_{\underline{\mathbf{s}}} \sum_{\underline{\mathbf{k}}} e^{i\underline{\mathbf{k}}^T (\underline{\mathbf{r}} - \underline{\mathbf{s}})} \Gamma_{c_1 c_2}^p(\underline{\mathbf{s}}) = \Gamma_{c_1 c_2}^p(\underline{\mathbf{r}}). \quad (\text{C.18})$$

as all terms where $\underline{\mathbf{s}} \neq \underline{\mathbf{r}}$ cancel.

Inserting the inverse DFT (C.17) into (C.4),

$$\begin{aligned} \Phi_{c_1 c_2}(\underline{\mathbf{r}}_1 - \underline{\mathbf{r}}_2) &= \\ &= \sum_{c_3=1}^B \sum_{\underline{\mathbf{r}}_3} \frac{1}{n} \sum_{\underline{\mathbf{k}}_1, \underline{\mathbf{k}}_2} e^{i\underline{\mathbf{k}}_1^T (\underline{\mathbf{r}}_1 - \underline{\mathbf{r}}_3) + i\underline{\mathbf{k}}_2^T (\underline{\mathbf{r}}_3 - \underline{\mathbf{r}}_2)} \mathcal{F}[\Gamma_{c_1 c_3}^p](\underline{\mathbf{k}}_1) \mathcal{F}[\Gamma_{c_3 c_2}^p](\underline{\mathbf{k}}_2) = \\ &= \sum_{c_3=1}^B \sum_{\underline{\mathbf{k}}} e^{i\underline{\mathbf{k}}^T (\underline{\mathbf{r}}_1 - \underline{\mathbf{r}}_2)} \mathcal{F}[\Gamma_{c_1 c_3}^p](\underline{\mathbf{k}}) \mathcal{F}[\Gamma_{c_3 c_2}^p](\underline{\mathbf{k}}). \end{aligned} \quad (\text{C.19})$$

Thus, the whole bubble (C.1) can be evaluated as

$$\begin{aligned} B_{t c_1 c_2}(\underline{\mathbf{r}}_1 - \underline{\mathbf{r}}_2; \dots) &= \\ &= \sum_{\underline{\mathbf{k}}} e^{i\underline{\mathbf{k}}^T (\underline{\mathbf{r}}_1 - \underline{\mathbf{r}}_2)} \sum_{\omega_3 \omega_4} \sum_{c_3} \mathcal{F}[\Gamma_{c_1 c_3}^p](\underline{\mathbf{k}}; \dots) \mathcal{F}[\Gamma_{c_3 c_2}^p](\underline{\mathbf{k}}; \dots) G(\omega_3) G(\omega_4), \end{aligned} \quad (\text{C.20})$$

where the structure of the omitted frequency arguments is the same as in (C.1).

C.4 Symmetries of the Fourier-transformed vertex

Symmetries of the vertex in real space carry over to the Fourier-transformed vertex, as the information content of the Fourier-space vertex must be the same as in real space. While symmetries in frequency space remain the same, the Fourier-space version of other symmetries of the real-space vertex is less obvious.

In pseudofermion models without off-diagonal spin interactions, the vertex in real space is real [86]

$$\text{Im} \Gamma(\underline{\mathbf{r}}, \dots) = 0, \quad (\text{C.21})$$

which corresponds to

$$\Gamma^p(\underline{\mathbf{k}}, \dots) = [\Gamma^p(-\underline{\mathbf{k}}, \dots)]^* \quad (\text{C.22})$$

in Fourier space.

In addition, the model may be symmetric under lattice symmetries

$$Q(\underline{r}, c) = (U\underline{r} + \underline{j}_c, Pc), \quad (\text{C.23})$$

as described in Sec. 4.1.5. For a vertex, this means there is a set of constraints

$$\begin{aligned} \Gamma_{c_1 c_2}(\underline{r}_1 - \underline{r}_2) &= S \Gamma_{c_1 c_2}(\underline{r}_1 - \underline{r}_2) = \\ &= \Gamma_{Pc_1 Pc_2}(U\underline{r}_1 + \underline{j}_{c_1} - U\underline{r}_2 - \underline{j}_{c_2}) = \Gamma_{Pc_1 Pc_2}(U[\underline{r}_1 - \underline{r}_2] + \underline{j}_{c_1 c_2}), \end{aligned} \quad (\text{C.24})$$

where $j_{c_1 c_2} = j_{c_1} - j_{c_2}$. These constraints induce equivalent constraints in Fourier space:

$$\begin{aligned} \mathcal{F}[\Gamma_{c_1 c_2}^p](\underline{k}) &= \frac{1}{\sqrt{n}} \sum_{\underline{r}} e^{-i\underline{k}^T \underline{r}} \Gamma_{c_1 c_2}^p(\underline{r}) = \\ &= \frac{1}{\sqrt{n}} \sum_{\underline{r}} e^{-i\underline{k}^T \underline{r}} \Gamma_{Pc_1 Pc_2}^p(U\underline{r} + \underline{j}_{c_1 c_2}) = \\ &= \frac{1}{\sqrt{n}} \sum_{\underline{r}} e^{-i\underline{k}^T U^{-1}(\underline{r} - \underline{j}_{c_1 c_2})} \Gamma_{Pc_1 Pc_2}^p(\underline{r}) = \\ &= e^{i\underline{k}^T U^{-1} \underline{j}_{c_1 c_2}} \mathcal{F}[\Gamma_{Pc_1 Pc_2}^p]((U^{-1})^T \underline{k}). \end{aligned} \quad (\text{C.25})$$

Thus, the gain in efficiency due to lattice symmetries is almost the same in real and Fourier space. There is, however, some overhead for the fast convolution algorithm, as these symmetries cannot be used efficiently by the fast Fourier transform algorithm. Before performing the FFT, the vertex has to be expanded from its symmetry-reduced form to a memory layout that does not use any lattice symmetries. After the FFT, the Fourier-space symmetries can be used to reduce the Fourier-space vertex to a more efficient memory layout again. In practice, this overhead leads to a negligible increase in runtime, though it does increase memory consumption.

C.5 Complexity of the fast convolution

In total, the RPA bubbles can be evaluated using fast convolution as follows:

1. Expand the vertices from their symmetry-reduced form to a form suitable for FFT
2. Apply zero-padding in all directions
3. Fourier-transform the vertex
4. Symmetry-reduce the vertex in Fourier space
5. Evaluate (C.20)
6. Symmetry-expand the result in Fourier space
7. Apply the inverse Fourier transform to the result
8. Symmetry-reduce the result

C. Fast convolution for RPA-type diagrams

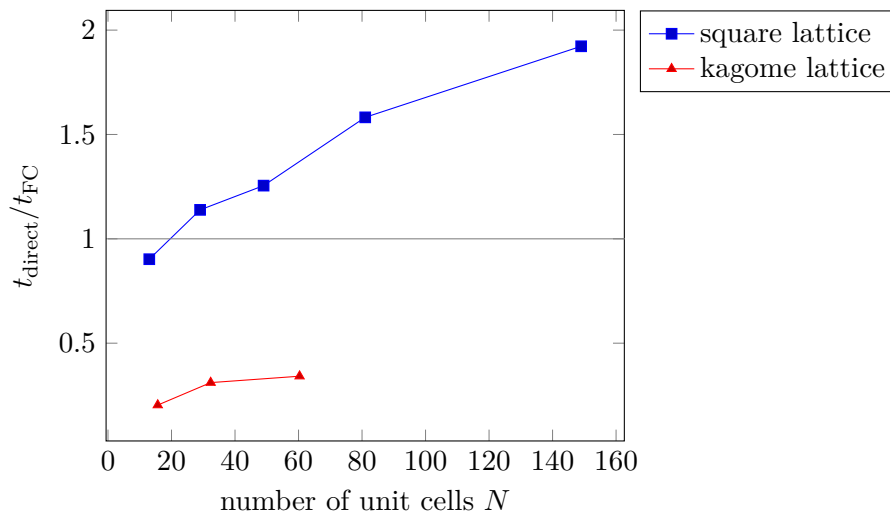


Figure C.1: Comparison of the runtime used to evaluate RPA-type diagrams over a 1-loop fRG flow from $\Lambda_i = 5$ to $\Lambda_f \approx 0.01$ in a disordered phase. t_{FC} is the runtime of the fast convolution algorithm and t_{direct} is the runtime needed for direct evaluation of (C.1).

Of these steps, the Fourier transform and its inverse scale most strongly with the number of unit cells $N = \prod N_j$. The zero-padded vertex has

$$Bbn = Bb \prod_j n_j = Bb \prod_j \left(\left\lceil \frac{3}{2} N_j \right\rceil - 1 \right) = \mathcal{O} \left(\left(\frac{3}{2} \right)^d BbN \right) \quad (\text{C.26})$$

entries. The Fourier transform (C.15) and its inverse (C.17) can be calculated with $\mathcal{O}(n \log n) = \mathcal{O}(N \log N)$ complexity using standard FFT algorithms described in the literature, such as the algorithm of Cooley and Tukey [112]. Implementations of these algorithms are widely available; our implementation uses the FFTW library [111]. As the algorithm involves one forward and one backward Fourier transform for each of the Bb combinations of two c parameters, the FFT steps scale as $\mathcal{O}(BbN \log N)$ in total.

In the evaluation of Φ and frequency integration (step 5, see Eq. (C.20)), there are B^2b distinct combinations of (c_1, c_2, c_3) and N distinct values of \underline{k} . The runtime scaling of the frequency integration is therefore $\mathcal{O}(B^2bN)$ for constant number of frequencies. As these integrations require $\geq 90\%$ of the runtime for practical values of N , this is the most important dependence.

The runtime complexity of symmetry expansion and reduction as well as zero-padding of a vertex scales proportional to the number of entries in the vertex, which in turn scales as $\mathcal{O}(Bbn)$ and therefore of a lower order than either the FFT or the frequency integration. This part is never dominant.

The numerical effort required for direct evaluation of (C.1) scales $\mathcal{O}(B^2bN^2)$, as BN expressions must be summed for each of the Bbn combinations of external site parameters. This means that direct evaluation of (C.1) is faster for

small N due to the overhead of the fast convolution, while fast convolution is faster for large N due to better runtime scaling (see Fig. C.1). Furthermore, the efficiency of the fast convolution algorithm and the value of N at which the benefits of the fast convolution compensate the added overhead depend strongly on properties of the lattice. For example, Fig. C.1 shows that on a square lattice, the fast convolution is beneficial for all but the smallest lattice sizes. On a kagome lattice, however, the lattice would have to be very large to compensate the overhead of fast convolution.

In 3d, the number of sites N required to extract meaningful results about physics of the system are expected to be larger than in 2d due to the additional dimension. Therefore, the fast convolution is expected to outperform direct evaluation on a cubic lattice. On a pyrochlore lattice, it seems unlikely that the increase in N which is expected for the same reason as on the cubic lattice is enough to compensate the overhead due to $B = 4$. Therefore, the FFT-based fast convolution was not implemented for the pyrochlore XXZ model.

Bibliography

- [1] L. Savary and L. Balents, “Quantum spin liquids: a review”, [Reports on Progress in Physics](#) **80**, 016502 (2017).
- [2] R. Moessner and S. L. Sondhi, “Resonating valence bond phase in the triangular lattice quantum dimer model”, [Physical Review Letters](#) **86**, 1881 (2001).
- [3] A. Y. Kitaev, “Fault-tolerant quantum computation by anyons”, [Annals of Physics](#) **303**, 2 (2003).
- [4] A. Y. Kitaev, “Anyons in an exactly solved model and beyond”, [Annals of Physics](#) **321**, 2 (2006).
- [5] J. S. Helton, K. Matan, M. P. Shores, E. A. Nytko, B. M. Bartlett, Y. Yoshida, Y. Takano, A. Suslov, Y. Qiu, J.-H. Chung, D. G. Nocera, and Y. S. Lee, “Spin dynamics of the spin-1/2 kagome lattice antiferromagnet $\text{ZnCu}_3(\text{OH})_6\text{Cl}_2$ ”, [Physical Review Letters](#) **98**, 107204 (2007).
- [6] M. R. Norman, “Colloquium : herbertsmithite and the search for the quantum spin liquid”, [Reviews of Modern Physics](#) **88**, 041002 (2016).
- [7] M. P. Shores, E. A. Nytko, B. M. Bartlett, and D. G. Nocera, “A structurally perfect $S = 1/2$ kagomé antiferromagnet”, [Journal of the American Chemical Society](#) **127**, 13462 (2005).
- [8] V. K. Anand, L. Opherden, J. Xu, D. T. Adroja, A. T. M. N. Islam, T. Herrmannsdörfer, J. Hornung, R. Schönemann, M. Uhlarz, H. C. Walker, N. Casati, and B. Lake, “Physical properties of the candidate quantum spin-ice system $\text{Pr}_2\text{Hf}_2\text{O}_7$ ”, [Physical Review B](#) **94**, 144415 (2016).
- [9] L.-J. Chang, S. Onoda, Y. Su, Y.-J. Kao, K.-D. Tsuei, Y. Yasui, K. Kakurai, and M. R. Lees, “Higgs transition from a magnetic coulomb liquid to a ferromagnet in $\text{Yb}_2\text{Ti}_2\text{O}_7$ ”, [Nature Communications](#) **3**, 992 (2012).

- [10] T. Fennell, P. P. Deen, A. R. Wildes, K. Schmalzl, D. Prabhakaran, A. T. Boothroyd, R. J. Aldus, D. F. McMorrow, and S. T. Bramwell, “Magnetic Coulomb phase in the spin ice $\text{Ho}_2\text{Ti}_2\text{O}_7$ ”, *Science* **326**, 415 (2009).
- [11] T. Fennell, M. Kenzelmann, B. Roessli, M. K. Haas, and R. J. Cava, “Power-law spin correlations in the pyrochlore antiferromagnet $\text{Tb}_2\text{Ti}_2\text{O}_7$ ”, *Physical Review Letters* **109**, 017201 (2012).
- [12] J. S. Gardner, M. J. Gingras, and J. E. Greedan, “Magnetic pyrochlore oxides”, *Reviews of Modern Physics* **82**, 53 (2010).
- [13] M. J. P. Gingras and P. A. McClarty, “Quantum spin ice: a search for gapless quantum spin liquids in pyrochlore magnets”, *Reports on Progress in Physics* **77**, 056501 (2014).
- [14] A. M. Hallas, J. Gaudet, and B. D. Gaulin, “Experimental insights into ground-state selection of quantum xy pyrochlores”, *Annual Review of Condensed Matter Physics* **9**, 105 (2018).
- [15] E. Kermarrec, D. D. Maharaj, J. Gaudet, K. Fritsch, D. Pomaranski, J. B. Kycia, Y. Qiu, J. R. D. Copley, M. M. P. Couchman, A. O. R. Morningstar, H. A. Dabkowska, and B. D. Gaulin, “Gapped and gapless short-range-ordered magnetic states with $(\frac{1}{2}, \frac{1}{2}, \frac{1}{2})$ wave vectors in the pyrochlore magnet $\text{Tb}_{2+x}\text{Ti}_{2-x}\text{O}_{7+\delta}$ ”, *Physical Review B* **92**, 245114 (2015).
- [16] K. Kimura, S. Nakatsuji, J.-J. Wen, C. Broholm, M. B. Stone, E. Nishibori, and H. Sawa, “Quantum fluctuations in spin-ice-like $\text{Pr}_2\text{Zr}_2\text{O}_7$ ”, *Nature Communications* **4**, 1934 (2013).
- [17] G. Pokharel, H. S. Arachchige, T. J. Williams, A. F. May, R. S. Fishman, G. Sala, S. Calder, G. Ehlers, D. S. Parker, T. Hong, A. Wildes, D. Mandrus, J. A. Paddison, and A. D. Christianson, “Cluster frustration in the breathing pyrochlore magnet $\text{LiGaCr}_4\text{S}_8$ ”, *Physical Review Letters* **125**, 167201 (2020).
- [18] J. G. Rau and M. J. Gingras, “Frustrated quantum rare-earth pyrochlores”, *Annual Review of Condensed Matter Physics* **10**, 357 (2019).
- [19] K. A. Ross, J. W. Krizan, J. A. Rodriguez-Rivera, R. J. Cava, and C. L. Broholm, “Static and dynamic XY-like short-range order in a frustrated magnet with exchange disorder”, *Physical Review B* **93**, 014433 (2016).
- [20] K. A. Ross, L. Savary, B. D. Gaulin, and L. Balents, “Quantum excitations in quantum spin ice”, *Physical Review X* **1**, 021002 (2011).
- [21] R. Sibille, N. Gauthier, E. Lhotel, V. Porée, V. Pomjakushin, R. A. Ewings, T. G. Perring, J. Ollivier, A. Wildes, C. Ritter, T. C. Hansen, D. A. Keen, G. J. Nilsen, L. Keller, S. Petit, and T. Fennell, “A quantum liquid of magnetic octupoles on the pyrochlore lattice”, *Nature Physics* **16**, 546 (2020).

-
- [22] R. Sibille, E. Lhotel, M. C. Hatnean, G. Balakrishnan, B. Fåk, N. Gauthier, T. Fennell, and M. Kenzelmann, “Candidate quantum spin ice in the pyrochlore $\text{Pr}_2\text{Hf}_2\text{O}_7$ ”, *Physical Review B* **94**, 024436 (2016).
- [23] R. Sibille, E. Lhotel, V. Pomjakushin, C. Baines, T. Fennell, and M. Kenzelmann, “Candidate quantum spin liquid in the Ce^{3+} pyrochlore stannate $\text{Ce}_2\text{Sn}_2\text{O}_7$ ”, *Physical Review Letters* **115**, 097202 (2015).
- [24] J.-J. Wen, S. M. Koochpayeh, K. A. Ross, B. A. Trump, T. M. McQueen, K. Kimura, S. Nakatsuji, Y. Qiu, D. M. Pajerowski, J. R. D. Copley, and C. L. Broholm, “Disordered route to the coulomb quantum spin liquid: random transverse fields on spin ice in $\text{Pr}_2\text{Zr}_2\text{O}_7$ ”, *Physical Review Letters* **118**, 107206 (2017).
- [25] H. D. Zhou, C. R. Wiebe, J. A. Janik, L. Balicas, Y. J. Yo, Y. Qiu, J. R. D. Copley, and J. S. Gardner, “Dynamic spin ice: $\text{Pr}_2\text{Sn}_2\text{O}_7$ ”, *Physical Review Letters* **101**, 227204 (2008).
- [26] P. W. Anderson, “Ordering and antiferromagnetism in ferrites”, *Physical Review* **102**, 1008 (1956).
- [27] A. Banerjee, S. V. Isakov, K. Damle, and Y. B. Kim, “Unusual liquid state of hard-core bosons on the pyrochlore lattice”, *Physical Review Letters* **100**, 047208 (2008).
- [28] O. Benton, L. D. C. Jaubert, R. R. Singh, J. Oitmaa, and N. Shannon, “Quantum spin ice with frustrated transverse exchange: from a π -flux phase to a nematic quantum spin liquid”, *Physical Review Letters* **121**, 067201 (2018).
- [29] O. Benton, L. Jaubert, H. Yan, and N. Shannon, “A spin-liquid with pinch-line singularities on the pyrochlore lattice”, *Nature Communications* **7**, 11572 (2016).
- [30] S. T. Bramwell, M. J. Harris, B. C. den Hertog, M. J. P. Gingras, J. S. Gardner, D. F. McMorrow, A. R. Wildes, A. L. Cornelius, J. D. M. Champion, R. G. Melko, and T. Fennell, “Spin correlations in $\text{Ho}_2\text{Ti}_2\text{O}_7$: a dipolar spin ice system”, *Physical Review Letters* **87**, 047205 (2001).
- [31] B. Canals and C. Lacroix, “Pyrochlore antiferromagnet: a three-dimensional quantum spin liquid”, *Physical Review Letters* **80**, 2933 (1998).
- [32] B. Canals and C. Lacroix, “Quantum spin liquid: the Heisenberg antiferromagnet on the three-dimensional pyrochlore lattice”, *Physical Review B* **61**, 1149 (2000).
- [33] C. Castelnovo, R. Moessner, and S. L. Sondhi, “Magnetic monopoles in spin ice”, *Nature* **451**, 42 (2008).
- [34] S. H. Curnoe, “Quantum spin configurations in $\text{Tb}_2\text{Ti}_2\text{O}_7$ ”, *Physical Review B* **75**, 212404 (2007).

- [35] S. H. Curnoe, “Structural distortion and the spin liquid state in $\text{Tb}_2\text{Ti}_2\text{O}_7$ ”, [Physical Review B](#) **78**, 094418 (2008).
- [36] B. Gao, T. Chen, D. W. Tam, C.-L. Huang, K. Sasmal, D. T. Adroja, F. Ye, H. Cao, G. Sala, M. B. Stone, C. Baines, J. A. T. Verezhak, H. Hu, J.-H. Chung, X. Xu, S.-W. Cheong, M. Nallaiyan, S. Spagna, M. B. Maple, A. H. Nevidomskyy, E. Morosan, G. Chen, and P. Dai, “Experimental signatures of a three-dimensional quantum spin liquid in effective spin-1/2 $\text{Ce}_2\text{Zr}_2\text{O}_7$ pyrochlore”, [Nature Physics](#) **15**, 1052 (2019).
- [37] J. Gaudet, E. M. Smith, J. Dudemaine, J. Beare, C. R. C. Buhariwalla, N. P. Butch, M. B. Stone, A. I. Kolesnikov, G. Xu, D. R. Yahne, K. A. Ross, C. A. Marjerrison, J. D. Garrett, G. M. Luke, A. D. Bianchi, and B. D. Gaulin, “Quantum spin ice dynamics in the dipole-octupole pyrochlore magnet $\text{Ce}_2\text{Zr}_2\text{O}_7$ ”, [Physical Review Letters](#) **122**, 187201 (2019).
- [38] M. Hermele, M. P. A. Fisher, and L. Balents, “Pyrochlore photons: the $U(1)$ spin liquid in a $S = \frac{1}{2}$ three-dimensional frustrated magnet”, [Physical Review B](#) **69**, 064404 (2004).
- [39] Y. Huang, K. Chen, Y. Deng, N. Prokof'ev, and B. Svistunov, “Spin-ice state of the quantum Heisenberg antiferromagnet on the pyrochlore lattice”, [Physical Review Letters](#) **116**, 177203 (2016).
- [40] R. Moessner, S. L. Sondhi, and M. O. Goerbig, “Quantum dimer models and effective Hamiltonians on the pyrochlore lattice”, [Physical Review B](#) **73**, 094430 (2006).
- [41] L. Savary and L. Balents, “Spin liquid regimes at nonzero temperature in quantum spin ice”, [Physical Review B](#) **87**, 205130 (2013).
- [42] N. Shannon, O. Sikora, F. Pollmann, K. Penc, and P. Fulde, “Quantum ice: a quantum Monte Carlo study”, [Physical Review Letters](#) **108**, 067204 (2012).
- [43] M. Taillefumier, O. Benton, H. Yan, L. D. C. Jaubert, and N. Shannon, “Competing spin liquids and hidden spin-nematic order in spin ice with frustrated transverse exchange”, [Physical Review X](#) **7**, 041057 (2017).
- [44] H. Tsunetsugu, “Antiferromagnetic quantum spins on the pyrochlore lattice”, [Journal of the Physical Society of Japan](#) **70**, 640 (2001).
- [45] H. Tsunetsugu, “Spin-singlet order in a pyrochlore antiferromagnet”, [Physical Review B](#) **65**, 024415 (2001).
- [46] H. Yan, O. Benton, L. Jaubert, and N. Shannon, “Theory of multiple-phase competition in pyrochlore magnets with anisotropic exchange with application to $\text{Yb}_2\text{Ti}_2\text{O}_7$, $\text{Er}_2\text{Ti}_2\text{O}_7$, and $\text{Er}_2\text{Sn}_2\text{O}_7$ ”, [Physical Review B](#) **95**, 094422 (2017).

-
- [47] Y. Iqbal, T. Müller, P. Ghosh, M. J. Gingras, H. O. Jeschke, S. Rachel, J. Reuther, and R. Thomale, “Quantum and classical phases of the pyrochlore Heisenberg model with competing interactions”, [Physical Review X](#) **9**, 011005 (2019).
- [48] J. Reuther, “Frustrated quantum Heisenberg antiferromagnets: functional renormalization-group approach in auxiliary-fermion representation”, PhD thesis (Karlsruhe Institute of Technology, 2011).
- [49] J. Reuther and P. Wölfle, “ J_1 - J_2 frustrated two-dimensional Heisenberg model: random phase approximation and functional renormalization group”, [Physical Review B](#) **81**, 144410 (2010).
- [50] Y. Iqbal, R. Thomale, F. Parisen Toldin, S. Rachel, and J. Reuther, “Functional renormalization group for three-dimensional quantum magnetism”, [Physical Review B](#) **94**, 140408 (2016).
- [51] J. Thoenniss, M. K. Ritter, F. B. Kugler, J. von Delft, and M. Punk, “Multiloop pseudofermion functional renormalization for quantum spin systems: application to the spin- $\frac{1}{2}$ kagome Heisenberg model”, [arXiv:2011.01268](#).
- [52] F. B. Kugler and J. von Delft, “Derivation of exact flow equations from the self-consistent parquet relations”, [New Journal of Physics](#) **20**, 123029 (2018); Corrected in “Erratum: derivation of exact flow equations from the self-consistent parquet relations (2018 New J. Phys. 20 123029)”, [New Journal of Physics](#) **21**, 099601 (2019).
- [53] F. B. Kugler, “Renormalization group approaches to strongly correlated electron systems”, PhD thesis (Ludwig-Maximilians-Universität München, 2019).
- [54] F. B. Kugler and J. von Delft, “Multiloop functional renormalization group for general models”, [Physical Review B](#) **97**, 035162 (2018).
- [55] F. B. Kugler and J. von Delft, “Multiloop functional renormalization group that sums up all parquet diagrams”, [Physical Review Letters](#) **120**, 57403 (2018).
- [56] C. Hille, F. B. Kugler, C. J. Eckhardt, Y.-Y. He, A. Kauch, C. Honerkamp, A. Toschi, and S. Andergassen, “Quantitative functional renormalization group description of the two-dimensional Hubbard model”, [Physical Review Research](#) **2**, 033372 (2020).
- [57] D. Kiese, T. Mueller, Y. Iqbal, R. Thomale, and S. Trebst, “Multiloop functional renormalization group approach to quantum spin systems”, [arXiv:2011.01269](#).
- [58] S. Onoda and Y. Tanaka, “Quantum fluctuations in the effective pseudospin- $\frac{1}{2}$ model for magnetic pyrochlore oxides”, [Physical Review B](#) **83**, 094411 (2011).

- [59] S. Onoda and Y. Tanaka, “Quantum melting of spin ice: emergent cooperative quadrupole and chirality”, *Physical Review Letters* **105**, 047201 (2010).
- [60] S. Lee, S. Onoda, and L. Balents, “Generic quantum spin ice”, *Physical Review B* **86**, 104412 (2012).
- [61] G. Chen, “Spectral periodicity of the spinon continuum in quantum spin ice”, *Physical Review B* **96**, 085136 (2017).
- [62] N. Shannon, T. Momoi, and P. Sindzingre, “Nematic order in square lattice frustrated ferromagnets”, *Physical Review Letters* **96**, 027213 (2006).
- [63] N. Shannon, K. Penc, and Y. Motome, “Nematic, vector-multipole, and plateau-liquid states in the classical $O(3)$ pyrochlore antiferromagnet with biquadratic interactions in applied magnetic field”, *Physical Review B* **81**, 184409 (2010).
- [64] A. Smerald, H. T. Ueda, and N. Shannon, “Theory of inelastic neutron scattering in a field-induced spin-nematic state”, *Physical Review B* **91**, 174402 (2015).
- [65] M. E. Zhitomirsky and H. Tsunetsugu, “Magnon pairing in quantum spin nematic”, *Europhysics Letters* **92**, 37001 (2010).
- [66] A. Altland and B. Simons, *Condensed matter field theory* (Cambridge University Press, Cambridge, 2010), p. 770.
- [67] T. H. Han, J. S. Helton, S. Chu, D. G. Nocera, J. A. Rodriguez-Rivera, C. Broholm, and Y. S. Lee, “Fractionalized excitations in the spin-liquid state of a kagome-lattice antiferromagnet”, *Nature* **492**, 406 (2012).
- [68] M. J. Harris, S. T. Bramwell, D. F. McMorrow, T. Zeiske, and K. W. Godfrey, “Geometrical frustration in the ferromagnetic pyrochlore $\text{Ho}_2\text{Ti}_2\text{O}_7$ ”, *Physical Review Letters* **79**, 2554 (1997).
- [69] M. J. Harris, S. T. Bramwell, T. Zeiske, D. F. McMorrow, and P. J. King, “Magnetic structures of highly frustrated pyrochlores”, *Journal of Magnetism and Magnetic Materials* **177-181**, 757 (1998).
- [70] C. Liu, G. B. Halász, and L. Balents, “Competing orders in pyrochlore magnets from a \mathbb{Z}_2 spin liquid perspective”, *Physical Review B* **100**, 075125 (2019).
- [71] A. A. Abrikosov, “Electron scattering on magnetic impurities in metals and anomalous resistivity effects”, *Physics Physique Fizika* **2**, 5 (1965).
- [72] V. N. Popov and S. A. Fedotov, “The functional integration method and diagram technique for spin systems”, *Soviet Physics JETP* **67**, 535 (1988).

-
- [73] J. Brinckmann and P. Wölfle, “Auxiliary-fermion approach to critical fluctuations in the two-dimensional quantum antiferromagnetic Heisenberg model”, *Physical Review B* **70**, 174445 (2004).
- [74] M. L. Baez and J. Reuther, “Numerical treatment of spin systems with unrestricted spin length S : A functional renormalization group study”, *Physical Review B* **96**, 045144 (2017).
- [75] J. Thoenniss, “Multiloop Functional Renormalization Group Studies of Heisenberg Models on the Kagome Lattice”, Master’s thesis (Ludwig-Maximilians-Universität München, 2019).
- [76] B. Roulet, J. Gavoret, and P. Nozières, “Singularities in the X-ray absorption and emission of metals. I. First-order parquet calculation”, *Physical Review* **178**, 1072 (1969).
- [77] F. J. Dyson, “The S matrix in quantum electrodynamics”, *Physical Review* **75**, 1736 (1949).
- [78] I. Diatlov, V. Sudakov, and K. Ter-Martirosian, “Asymptotic meson-meson scattering theory”, *Soviet Physics JETP* **5**, 631 (1957).
- [79] E. E. Salpeter and H. A. Bethe, “A relativistic equation for bound-state problems”, *Physical Review* **84**, 1232 (1951).
- [80] J. Schwinger, “On the green’s functions of quantized fields. I”, *Proceedings of the National Academy of Sciences* **37**, 452 (1951).
- [81] J. Schwinger, “On the green’s functions of quantized fields. II”, *Proceedings of the National Academy of Sciences* **37**, 455 (1951).
- [82] Y. A. Bychkov, L. P. Gor’kov, and I. E. Dzyaloshinskii, “Possibility of superconductivity type phenomena in a one-dimensional system”, *Soviet Physics JETP* **23**, 489 (1966).
- [83] W. Metzner, M. Salmhofer, C. Honerkamp, V. Meden, and K. Schönhammer, “Functional renormalization group approach to correlated fermion systems”, *Reviews of Modern Physics* **84**, 299 (2012).
- [84] K. G. Wilson, “The renormalization group: critical phenomena and the Kondo problem”, *Reviews of Modern Physics* **47**, 773 (1975).
- [85] P. Kopietz, L. Bartosch, and F. Schütz, *Introduction to the functional renormalization group*, Lecture Notes in Physics (Springer, Heidelberg, 2010).
- [86] F. L. Buessen, V. Noculak, S. Trebst, and J. Reuther, “Competing magnetic orders and spin liquids in two- and three-dimensional kagome systems: pseudofermion functional renormalization group perspective”, *Physical Review B* **100**, 125164 (2019).
- [87] C. Taranto, S. Andergassen, J. Bauer, K. Held, A. Katanin, W. Metzner, G. Rohringer, and A. Toschi, “From infinite to two dimensions through the functional renormalization group”, *Physical Review Letters* **112**, 196402 (2014).

- [88] J. R. Cash and A. H. Karp, “A variable order runge-kutta method for initial value problems with rapidly varying right-hand sides”, [ACM Transactions on Mathematical Software](#) **16**, 201 (1990).
- [89] W. H. Press, S. A. Teukolsky, W. T. Vetterling, and B. P. Flannery, *Numerical recipes*, 3rd ed. (Cambridge University Press, Cambridge, 2007).
- [90] C. Runge, “Ueber die numerische Auflösung von Differentialgleichungen”, [Mathematische Annalen](#) **46**, 167 (1895).
- [91] D. G. Anderson, “Iterative procedures for nonlinear integral equations”, [Journal of the ACM](#) **12**, 547 (1965).
- [92] C. G. Broyden, “A class of methods for solving nonlinear simultaneous equations”, [Mathematics of Computation](#) **19**, 577 (1965).
- [93] H.-R. Fang and Y. Saad, “Two classes of multiseccant methods for nonlinear acceleration”, [Numerical Linear Algebra with Applications](#) **16**, 197 (2009).
- [94] N. Wentzell, G. Li, A. Tagliavini, C. Taranto, G. Rohringer, K. Held, A. Toschi, and S. Andergassen, “High-frequency asymptotics of the vertex function: diagrammatic parametrization and algorithmic implementation”, [Physical Review B](#) **102**, 085106 (2020).
- [95] I. Affleck, Z. Zou, T. Hsu, and P. W. Anderson, “SU(2) gauge symmetry of the large- U limit of the Hubbard model”, [Physical Review B](#) **38**, 745 (1988).
- [96] M. Hering and J. Reuther, “Functional renormalization group analysis of dzyaloshinsky-moriya and Heisenberg spin interactions on the kagome lattice”, [Physical Review B](#) **95**, 054418 (2017).
- [97] M. Rück and J. Reuther, “Effects of two-loop contributions in the pseudofermion functional renormalization group method for quantum spin systems”, [Physical Review B](#) **97**, 144404 (2018).
- [98] R. Suttner, C. Platt, J. Reuther, and R. Thomale, “Renormalization group analysis of competing quantum phases in the J_1 - J_2 Heisenberg model on the kagome lattice”, [Physical Review B](#) **89**, 020408 (2014).
- [99] C. L. Henley, “Power-law spin correlations in pyrochlore antiferromagnets”, [Physical Review B](#) **71**, 014424 (2005).
- [100] E. Berg, E. Altman, and A. Auerbach, “Singlet excitations in pyrochlore: a study of quantum frustration”, [Physical Review Letters](#) **90**, 147204 (2003).
- [101] F. J. Burnell, S. Chakravarty, and S. L. Sondhi, “Monopole flux state on the pyrochlore lattice”, [Physical Review B](#) **79**, 144432 (2009).
- [102] B. Canals and D. Garanin, “Spin-liquid phase in the pyrochlore antiferromagnet”, [Canadian Journal of Physics](#) **79**, 1323 (2001).

-
- [103] V. R. Chandra and J. Sahoo, “Spin- $\frac{1}{2}$ Heisenberg antiferromagnet on the pyrochlore lattice: an exact diagonalization study”, [Physical Review B](#) **97**, 144407 (2018).
- [104] R. Moessner and J. T. Chalker, “Properties of a classical spin liquid: the Heisenberg pyrochlore antiferromagnet”, [Physical Review Letters](#) **80**, 2929 (1998).
- [105] P. Müller, A. Lohmann, J. Richter, and O. Derzhko, “Thermodynamics of the pyrochlore-lattice quantum Heisenberg antiferromagnet”, [Physical Review B](#) **100**, 024424 (2019).
- [106] R. Schäfer, I. Hagymási, R. Moessner, and D. J. Luitz, “Pyrochlore $S = \frac{1}{2}$ Heisenberg antiferromagnet at finite temperature”, [Physical Review B](#) **102**, 054408 (2020).
- [107] O. Benton, O. Sikora, and N. Shannon, “Seeing the light: experimental signatures of emergent electromagnetism in a quantum spin ice”, [Physical Review B](#) **86**, 075154 (2012).
- [108] O. Derzhko, T. Hutak, T. Krokhnalskii, J. Schnack, and J. Richter, “Adapting Planck’s route to investigate the thermodynamics of the spin-half pyrochlore Heisenberg antiferromagnet”, [Physical Review B](#) **101**, 174426 (2020).
- [109] Y. Kato and S. Onoda, “Numerical evidence of quantum melting of spin ice: quantum-to-classical crossover”, [Physical Review Letters](#) **115**, 077202 (2015).
- [110] A. V. Oppenheim and R. W. Schaffer, *Discrete-time signal processing*, 2nd ed. (Prentice Hall, Upper Saddle River, 1998).
- [111] M. Frigo and S. G. Johnson, “The design and implementation of FFTW3”, [Proceedings of the IEEE](#) **93**, 216 (2005).
- [112] J. W. Cooley and J. W. Tukey, “An algorithm for the machine calculation of complex fourier series”, [Mathematics of Computation](#) **19**, 297 (1965).

Selbständigkeitserklärung

Hiermit erkläre ich, die vorliegende Arbeit selbständig verfasst und keine anderen als die angegebenen Quellen und Hilfsmittel benutzt zu haben.

München, 15. März 2021

Marc Ritter
